Bridging Spatiotemporal Scales in Multicellular Organization and Information Processing

Thesis submitted in partial fulfillment
of the requirements for the degree of
"DOCTOR OF PHILOSOPHY"

by

Amos Zamir

Submitted to the Senate of Ben-Gurion University
of the Negev
22st Oct, 2024
Beer-Sheva

Bridging Spatiotemporal Scales in Multicellular Organization and Information Processing

Thesis submitted in partial fulfillment of the requirements for the degree of
“DOCTOR OF PHILOSOPHY”

by

Amos Zamir

Submitted to the Senate of Ben-Gurion University of the Negev

Approved by the advisor

Approved by the Dean of the Kreitman School of Advanced Graduate Studies

22st Oct, 2024

Beer-Sheva

This work was carried out under the supervision of Prof. Assaf Zaritsky in the Department of Software and Information Systems Engineering, Faculty of Engineering Science, Ben-Gurion University, Beer-Sheva, Israel

Amos Zamir
Bridging Spatiotemporal Scales in Multicellular Organization and Information Processing
22st Oct, 2024
Supervisor: Prof. Assaf Zaritsky

Ben-Gurion University of the Negev
Faculty of Engineering Sciences
Department of Software and Information Systems Engineering
Marcus Family Campus, Ben-Gurion University of the Negev, Israel
PO Box 653 Be'er Sheva 8410501

Research-Student's Affidavit when Submitting the Doctoral Thesis for Judgment

I Amos Zamir, whose signature appears below, hereby declare that:

1. I have written this Thesis by myself, except for the help and guidance offered by my Thesis Advisors.
2. The scientific materials included in this Thesis are products of my own research, culled from the period during which I was a research student.
3. This Thesis incorporates research materials produced in cooperation with others, excluding the technical help, excluding result analysis, commonly applied during such experimental work. Therefore, I attach an additional affidavit stating the contributions made by myself and the other participants in this research, which has been approved by them and submitted with their approval.

The work presented in this Thesis was done in cooperation with two biological laboratories. The laboratories mainly contributed data and the biological motivation and background. All the computational models and performed computational simulations done by me under the supervision of Prof. Assaf Zartisky. The collaborators are:

1. Bo Sun and his lab at Oregon State University.
2. Leeat Keren and her lab at Weizmann Institute.

Date: 22st Oct 2024 Student's name: Amos Zamir Signature: ____________________

ACKNOWLEDGEMENTS

First, I would like to thank my mentor, Prof. Assaf Zartisky, for his unwavering support, guidance, mentorship, and commitment to my development and success.

I want to express my deepest gratitude and appreciation to my beloved wife, whose unwavering support and love have given me the peace and strength needed to complete this challenging work. In addition, thanks to my daughters for sacrificing many parental hours for my personal development and supporting me with love and patience thourgh my academic journey.

Table of Contents

Abstract

Self-organization is a process in which individual cells arrange in a higher-level order of structures and patterns. This dissertation bridges spatial scales in multicellular signaling dynamics and multicellular organization. The first chapter investigates endothelial cell monolayers' calcium synchronization in response to mechanical stimuli. We used information theory to quantify the asymmetric information-transfer between pairs of cells and defined quantitative measures of how single cells receive or transmit information in the multicellular network. We revealed that collective synchronization emerged through gradual information spread, driven by heterogeneous communication properties among cells. The second chapter introduces Context-dependent Identification of Spatial Motifs (CISM), a method for identifying modular cellular interactions at a fine spatial scale of a few cells. Applied to melanoma and triple-negative breast cancer (TNBC) spatial single cell proteomics data, CISM predicts disease states effectively and uncovers specific cellular compositions and spatial cellular organization that characterize different disease conditions. These studies reveal the modular components and emerging dynamics that lead to collective cell behavior for understanding multicellular self-organization and associating modular components with disease states.

Keywords

cell-cell communication, live cell imaging, calcium dynamics, multicellular synchronization, mechanosensing, Granger causality, spatial single cell proteomics, tumor microenvironment, network motifs, triple negative breast cancer, melanoma

Introduction

Cell biological processes cross scales in space and time: molecules organize within cells, and cells organize within tissues. The architecture and functional state of a healthy tissue relies on individual cells using basic cellular machineries to influence and respond to neighboring cells through a complex interplay of chemical and physical cues. Dysfunctional regulation of molecular and cellular processes underlies the defected tissue organization and function in disease. How local interactions at the single cell scale are integrated in space and time to induce function or loss of function at the tissue scale is yet to be fully resolved. This dissertation investigates the fundamental question of how do cellular heterogeneity and noisy interactions between cells converge to regulate the emergence of tissue scale architecture and function?

Progress in this area has been confounded by the technical challenges in systematically characterizing heterogeneity and bridging scales in space and time. Traditional approaches of perturbing the cells and measuring alterations in the collective tissue response cannot explain the bottom-up process of coordinating groups of cells at the tissue scale because population averages mask the single cell heterogeneity and the spatiotemporal integration of information across scales, i.e., from the scale of organelles within cells to single cells to the multicellular collective that enables a biological function. Thus, elucidating emergent physiological tissue state requires systematic and integrated quantitative evaluation of the system's "atomic" components, in single cells and their composition, as well as of how single cells interact with one another to contribute to the collective tissue outcome. This dissertation investigates two bottom-up modular characterizations of tissue state: following the bottom-up collective signaling synchronization process of an endothelial monolayer in response to shear stress and identifying multicellular modular components as an intermediate scale of multicellular organization in melanoma and triple-negative breast cancer patients (Fig. I1).

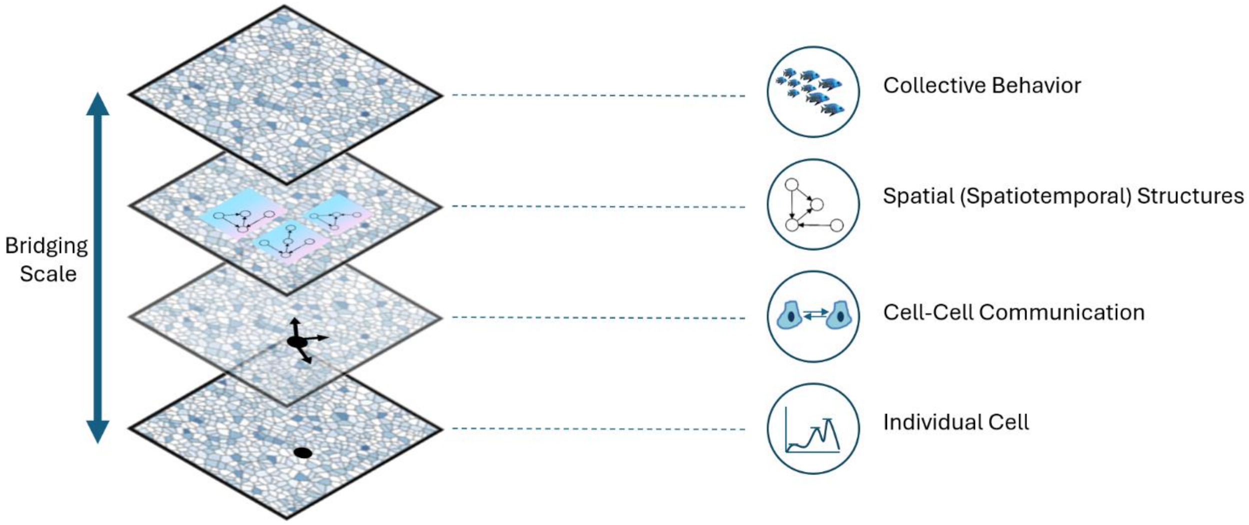

Figure I1. Bridging the scale between single and collective cell behavior and organization. Illustration of different modular perspectives between individual cell analysis and self-organized multicellular system. Bottom-up: single cell, pairwise analysis, spatial modular components, and self-organized multicellular system.

In the first chapter of my dissertation, we quantitatively characterized the dynamics of multicellular synchronization at the single-cell level using a data-driven approach and tools from information theory. We quantitatively characterized the process of mechanically stimulated multicellular calcium synchronization by applying Granger-causality and network analysis to live calcium imaging of endothelial cell monolayers. At the cellular scale, we found that increased connectivity, heterogeneity, and memory were associated with the emergence of synchronization across a multicellular network by a gradual transition from local to global information spread. We propose that cells gradually learn their local environment, adjust, and reinforce their internal state to stabilize the multicellular network architecture to support information flow from local to global scales toward multicellular synchronization. A full version was published in the Cell System journal in 2022.

The second chapter introduces a new method termed Context-dependent Identification of Spatial Motifs (CISM) that captures recurrent patterns in cell type organization within the tissue to identify modular components at the spatial scale of a few cells. Spatial motifs are defined as sub-networks that occur more than expected in the cellular network that is composed of cells (nodes), cell types (node color), and the cells' spatial adjacency (edges). CISM extracts all motifs from each tissue and then filters them according to a specific query, such as what motifs are discriminative between different tissue clinical disease states. The method enables biological insight at the spatial scale of a few cells and their composition. We applied the method to infer differences in the microenvironment of different disease states in the context of Melanoma and TNBC using singe cell proteomics imaging. CISM can be used for hypothesis generation and explanatory modeling. This study will very soon be released to *biorxiv* and submitted for publication.

Cumulatively, my research demonstrates bottom-up approaches for bridging the scales between single-cell and multicellular information processing and decision-making, an innovation necessary for a more holistic and complete understanding of how multicellular systems operate.

Chapter 1: Emergence of synchronized multicellular mechanosensing from spatiotemporal integration of heterogeneous single-cell information transfer

Amos Zamir[1], Guanyu Li[2,3], Katelyn Chase[3], Robert Moskovitch[1], Bo Sun[2*], Assaf Zaritsky[1,4*]

[1]Department of Software and Information Systems Engineering, Ben-Gurion University of the Negev, Beer-Sheva 84105, Israel

[2]Department of Physics, Oregon State University, Corvallis, OR 97331, USA

[3]Lewis-Sigler Institute for Integrative Genomics, Princeton University, Princeton, NJ 08544, USA

*Corresponding author

Assaf Zaritsky, assafza@bgu.ac.il

Bo Sun, sunb@physics.oregonstate.edu

Publication details: Zamir, Amos, et al. "Emergence of synchronized multicellular mechanosensing from spatiotemporal integration of heterogeneous single-cell information transfer." *Cell systems* 13.9 (2022): 711-723. DOI: 10.1016/j.cels.2022.07.002

---

[4] Lead contact

Summary

Multicellular synchronization is a ubiquitous phenomenon in living systems. However, how noisy and heterogeneous behaviors of individual cells are integrated across a population toward multicellular synchronization is unclear. Here we study the process of multicellular calcium synchronization of endothelial cell monolayer in response to mechanical stimuli. We applied information-theory to quantify the asymmetric information-transfer between pairs of cells and defined quantitative measures to how single cells receive or transmit information within a multicellular network. Our analysis revealed that multicellular synchronization was established by gradual enhancement of information spread from the single cell to the multicellular scale. Synchronization was associated with heterogeneity in the cells' communication properties, reinforcement of the cells' state and information flow. Altogether, we suggest a phenomenological model where cells gradually learn their local environment, adjust and reinforce their internal state to stabilize the multicellular network architecture to support information flow from local to global scales toward multicellular synchronization. A record of this paper's Transparent Peer Review process is included in the Supplemental Information.

Introduction

Synchronized multicellular dynamics is the basis of many critical physiological processes, such as the rhythmic beating of cardiomyocytes, planar cell polarity, and brain activities. The human endothelium, for instance, consists of a staggering over one trillion endothelial cells which constantly monitor environmental cues such as shear stress, in order to collectively regulate the vasculature tone (Davies, 2008; Wolinsky, 1980). However, a fundamental question remains elusive: how synchronization in the group emerges from the interactions of individual cells, each making stochastic decisions based on noisy cues from their local environment?

A major challenge toward establishing multicellular synchronization lays at how single cells translate environment information to intracellular signaling responses (Perkins Peter S., 2009). Signaling in cells often rely on low copy numbers of proteins (Huang et al., 2007) and diffusion limited intracellular transport (Brangwynne et al., 2009). These effects, often considered as intrinsic noises, lead to variable single cell signaling dynamics even in response to identical external stimuli (Elowitz et al., 2002; Swain et al., 2002). Cell-to-cell variation, or intercellular heterogeneity, is present even for cells originating from the same genetic background, also complicates our understanding of multicellular synchronization processes. Such cell-to-cell variation, or non-genetic intercellular heterogeneity, may arise from differences in gene expression levels (also terms as extrinsic noise), alternative splicing, as well as post translation modifications (Bintu et al., 2016; Elowitz et al., 2002; Gut et al., 2018; Ng et al., 2018; Raj and van Oudenaarden, 2008). Intercellular heterogeneity implies that individual cells take different states, or phenotypes, which may be related with intrinsic noises such as by varying the copy number of receptors to modulate the probability of activation (Young et al., 2008). Intercellular heterogeneity also modulates the propensity of cells to interact with their peers, as the communication between cells depend on specialized molecular channels such as gap junctions (Calderón and Retamal, 2016; Nicholson and Bruzzone, 1997). However, it is not known whether non-genetic intercellular heterogeneity can play a constructive role in information transfer between cells in multicellular systems. As such, we ask whether some cells within a group function as leaders or followers, promoting the spread of information through the group, while others act individually, and whether such heterogeneity is important for the synchronization of multicellular dynamics.

Previously, we demonstrated that cell-cell communication through gap junctions (Fujii et al., 2017) modulated ATP-induced calcium signaling in monolayers of fibroblast cells (Sun et al., 2012). Tuning the levels of intercellular communications, by varying cell densities, inserting weakly-communicating cells, and by pharmacologically inhibiting gap junctions, controlled the temporal coordination of calcium signaling in neighboring cells (Potter et al., 2016; Sun et al., 2012). Others have also highlighted the role of local gap-junction mediated cell-cell communication in functional multicellular connectivity of neural progenitor cells at the vascular interface (Lacar et al., 2011), in neural stem cell reactivation in the blood-brain barrier (Spéder and Brand, 2014), in neural progenitors cell proliferation during embryonic development (Malmersjö et al., 2013) and in coordinated fate decisions (Ho et al., 2021).

To elucidate how information transfer between single cells is integrated to synchronize population-level cellular responses, we study the physiological process where monolayers of endothelial cells collectively sense and respond to external shear stress. Endothelial cells line the interior surface of blood vessels and form a monolayer that experiences varying levels of shear stress from blood flow (Hill et al., 2010; Yin et al., 2007). Upon changing the flow rate (e.g., during acute wound), endothelial cells detect the change in shear stress, inform other cells such as smooth muscle cells, and adjust their internal signaling accordingly. Central to the cascade of events, shear stress leads to downstream ATP activation which modulates calcium signaling at the subcellular scale (Faehling et al., 2002; Kohn et al., 1995; Rubanyi and Vanhoutte, 1988). As a group, the endothelial cells must coordinate their signaling dynamics to achieve a coherent and collective response. Specifically, intercellular calcium levels are synchronized via gap junction-mediated cell-cell communication (Kumar and Gilula, 1996; Sun et al., 2012). Such synchronized calcium signaling is instrumental in modulating reepithelialization, angiogenesis, and extracellular matrix remodeling, which are essential processes in wound repair (Aihara et al., 2013; Eming et al., 2014; Handly and Wollman, 2017; Lee et al., 2019; Shannon et al., 2017).

In this study we developed an integrated experimental-computational approach to quantitatively evaluate the roles that single cells take during the emergence of multicellular synchronization. Using this platform, we identified three key functions whereby single cells contribute to collective information processing that ultimately leads to multicellular synchronization. *Division of labor*, where single cells take differentiated functional roles in collective information processing; *Cell memory*, where single cells maintain and reinforce their specified functional roles in cell-cell communication in response to repeated external stimuli; And *information flow*, where the information gradually propagates spatially from the scale of single cells to eventually synchronize the collective.

Results

Endothelial cells in a monolayer adapt their calcium dynamics in response to external shear stress

We employed a microfluidics system that can precisely control the temporal profile of the shear stress that the cells experience (Fig. 1.1A top). We grew confluent monolayers of HUVEC (Human Umbilical Vascular Endothelial Cell) cells on the bottom surface of the flow channels (Fig. 1.1A bottom). A computer interfaced flow switch regulated input pressure to induce smooth flow profiles in the microfluidic channel as verified by particle image velocimetry (Fig. 1.1B). The shear stress -induced calcium signal of the HUVEC cells was imaged with the fluorescent calcium indicator Calbryte-520 at single cell resolution (Fig. 1.1A inset, Video S1). We manually marked each cell center (Fig. 1.1A inset), recorded the intracellular calcium signal as a time-series of fluorescent intensity for every cell and verified that the magnitude of the cell's calcium signal correlated with the magnitude of the applied flow shear stress (Fig. 1.1C, Methods). This setting enabled us to investigate the collective mechanosensing of HUVEC cells to fluid shear stresses, a scenario that mimics the physiological function of the endothelium.

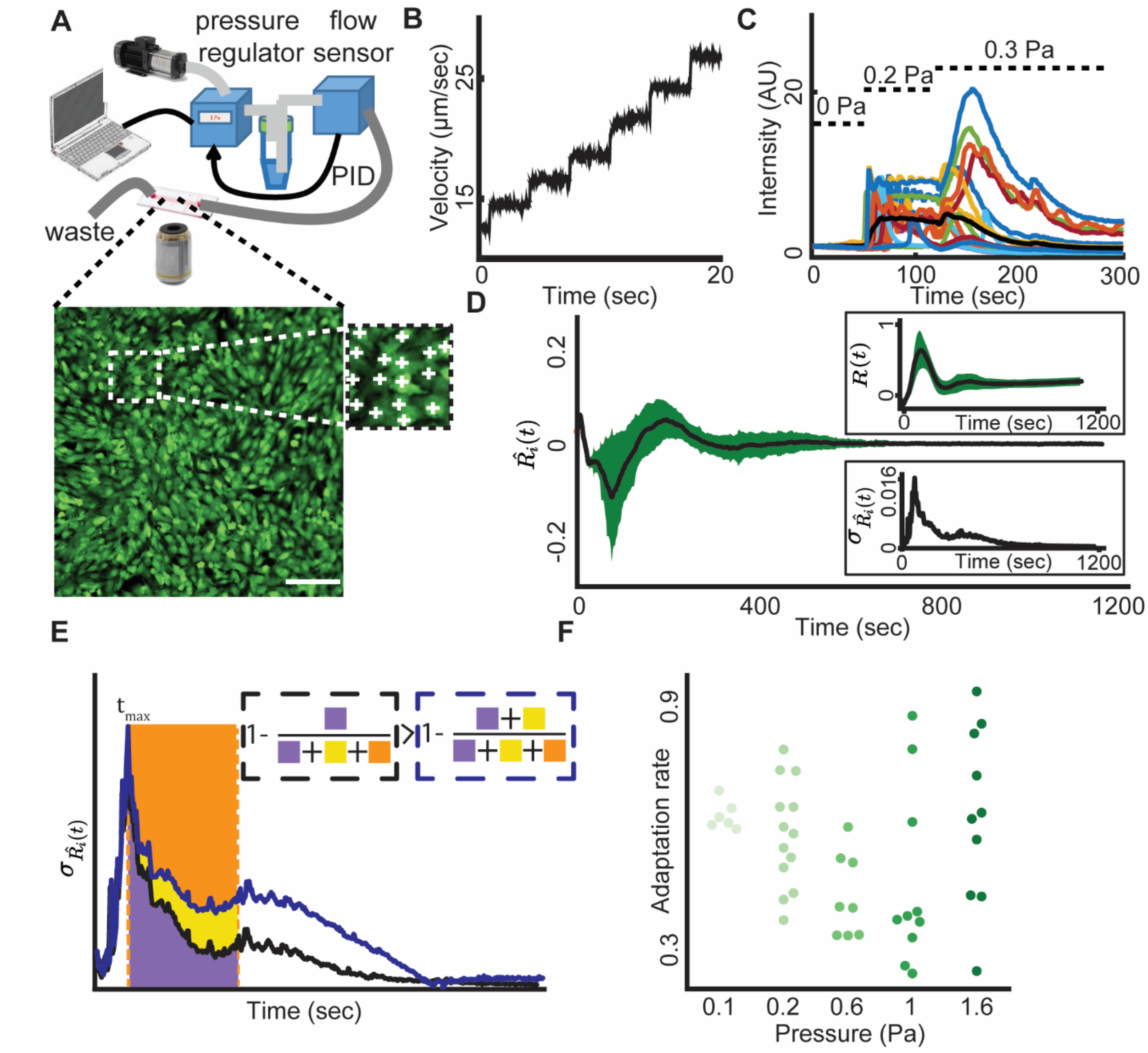

Figure 1.1. Collective calcium signaling of mechanosensing as a model to investigate the emergence of multicellular synchronization at the single cell resolution. (**A**) In a typical experiment, a monolayer of HUVEC was cultured in a microfluidic device where fluid flow applied shear stress on the cells. Top: Schematics of the setup. The input pressure that drives a laminar flow in the single channel microfluidics is controlled by a computer interface. The pressure is regulated in real time via a PID loop consisting of a pressure regulator and a flow sensor. Bottom: A monolayer of HUVEC loaded with the fluorescent calcium indicator Calbryte-520 as a readout of the cellular response to flow shear stress. Scale bar = 50 μm. Inset: manual annotation of single cells. (**B**) Particle image velocimetry verified that the regulated input pressure produces a smooth flow profile in the microfluidics channel. (**C**) Cells respond to step increase in the flow shear stress. Relative intensity is the relative change of the fluorescence intensity from the basal cell level (Methods). Colored lines: individual cell calcium responses. Black line: mean response of over 400 cells in the field of view. Dashed horizontal lines indicate the time interval of 0, 0.2, 0.3 Pa shear stress correspondingly. (**D**) Multicellular calcium dynamics is synchronized over time in response to external mechanical stimuli. The flow shear stress is applied from the onset of imaging (t = 0). The calcium dynamics of each cell was represented by the time-derivative of its relative fluorescent intensity. Black: mean calcium *Ri*(*t*) dynamics; Green: standard deviation. Top inset: mean (black) and

standard deviation (green) of single cell calcium relative intensity (Methods) over time. Bottom Inset: standard deviation of calcium dynamics over time. (**E**) Depiction of the adaption rate measure overlayed on the plot of the standard deviation of calcium dynamics overtime. There are two solid lines; the black represents faster adaptation compared to blue. Adaption rate of the black / blue solid line is one minus the ratio between the area under the curve for 400 seconds (200 frames, purple / yellow + purple area) and the area of the rectangle whose height is set by the maximum variations of individual cell dynamics (yellow + orange + purple area). See Methods for full description. (**F**) Multicellular adaption rate for increasing shear stress levels. Each observation represents a biological replica. N =47 biological replicates: n = 6 (0.1 Pa), n = 13 (0.2 Pa), n = 8 (0.6 Pa), n = 10 (1 Pa), n = 10 (1.6 Pa).

Upon exposing the cells to a step-like increase in shear stress to 0.2 Pa, which is similar to those that an endothelial cell experiences during acute bleeding (Albuquerque et al., 2000), the variability in the cells' temporal derivative of their calcium signal (termed *calcium dynamics*, annotated $\widehat{R_i}(t)$ (Methods)) increased and then gradually reduced until the cells adapted to the external stress and converged to a steady state (Fig. 1.1D). We defined the *adaptation rate* as $1 - \left(\frac{\int_{t_{max}}^{t_{max}+400} \sigma_{\widehat{R_i}(t)}(t)}{400 * \sigma_{\widehat{R_i}(t_{max})}}\right)$, where $\sigma_{\widehat{R_i}(t)}(t)$ is the population-level standard deviation of single cell calcium dynamics $\widehat{R_i}(t)$ at time *t*, and $t_{max} = \underset{t}{argmax}\, \sigma_{\widehat{R_i}(t)}(t)$ is the time of the peak variability in calcium dynamics (Methods, Fig. 1.1E). The adaptation rate is a non-parametric measurement for the speed that the multicellular system adapts to the external stress. When a system rapidly synchronizes, adaptation rate approaches one. Conversely, if a system maintains a large deviation between the dynamics of individual cells, adaptation rate is close to zero. In general, higher adaptation rate implies faster multicellular adaptation to the external stress (Fig. 1.1E black curve adapts faster than blue curve). The endothelial monolayer adapted to increasing levels of shear stress ranging from 0.1 to 1.6 Pa (Fig. 1.1F, Fig. S1.1 - parametric exponential model) demonstrating the robustness of the multicellular system in adaptation to varying physiological-relevant levels of external mechanical stimuli (Charbonier et al., 2019). Altogether, these results suggested that the cells gradually adapted despite the vast variability in single cell calcium response at the onset of shear stress.

The interplay between information flow, heterogeneity and multicellular adaptation

We hypothesized that integrating and propagating information from the local scale, between single cells, to the global scale, drove the adaptation of an inherently heterogeneous multicellular system to external mechanical stimuli. To investigate this hypothesis, we defined quantitative measures for cell-cell communication. If two cells communicate, we expect the past calcium dynamics of one cell to contain information regarding the future calcium dynamics of the other cell. Defined in this way, cell-cell communications can be bidirectional and asymmetric – cell A can influence its neighbor B differently from how cell B influences A (Fig. 1.2A). To quantify asymmetric cell-cell communication, we used Granger Causality (Granger, 1969) (GC), a classic statistical method from the field of information theory, to infer cause-effect relationships between cell pairs from their fluctuating calcium dynamics. Granger Causality uses linear regression to quantify the extent to which the prediction of values in one time series can be improved by including information from another time series. This provides us with an established framework to extract feedback and feedforward relations from pairwise variables' fluctuating time-series.

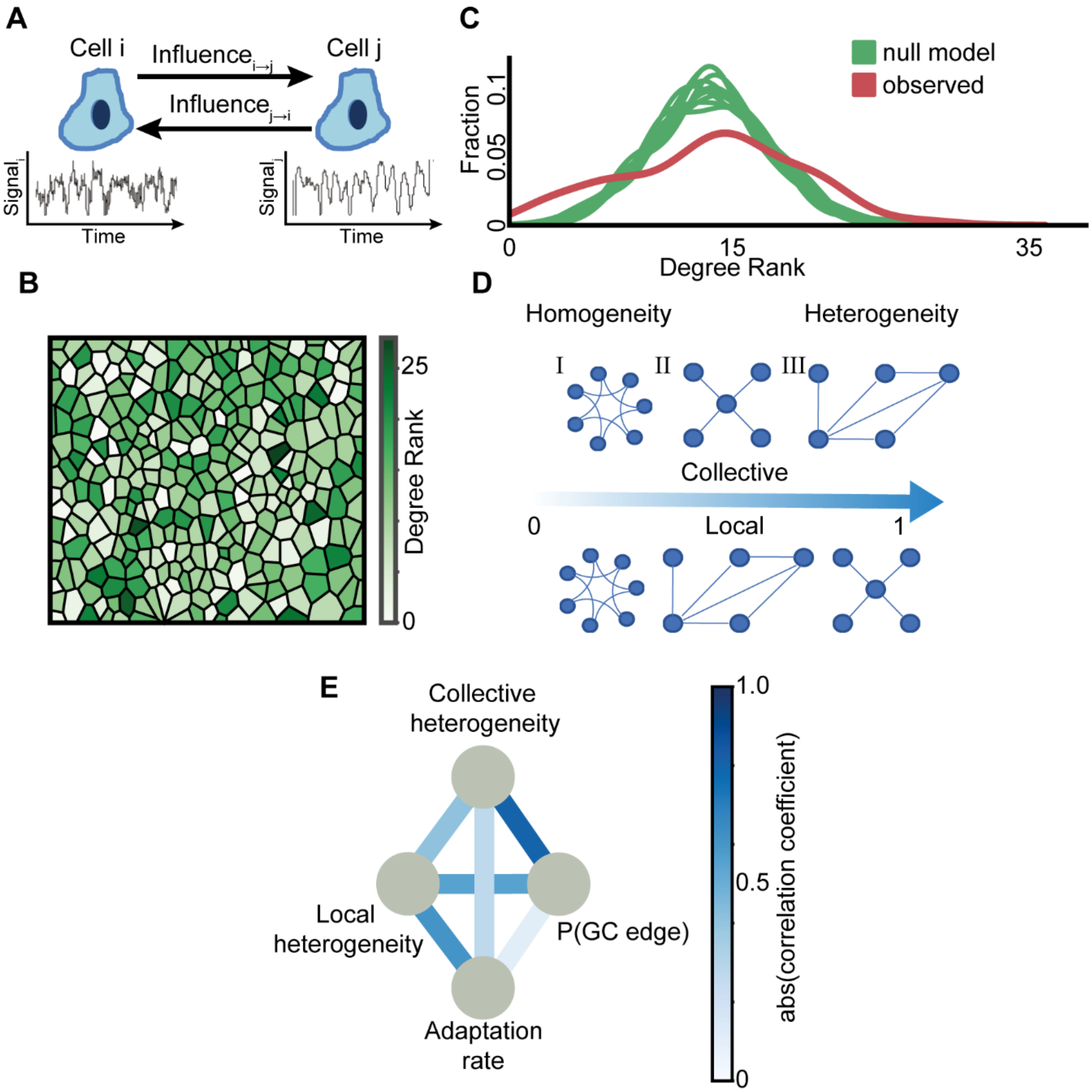

Figure 1.2. Correlating information flow, collective and local heterogeneity in single cell information transfer and multicellular adaptation. (**A**) Schematics of cell-cell communication. Generic estimation of the asymmetric mutual influence between a pair of cells from their fluctuating time series. The influence of cell i on cell j is defined as the extent to which the past signal of cell i improves the prediction of cell j's signal beyond the past signal of j alone and is determined using the pairwise asymmetric Granger Causality statistical test. (**B**) Visualization of the spatial single cell heterogeneity of the degree rank (in-degree + out-degree). The color scale is linear. (**C**) Heterogeneity in degree rank distribution. The Kernel Density Estimation (KDE) of the degree rank distributions of 10 null models that considered random shuffling of GC edges while preserving the probability for an edge (green) versus the experimentally observed degree rank distribution (red). The raw distribution (input to KDE) is shown in Fig. S1.3A, with Rinku index ~29 versus ~25 for the observed and null model correspondingly. (**D**) Example of collective (top) and local (bottom) heterogeneity for three different network structures. Networks are ordered from left-to-right according to their heterogeneity levels measured with (Jacob et al., 2017) (collective) and (Estrada, 2010) (local). Graph (I) node degree ranks are (2,2,2,2,2,2): local heterogeneity = 0, collective heterogeneity = 0. Graph (II) node degree ranks are (1, 4, 2, 2, 3): local

heterogeneity ≈ 0.38, collective heterogeneity ≈ 1. Graph (III) node degree ranks are (1,1,1,1, 4): local heterogeneity = 1, collective heterogeneity ≈ 0.59. See Methods for full details. (**E**) Pairwise associations between two heterogeneity measures (local heterogeneity, collective heterogeneity), adaptation rate and GC edge probability. Edges color represents the level of association, as quantified by the magnitude of correlation coefficients. Color scale is linear. Note that some edges reflect positive correlations (e.g., collective heterogeneity - GC edge probability) while others reflect negative correlations (e.g., local heterogeneity – adaptation rate). N = 23 biological replicates, across shear stress levels, that passed the stationarity criterion were considered to calculate correlations. See full data (with signed correlations) in Fig. S1.4.

To avoid spurious cause-effect relations, Granger Causality requires the time-series being analyzed to be stationary, i.e., fluctuating signals with a consistent mean and variability. Therefore, we excluded experiments where less than 85% of the cells passed two stationary tests (Kwiatkowski–Phillips–Schmidt–Shin (Kwiatkowski et al., 1992) and Augmented Dickey–Fuller (Cheung and Lai, 1995); Fig. S1.2A, Methods) and in the remaining experiments we analyzed only the cells that passed both stationary tests. When one cell's calcium dynamics significantly contributed to the accurate prediction of another cell's signal, we defined a directed GC edge from the first cell to the other (Methods). For every cell in the monolayer, we calculated the *degree rank* as a measurement for the cell's involvement in influencing or being influenced-by cells in its local vicinity -- cells with topological distance up to two (nearest neighbor cells and next-to-nearest neighbor cells, Methods, Fig. S1.2B-C). Cells took different roles in the multicellular communication network as indicated by the spatial heterogeneity in their degree ranks (Fig. 1.2B), which was higher than a null model that considered random shuffling of GC edges (Fig. 1.2C, Fig. S1.3A-B, Methods), and was only associated very weakly with the number of cell neighbors (Fig. S1.2D).

To quantitatively explore the role of heterogeneity in the cells' degree rank, we correlated four metrics that characterized adaptation, information flow, collective and local heterogeneity respectively. (1) The adaptation rate measures the dynamics of the multicellular adaptation to external mechanical stimuli (Fig. 1.1E). (2) The *GC edge probability*, or *P(GC edge)*, is the probability of a GC edge from all potential edges, a proxy for the overall information flow within the multicellular network. (3) The *collective heterogeneity* is a measurement for the variability of the cells' degree ranks (Jacob et al., 2017). The collective heterogeneity is calculated directly from the network's degree distribution and provides a normalized measure that is independent of the network's topology and size (Fig. S1.3B, see Methods for full details). For example, a network in which all the nodes having the same degree is considered as completely homogeneous while a more complex network such as scale-free that has a degree distribution approximates as a power-law (Amaral et al., 2000) is considered a more heterogeneous network (Fig. 1.2D – top). (4) The *local heterogeneity*, or the *Estrada index*, measures the degrees differences between all pairs of communicating cells capturing the heterogeneity in the local network's structure (Estrada, 2010) (see Methods for full details). The Estrada index is equal to zero for regular networks, where all neighboring cells have the same degree, and equal to one for star graphs (Fig. 1.2D - bottom). The observed local heterogeneity of all experiments spatially shuffled the cells' neighbors while preserving the same degree rank (Methods) implying higher local homogeneity (Fig. S1.3C). Thus, in response to step-like increase in shear stress the multicellular network was characterized by collective heterogeneity and local homogeneity.

We pooled together the 23 experiments across the shear stress range of 0.1-1.6 Pa and correlated the four measurements (Table S1). Collective heterogeneity was correlated with the GC edge probability while the local heterogeneity was negatively associated with the adaptation rate as well as with the GC edge probability. The pairwise correlations are depicted in Fig. 1.2E and detailed in Fig. S1.4. Cumulatively, our results suggest a transition from local to global scales in the multicellular network organization. Rapid adaptation is associated with local homogeneity, but has a marginal correlation with the collective heterogeneity. Active information flow is associated with both collective heterogeneity and local homogeneity in communication. The scale-dependent dynamics suggest propagation and integration of information from nearby cells into a decentralized network architecture, a mechanism we further investigate.

Gap-junction mediated multicellular synchronization to periodic mechanical stimuli

After characterizing the communication networks exhibited by endothelial cell monolayers to shear stress, we asked if the network could be trained to adapt to time-dependent external stimuli. To this end, we extended our assay to multiple rounds of repeated mechanical stimuli (Video S2). By treating each round as an independent *cycle,* and comparing single cell responses across cycles, we could focus on the evolution of synchronization in the multicellular system (Fig. 1.3A, Methods). We found that the HUVEC monolayer reinforced synchronization as observed by the gradual decrease in the standard deviation of the cells' calcium dynamics $\sigma_{\widehat{R_i}(t)}(t)$ (Fig. 1.3B). To confirm the role of intercellular communication in multicellular synchronization, we inhibited gap junctions or reduced cell density (Methods). In both cases the multicellular network failed to effectively synchronize (Fig. 1.3C-D, S1.5A-B).

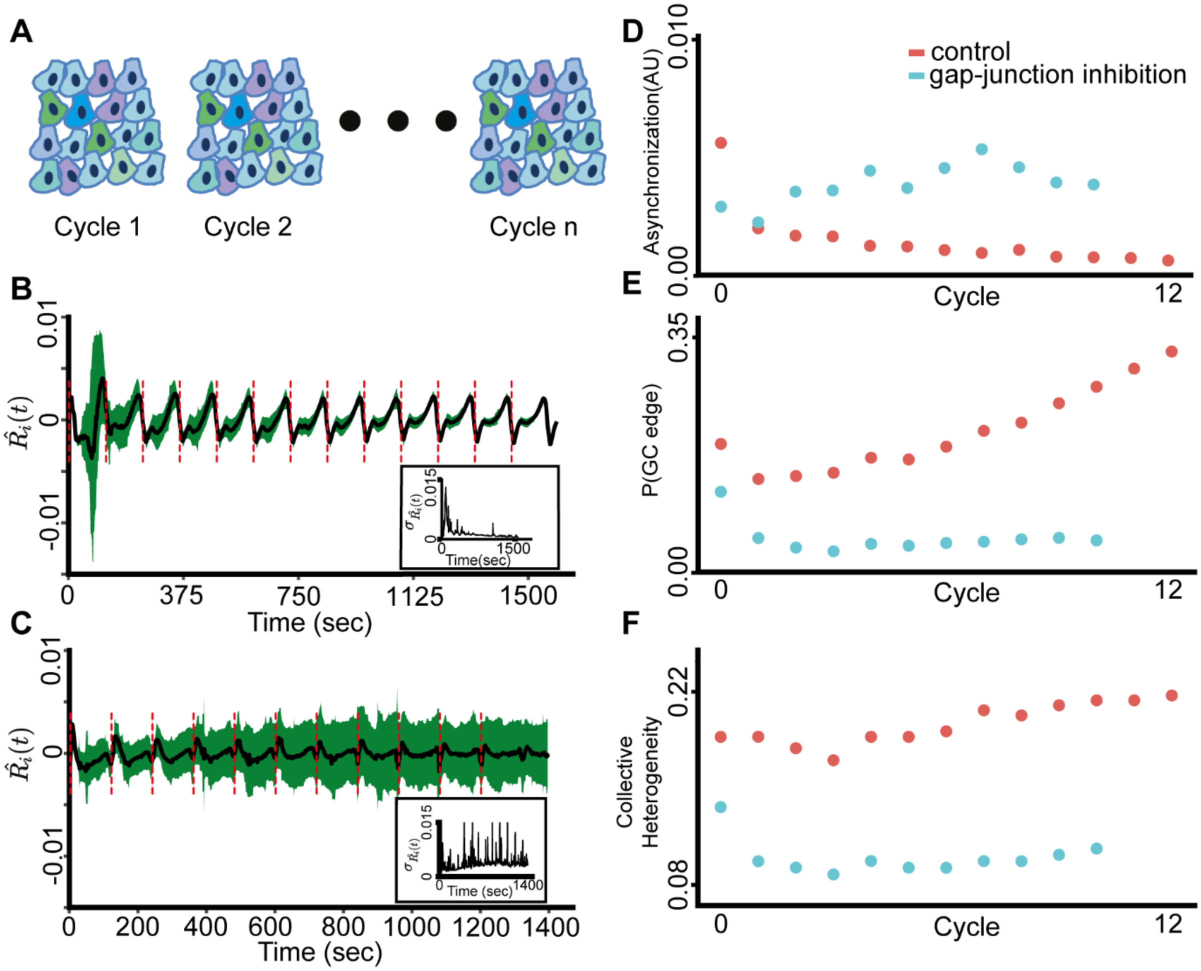

Figure 1.3. Information flow and collective heterogeneity are associated with multicellular synchronization to periodic mechanical stimuli. The shear stress was applied from the onset of the experiment (t = 0). (**A**) Depiction of the periodic mechanical stimuli experiment setup that included 13 cycles of continuous shear stress in 10 biological replicates (Methods). (**B**) Multicellular calcium dynamics is synchronized over time to periodic external mechanical stimuli. In total there are 13 cycles. Black: mean calcium dynamics; Green: standard deviation; Red dashed lines: shear stress onsets. Inset: standard deviation of calcium dynamics over time. (**C**) Gap junctions are required for multicellular synchronization. The calcium dynamics fail to synchronize following gap-junction inhibition. Representative of two experiments. Black: mean calcium dynamics; Green: standard deviation; Red dash lines: shear stress onsets. Inset: standard deviation of calcium dynamics over time. (**D**) Multicellular calcium dynamics synchronized over time for control (red) (Pearson coefficient = -0.7067, p-value < 0.007) but not for gap-junction inhibited (cyan) monolayers (Pearson coefficient = 0.6442, p-value < 0.0325). (**E**) Information flow increased over time for control (red) (Pearson coefficient = 0.9054, p-value < 0.0000207) but not for gap-junction inhibited (cyan) monolayer (Pearson coefficient = -0.3726, p-value

< 0.25898). (**F**) Collective heterogeneity increased over time for control (red) (Pearson coefficient = 0.8836, p-value < 0.000062) but not for gap-junction inhibited (cyan) monolayer (Pearson coefficient = -0.2376, p-value < 0.4818).

Synchronization coincided with a gradual increase of the information flow, i.e., the cell's mean GC edge probability (Fig. 1.3E), and with the collective heterogeneity (Fig. 1.3F) in intercellular communication. These relations were not measured upon gap-junction inhibition and sparser cell seeding (Fig. 1.3E-F, Fig. S1.5C-D, Fig. S1.6). We did not observe a clear pattern in the local homogeneity measure (Fig. S1.7). These results, summarized in Table S2, indicate the multicellular network gradually synchronizes to cycles of external mechanical stimuli in a local mechanism that is consistent with jap-junction mediated communication.

Functional cell memory: cells maintain their states in the communication network and reinforce them over time

To characterize the asymmetric communication roles that single cells take during the multicellular synchronization we calculated for each cell the transmission score and the receiver score as measures for being influential or influenced-by cells in its local vicinity (up to topological distance of two). We defined the transmission score as the probability of outgoing GC edges, and the receiver score as the probability of ingoing GC edges (Fig. 1.4A) (Methods). The observed trend of improved synchronization coincided with a gradual increase of the (population) mean receiver and transmission scores over time (Fig. 1.4B, Video S1.3, Video S1.4).

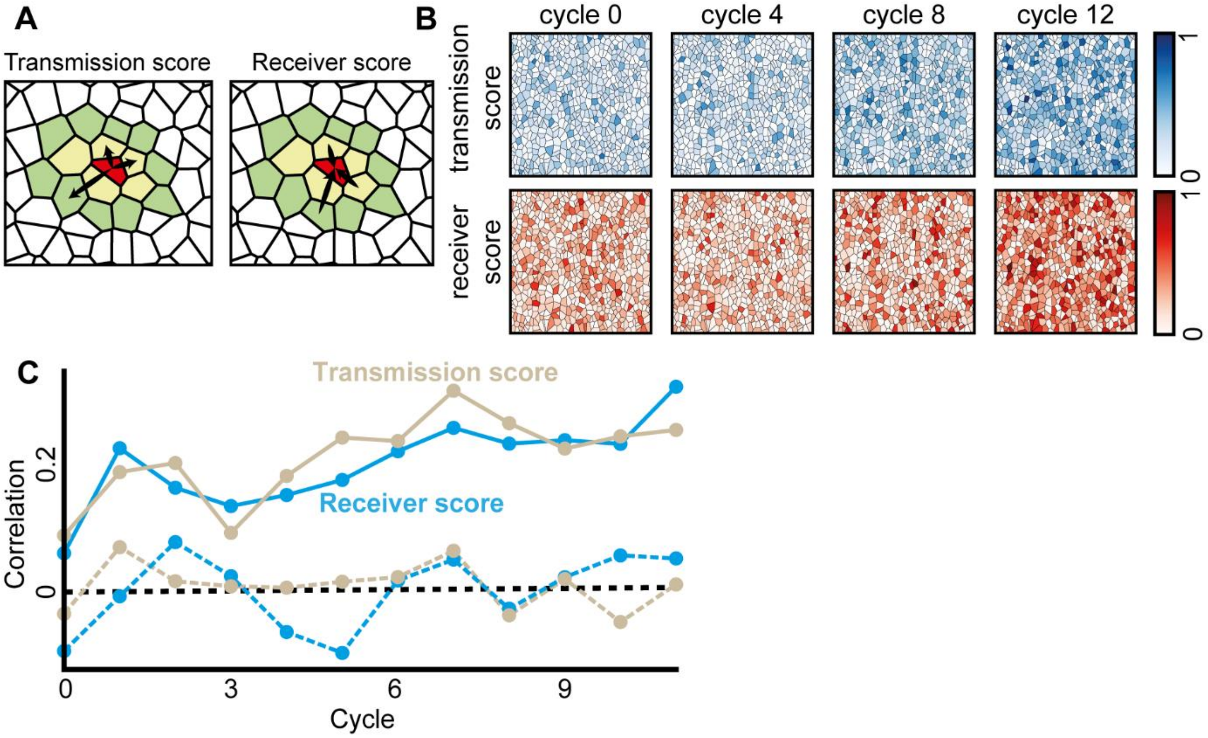

Figure 1.4. Functional cell memory is reinforced over time. (**A**) The transmission and the receiver scores were calculated as the probability for a significant outgoing (respectively, ingoing) Granger Causality edge at topological distance of up to two (nearest (yellow polygons) and next-to-nearest neighbor cells (green polygons)). For example, the red cell in the center has total of 15 neighbors, 5 in topological distance 1 (yellow) and 10 in topological distance 2 (green). The transmission score of the red cell is 3(outgoing edges)/15 and receiver score is 3(ingoing edges)/15. (**B**) The mean transmission and receiver scores increased over the cycles. Shown are the cells color coded according to their transmission (top, blue) and receiver (bottom, red) scores. The color scale is linear. (**C**) Cells transmission and receiver scores were correlated across consecutive cycles (solid lines), reinforced over time (Pearson coefficient = 0.7512, $p < 0.0001$), and were a local cell property as validated with permutation analysis - shuffling the cells in the next cycle and calculating correlation (dashed line, see Methods). P-value for the significance of the memory ≤ 0.001 (except the first cycle: p-value of transmission and receiver score 0.021 and 0.15 correspondingly, and the third cycle's transmission score p-value of 0.017, Fig. S1.8A).

We next asked to what extent the communication properties of cells were intrinsic cellular properties. To this end we correlated single cells' transmission and receiver scores across the repeated mechanical stimulus cycles while testing the null hypothesis that these scores were assigned randomly between consecutive cycles. We found that single cells' transmission and receiver scores were strongly correlated between consecutive stimulus cycles, that this correlation gradually increased as cells underwent additional stimulus cycles (Fig. 1.4C, Fig. S1.8A), and could not be explained by the autonomous cells' response to the external mechanical stimuli (Fig. S1.9). Measuring single cell correlation between larger temporal gaps of 2-4 cycles did not show a dramatic diminishing pattern suggesting that the cellular memory is stable for time scales of at least 4-8 minutes, which is beyond the timescale required for the multicellular system to recover (Fig. S1.8B). These results suggest that cells maintain and gradually reinforce memory regarding their role in the multicellular communication network at the timescales relevant for collective synchronization.

Stability in single cell communication state and increased information flow lead to enrichment of highly communicating cells coinciding with the establishment of synchronization

We next aimed to characterize how single cell communication properties and memory contribute to multicellular synchronization. First, we normalized the transmission and receiver scores across the population and cycles by calculating the respective z-score - the number of standard deviations away from the mean (Fig. 1.5A, Methods). The normalized scores allowed comparison of cell communication properties across different cycles in the same experiment as well as between different experiments. Next, we partitioned the normalized transmission-receiver space into five regions and empirically assigned the cells to states according to the region they occupied. *Individual cells*, whose calcium dynamics were independent of cells in their local vicinity, have normalized transmission and receiver scores both below -0.5. *Common cells*, with average communication properties. *Leader cells*, with high transmission scores (transmission score > 0.5 and receiver score < 0.5), *follower cells*, with high receiver score (receiver score > 0.5 and transmission score < 0.5), and *communication hub cells*, characterized by both transmission and receiver normalized scores above 0.5 (Fig. 1.5A, Methods). This data-driven partitioning defined five distinct states that cells take in terms of information transfer in the multicellular communication network and enabled us to follow their evolution throughout the synchronization process (Fig. 1.5B-C, Video S1.5, Video S1.6). The combined effect of the increasing information flow and cell memory led to a gradual increase in the fraction of cells actively participating in communication: followers, leaders and communication hubs, along with decreased fraction of cells with reduced level of communication: common and individual (Fig. 1.5C).

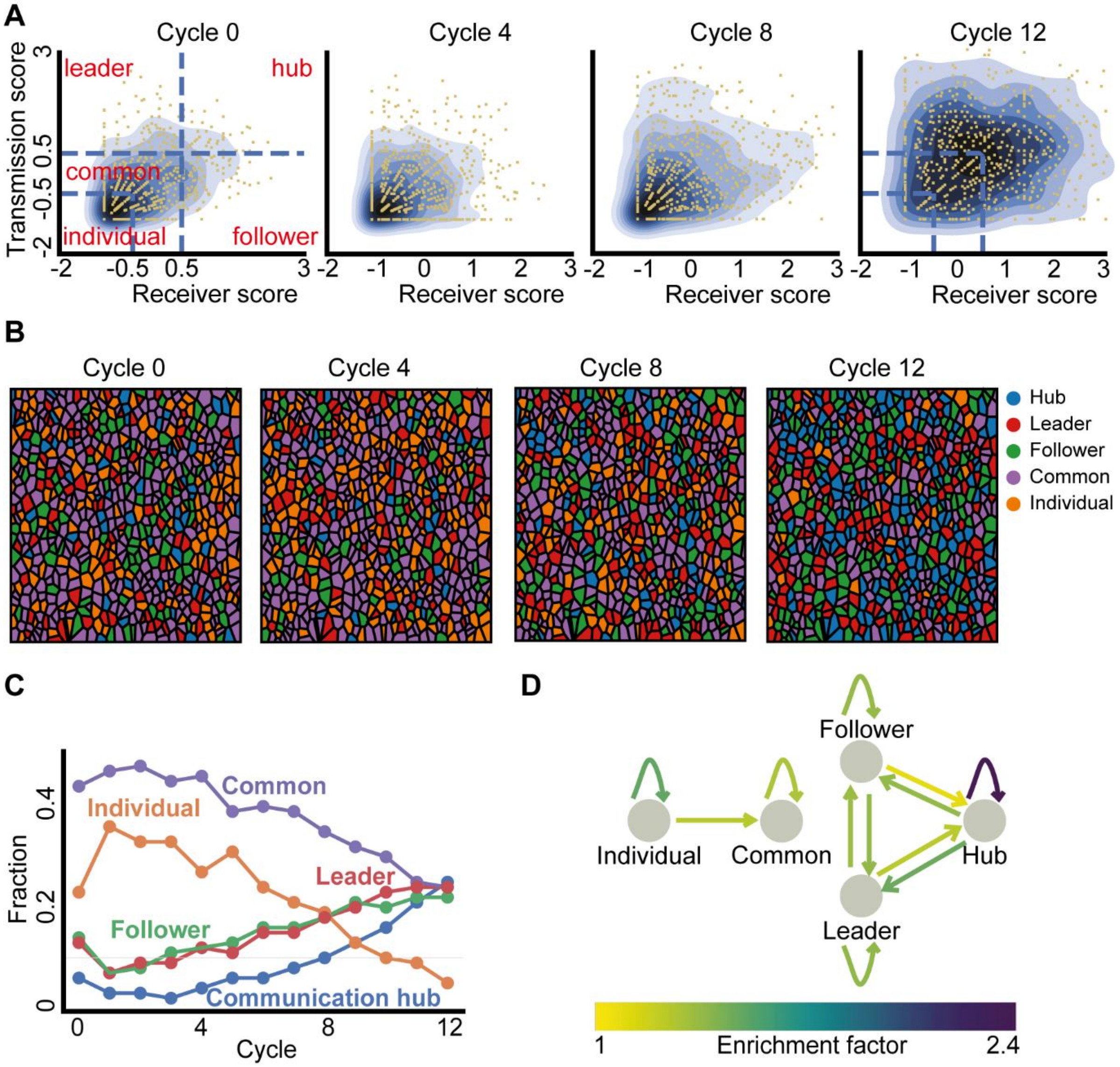

Figure 1.5. **Cells' communication states, state transitions and enrichment of communication hubs**. (**A**) Kernel density estimate plot visualization of the normalized transmission and receiver score over the cycles (blue gradient contours). Left: partitioning of the z-score normalized transmission-receiver space to five regions (blue dashed lines), each cell (yellow dot) was assigned to a group or "state" (red text) according to the region they resided at. Individual: transmission and receiver z-score < -0.5, Common: transmission z-score in the range of (-0.5, 0.5) and receiver z-score < 0.5 or receiver z-score in the range of (-0.5, -0.5) and transmission z-score < 0.5. Leader: transmission z-score > 0.5 and receiver z-score < 0.5. Follower: receiver z-score > 0.5 and transmission z-score < 0.5. Hub: transmission and receiver z-score > 0.5. (**B**) Visualizing the cells' communication states over the cycles with color code. (**C**) Fraction of cells at each communication state over the cycles. (**D**) Enrichment factors of cellular state transition. Depiction of the single cell transitions between states that were enriched beyond the expected values of a null model. The null model was based on the marginal distribution of the states (Fig. S1.10, Methods). Shown are edges with fold increase over 1 (linear color code).

To follow the dynamic trajectory of single cells between communication states we analyzed the probability of transitioning from one state to another in consecutive cycles. In particular, we computed the enrichment factor - transition probabilities between any two states and normalized the quantity by the fully random transition probabilities (Methods, Fig. S1.10). As expected from our earlier observation of functional memory (Fig. 1.4C), we found that cells tended to maintain their states or “similar” states, as reflected by self-transition enrichment factors above one (Fig. 1.5D, Fig. S1.10). Generally, single cells followed a temporal trajectory from the states characterized with less communication capacity to states with increased communication (Fig. 1.5D - showing edges only for enrichment factors > 1). We also found symmetric transition folds between the follower-and leader states, and the transition from communication hub to the follower/leader state was enriched compared to the opposite transition to a communication hub (Fig. 1.5D, Fig. S1.10).

We next focused our attention to the fraction of cells taking the “communication hub” role. Low fraction of communication hubs at the onset of the experiment rapidly increased to become a frequent state in later cycles (Fig. 1.5C) coinciding with the gradual increase in information flow (Fig. 1.4B). Moreover, the communication hub state was found to be much more stable than other states or transitions (2.4 fold dwell probability compared with a fully random process), underpinning their rapid spread in the population (Fig. 1.5C). Altogether, increased information flow along with stable functional memory led to enrichment of communication hubs that contribute to effective spread of information in the multicellular network.

Information gradually propagates from the (local) single cell to the (global) multicellular scale

Our data suggests multicellular synchronization is associated with various single cell properties such as communication state and memory. This led us to the hypothesis that the synchronization process is driven by effectively propagating information from the local scale (between single cells), to the global (collective) scale. To test this hypothesis, we measured to what extent local cell properties explained the information flow in the multicellular network. First, we computed the neighboring pair cross correlation coefficients for direct observations and spatially permuted data. We found that the spatial permutation always decreased the cross correlation, therefore cross correlation was maintained as a local cell property throughout the experiment even in the presence of common external stimuli (Fig. 1.6A, upper-left inset). Spatial permutation decreased the GC edge probability in early cycles but increased the edge probabilities in later cycles (Fig. 1.6A main panel and the lower-right inset). These results indicate that once neighboring cells reach sufficient synchronization their ability to influence each other is less effective than cell pairs far apart. We validated these observations more systematically by correlating the topological distance between pairs of cells to their GC edge probability (Methods). This analysis established that at the onset of the experiment, the information flow is dominated by local cell-cell interactions and is gradually transitioning to the global scale as the multicellular network synchronizes (Fig. 1.6B).

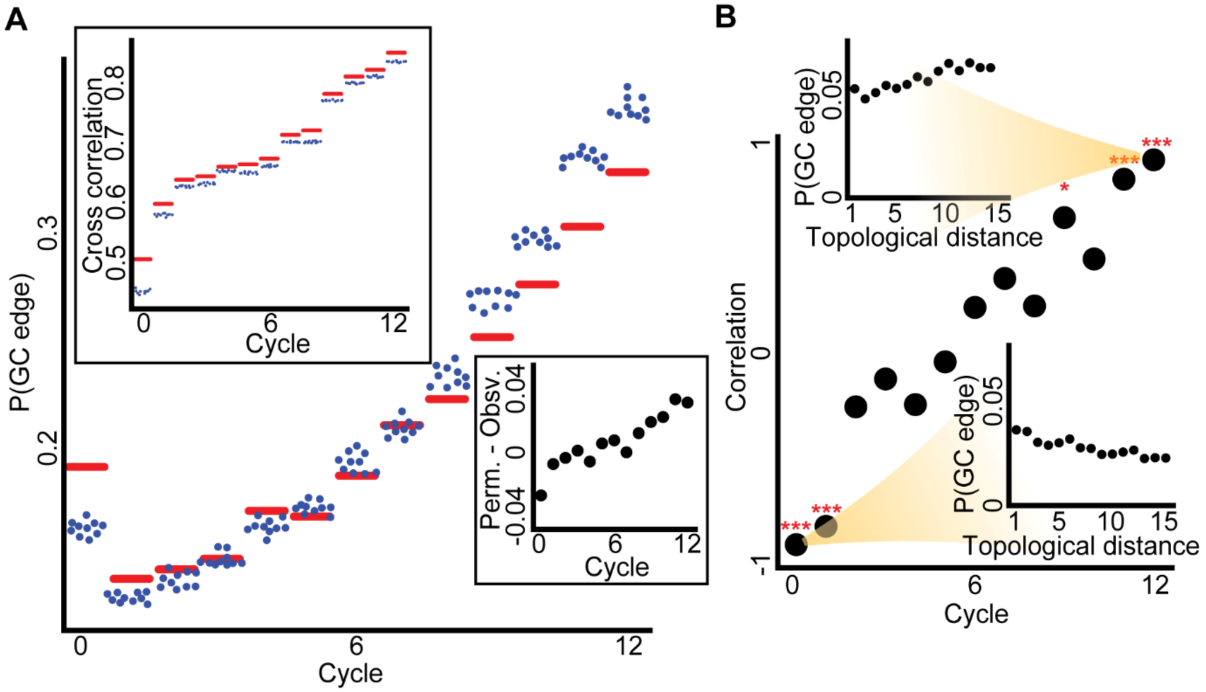

Figure 1.6. Gradual local to global transition in information spreading. (**A**) Main panel: the observed versus permuted Granger causality edge probability, P(GC edge), over the cycles. Upper left panel: the mean observed versus mean permuted neighbor cross correlation over the cycles. For both panels the red horizontal line is the experimental observation, while each blue dot is the result of one of ten independent spatial cell permutations. Bottom right inset: experimental GC edge probability subtracted from the mean permuted GC edge probability using the same data as in the main panel. Through cycles 0 to 12 Pearson coefficient = 0.94, p-value < 0.0001. (**B**) In the main panel each dot represents the Pearson correlation between the topological distances of pairs of cells to the corresponding GC edge probability in a given cycle. Through cycles 0 to 12 Pearson coefficient = 0.964, p-value < 0.0001. *** - p-value < 0.0001, * - p-value < 0.05, for Pearson correlation significance test. Insets show the P(GC edge) as a function of the topological distance between cell pairs for the first (bottom right) and last (top left) cycles. For this

analysis, we randomly selected for each cell at each topological distance at most ten neighboring cells due to computational cost and performed FDR multiple hypotheses correction (see Methods for full details).

Discussion

The emergence of robust multicellular behaviors from heterogeneous single cell dynamics is a poorly understood, but fundamentally important phenomenon in living systems (Zinner et al., 2020). Here we provide insights in bridging the scales between local cell-cell communication and global multicellular synchronization. This was achieved by measuring asymmetric information transfer at single cell resolution in multicellular monolayers under externally applied mechanical stimuli. By employing Granger Causality to systematically quantify the communication of a cell with other cells in their local environment, we defined for each cell its capacity to transmit and to receive information in the multicellular communication network. Our method relies on local pairwise analysis of cell dynamics, and defines single cell communication properties without requiring explicit construction of the network or committing to a specific network architecture. This model-free data-driven approach can be applied to a broad set of biological systems from synchronized beating of cardiomyocytes (Nitsan et al., 2016), intercellular communication through the microenvironment (Nahum et al., 2023), brain activity (Seth et al., 2015), molecular signaling (Goglia et al., 2020) and coordinated cell migration (Malinverno et al., 2017).

We showed the cells were actively communicating with one another locally, and that physical cell-cell contacts via gap-junctions were required for multicellular synchronization. These conclusions were supported by multiple lines of evidence throughout our study. First, we reported that gap-junctions and sufficient cell confluence were required for multicellular synchronization (Fig. 1.3B versus Fig. 1.3C or Fig. S1.5 and Table S1.2). Second, we demonstrated that both local and collective heterogeneity depended on the spatial organization of cells in their vicinity (Fig. S1.3). Third, we found that the activation time, a cell's autonomous response to the external stress, was not associated with the transmission or receiver score (Fig. S1.9A), which would also be conflicting with the gradual increase fraction of communication hubs (which are both leaders and followers). Forth, cells "remembered" and reinforced their roles in the multicellular communication network over time, as a local, spatially-dependent property (Fig. 1.4C, Fig. S1.8), but did not "remember" their activation time in previous cycles

(Fig. S1.9B). Fifth, neighbor pair cross correlation was a local cell property throughout the experiment (Fig. 1.6A). Together, our data established the decoupling of the local cell-cell communication from the external stimuli, and established that the emergence of multicellular synchronization required gap-junction mediated local cell-cell communication.

Our data reveal that single cells take different roles in cell-cell communication ("division of labor"), which we defined as communication states in the context of collective mechanosensing. Cells gradually reinforce their state ("functional cell memory"), and increase the connectivity ("information flow") in the multicellular network. These three mechanisms work in concert to facilitate the emergence of multicellular synchronization. Our results suggest that while cell heterogeneity expands the dynamic range of mechanoresponses, functional memory stabilizes the dynamics against intrinsic and extrinsic noise and that information flow sustains and reinforces the multicellular dynamics.

We found that heterogeneity in cells' communication properties were associated with improved convergence to synchronization (Fig. 1.2E, Fig. 1.3F). We also observed that the fractions of cells at each functional state, excluding individuals, became more balanced through periodic cycles (Fig. 1.5C), in agreement with our conclusion that heterogeneity constructively contributes to the synchronization of a noisy multicellular system. Heterogeneity among cells could arise from stochastic gene expression levels, signaling kinetics, physiological states such as cell cycle, and/or microenvironmental cues (Cheng et al., 2015; Gut et al., 2018; Gut et al., 2015; Muldoon et al., 2020; Hasenauer et al., 2011; Paszek et al., 2010; Tay et al., 2010). Although our data does not exclude a particular source of heterogeneity, the alteration of cellular communication state at a short time scale (~10 minutes) suggests pathway kinetics, such as the cross-talk between gap junction and mechanotransduction, may be important factors to determine both local and global heterogeneities.

Previous studies have reported multiple sources of microenvironment-dependent cell memory. For instance, cells can remember past mechanical properties of their substrate, which influence their differentiation (Yang et al., 2014). Cells can also sense changes in their extracellular signal by remembering past extracellular stimulation via a receptor-mediated mechanism (Lyashenko et al., 2020), and past growth-promoting stimuli can affect cells' future signaling responses (Spinosa et al., 2019). In the context of collective cell migration, a recent study showed that cells remembered their polarized state independently of cell–cell junctions (Jain et al., 2020), and another study revealed associative memory of electric field and chemoattractant at stimuli in a unicellular organism migration patterns (De la Fuente et al., 2019). In our study, single cell memory of communication properties contributes to the temporal evolution of the multicellular network to its synchronized state. The dissociation between a cell's activation time and its functional role in information processing underpins the dynamic nature of memory, which is also consistent with the unidirectional evolution of the multicellular network (Figs. 1.5-6). While further investigations are required to reveal the molecular mechanisms of the cellular memory, we suspect slowed gap junction turnover, as well as the continuously perturbed calcium dynamics from fully relaxation, may contributed to the reinforced functional role of cells.

Our study reveals a self-organized multicellular network that supports information flow from local to global scales. Such information may be carried by two main signaling mechanisms, juxtacrine (contact-dependent) and autocrine (secreted-dependent) (Fancher and Mugler, 2017). A juxtacrine channel allows a cell to establish conversation with its (physically touching) immediate neighbors without interference from extracellular space. For HUVEC cells such communication can be realized by gap junctions (Okamoto et al., 2017). On the other hand, an autocrine channel allows a cell to broadcast its information through diffusive messengers in the extracellular space. For HUVEC cells stress-triggered ATP release and ATP-induced calcium dynamics constitute an autocrine pathway (Yamamoto et al., 2011). While both mechanisms could contribute to the information flow within the multicellular network, we suggest gap-junction and contact-dependent signaling as the dominant mechanism (Fig. 1.3B versus Fig. 1.3C or Fig. S1.5). While a recent study suggested that positive feedback of a diffusive signaling mechanism can drive accelerated, long-range information transmission (Dieterle et al., 2020), the external flow in our system is likely to rapidly dilute the diffusive messenger (Gregor et al., 2010). The contact-dependent information flow hypothesis is also supported by our previous studies where we demonstrated that blocking gap junctions, or inserting weakly communicating cells impaired the information flow (Potter et al., 2016; Sun et al., 2012).

Altogether, our results suggest the following phenomenological model for multicellular synchronization. Cells are gradually "learning" the local network structure around them (heterogeneity), adjusting their internal state, reinforcing it (memory), and thus stabilizing the network architecture. This stabilized network structure reduces conflicting communication interferences and thus promotes enhanced spread of information from the local to the global scale to eventually synchronize the group.

Acknowledgements

This work was supported by the Israeli Council for Higher Education (CHE) via Data Science Research Center, Ben-Gurion University of the Negev, Israel (to AZ), by the Wellcome Leap Delta Tissue program (to AZ) and by the National Institute of General Medical Sciences grant R35GM138179 (to BS). GL is supported by National Science Foundation Grant PHY-1844627. Part of this research was conducted at the Northwest Nanotechnology Infrastructure, a National Nanotechnology Coordinated Infrastructure site at Oregon State University which is supported in part by the National Science Foundation (grant NNCI-1542101) and Oregon State University. We thank Kevin Dean for critically reading the manuscript.

Author Contributions

Assaf Z and BS conceived the study. GL and KC designed the experimental assay and performed all experiments. Amos Z developed analytic tools, analyzed, and interpreted the data. Assaf Z, BS and Amos Z drafted the manuscript. BS and Assaf Z mentored the authors. All authors wrote and edited the manuscript and approved its content.

Declaration of Interests

The authors declare that they have no competing interests.

Main tables and legends

Index	Tag	Shear stress (Pa)	Stationarity level	Adaptaion rate	K	Information flow (P(GC Edge))	Local heterogeneity	Collective heterogeneity	std_length	t_max_std	adaptation_rate_eow
0	step_shear_data_1_mbar_2016_10_12_Exp_06	0.1	0.93715342	0.692624934	0.006140391	0.348634454	0.056993983	0.240203442	1170	298	698
1	step_shear_data_1_mbar_2016_10_12_Exp_01	0.1	0.909090909	0.61304193	0.005902869	0.353039785	0.055284062	0.231127128	1170	34	434
2	step_shear_data_1_mbar_2016_10_12_Exp_02	0.1	0.990176817	0.627121604	0.005417284	0.24814775	0.05242682	0.226925513	1170	752	1152
3	step_shear_data_1_mbar_2016_10_12_Exp_03	0.1	0.977739726	0.597913552	0.005768709	0.306559821	0.046027945	0.215776206	1170	104	504
4	step_shear_data_1_mbar_2016_10_12_Exp_04	0.1	0.911858974	0.649075447	0.006212594	0.333240145	0.051548545	0.216277776	1170	252	652
5	step_shear_data_1_mbar_2016_10_12_Exp_05	0.1	0.93418259	0.607828648	0.004919776	0.280601723	0.060495673	0.244814568	1170	154	554
6	step_shear_data_2_mbar_2016_08_15_Exp_03	0.2	0.993065187	0.502713762	0.000305813	0.075363399	0.069039626	0.140354321	1170	166	566
7	step_shear_data_2_mbar_2016_08_15_Exp_02	0.2	0.955223881	0.602952628	0.002065015	0.131702939	0.073783469	0.148050358	1170	256	656
8	step_shear_data_2_mbar_2016_08_15_Exp_01	0.2	0.950540958	0.37301204	0.001075519	0.507400313	0.059334239	0.246192534	1170	128	528
9	step_shear_data_2_mbar_2016_07_24_Exp_03	0.2	0.855696203	0.551251537	0.005044173	0.345339652	0.066505894	0.294684506	1170	84	484
10	step_shear_data_2_mbar_2016_07_24_Exp_05	0.2	0.957792208	0.740846352	0.006949409	0.3857512	0.05065111	0.292253208	1170	418	818
11	step_shear_data_2_mbar_2016_08_24_Exp_03	0.2	0.888257576	0.423498884	0.002848752	0.159711075	0.080955874	0.180373461	1170	78	478
12	step_shear_data_2_mbar_2016_07_24_Exp_02	0.2	0.859060403	0.652434561	0.001303614	0.607826457	0.053116282	0.349556566	1170	424	824
13	step_shear_data_2_mbar_2016_08_24_Exp_05	0.2	0.907246377	0.794099388	0.021710105	0.55177717	0.042020167	0.235310541	1170	522	922
14	step_shear_data_6_mbar_2016_07_28_Exp_03	0.6	0.962219599	0.405864233	0.00111814	0.52390206	0.059172836	0.236060298	1170	478	878
15	step_shear_data_6_mbar_2016_07_28_Exp_04	0.6	0.997047244	0.335411279	0.00153647	0.230186906	0.081415846	0.201366956	1170	194	594
16	step_shear_data_6_mbar_2016_08_12_Exp_01	0.6	0.886885246	0.334795914	0.001644794	0.442371883	0.091916326	0.247003392	1170	36	436
17	step_shear_data_6_mbar_2016_08_12_Exp_04	0.6	0.993966817	0.525408922	0.009795871	0.133842281	0.080528039	0.194999581	1170	504	904
18	step_shear_data_6_mbar_2016_08_12_Exp_02	0.6	0.907630522	0.403074369	0.001417176	0.122998829	0.069614714	0.147110323	1170	390	790
19	step_shear_data_6_mbar_2016_07_28_Exp_02	0.6	0.982995951	0.336648715	0.001400486	0.236709081	0.081282448	0.178042683	1170	458	858
20	step_shear_data_10_mbar_2016_08_17_Exp_05	1	0.92173913	0.368680141	0.001622162	0.085397366	0.083629721	0.115041099	1170	254	654
21	step_shear_data_10_mbar_2016_08_17_Exp_02	1	0.939271255	0.374059506	0.002307977	0.57177015	0.037480058	0.230001223	1170	380	780
22	step_shear_data_16_mbar_2016_08_10_Exp_02	1.6	0.853161844	0.729553891	0.008461452	0.121990262	0.056346402	0.127436678	1170	36	436

Table S1. Step experimental data table. Included are 23/47 experiments that passed the stationarity criteria (see Methods) across a shear stress range of 0.1-1.6 Pa. The following readouts were recorded for each experiment: shear stress (Pa), stationarity level (fraction of cells passing the stationarity criteria), adaptation rate (non-parametric and parametric), K (coefficient of the parametric exponential model), information flow (P(GC edge)), local heterogeneity (Estrada index), collective heterogeneity, std_length (the standard deviation in seconds), t_max_std (the peak time of standard deviation), and adaptation_rate_eow (the end of window time of the adaption rate: t_max_std + 400, see Methods).

Index	Tag	Treatment	Max shear stress (Pa)	# cycles	corr_async_vs_cycle	mean_async	mean_prob_gc_edge	corr_prob_gc_edge_vs_cycle	corr_mem_tr_vs_cycle	max_mem_tr	corr_mem_re_vs_cycle	max_mem_re	mean_local_heterogeneity	corr_collective_heterogeneity_vs_cycle	mean_collective_heterogeneity
0	oscillatory_shear_data_1_mbar_2016_11_10_Exp_03	control	0.1	13	-0.813876068	0.001470369	0.064211871	0.750468304	0.653312396	0.143189997	0.866893389	0.121625413	0.062621072	0.524200171	0.052096426
1	oscillatory_shear_data_1_mbar_2016_11_10_Exp_04	control	0.1	13	-0.973327092	0.002761506	0.064924541	0.932818277	0.489364533	0.11784741	0.773781743	0.108997819	0.06731085	0.932632268	0.075205862
2	oscillatory_shear_data_2_mbar_2016_11_10_Exp_01	control	0.2	13	-0.980176261	0.001790963	0.069045235	0.887429552	0.839644409	0.172848707	0.477148851	0.085757629	0.066391774	0.872910854	0.057985931
3	oscillatory_shear_data_2_mbar_2016_11_10_Exp_02	control	0.2	13	-0.929862531	0.001527613	0.080481273	0.934836706	0.465177984	0.157153815	0.139020592	0.126276511	0.066042594	0.711974324	0.060681375
4	oscillatory_shear_data_1_mbar_2016_25_10_Exp_01	control	0.1	13	-0.97513278	0.002353781	0.168055624	0.086741779	0.94688912	0.177094755	0.952595405	0.15846461	0.084703591	-0.049088934	0.092527147
5	oscillatory_shear_data_1_mbar_2016_25_10_Exp_02	control	0.1	13	-0.879508414	0.001959371	0.125031348	0.915085524	0.316705068	0.087501343	-0.222441542	0.070769837	0.102135834	0.692054587	0.093600152
6	oscillatory_shear_data_2_mbar_2016_25_10_Exp_03	control	0.2	13	-0.939439718	0.001239794	0.18987109	0.863796506	0.166951894	0.110089679	0.076248782	0.092473473	0.092308171	0.788426282	0.083026629
7	oscillatory_shear_data_2_mbar_2016_25_10_Exp_04	control	0.2	13	-0.963107165	0.001138419	0.230657917	0.806824163	-0.684485864	0.1164812	-0.295834181	0.040086956	0.077443342	0.680942711	0.081860833
8	oscillatory_shear_data_2_mbar_2018_08_05_Exp_02	control	0.2	13	-0.706718649	0.001465374	0.219930632	0.92484268	0.732863548	0.302751545	0.833962816	0.308651313	0.077427469	0.883686504	0.196427445
9	oscillatory_shear_data_2_mbar_2018_11_10_Exp_02	control	0.2	13	-0.791866816	0.002523907	0.183647543	0.252357028	0.582201098	0.206573806	0.55357875	0.317148809	0.083250485	0.417820144	0.100915864
10	HUVEC_10uM_palmitolei_acid_60s_2_mbar_HUVEC_10uM_Palmitoleic_acid_60s_exp	palmitoleic_acid	0.2	11	0.644202479	0.003825205	0.049929252	-0.37269041	0.189845863	0.096088215	-0.29684402	0.075912421	0.057790419	-0.237617506	0.099827201
11	HUVEC_10uM_palmitolei_acid_60s_2_mbar_HUVEC_10uM_Palmitoleic_acid_60s_exp2	palmitoleic_acid	0.2	11	0.659997726	0.004522818	0.04790104	0.88048978	0.744582726	0.076945615	0.615300834	0.093670811	0.056931751	0.831145464	0.098927966
12	HUVEC_10uM_palmitolei_acid_60s_2_mbar_HUVEC_reducedensity_60sonoff_exp	low_density	0.2	11	-0.856353665	0.00515809	0.041522578	-0.758139524	0.249537366	0.102525476	0.17061119	0.111699086	0.052136651	-0.651718994	0.119822805
13	HUVEC_10uM_palmitolei_acid_60s_2_mbar_HUVEC_reduced_density_60s_exp2	low_density	0.2	11	-0.683117126	0.003746724	0.046666053	-0.734306442	0.566127528	0.18433915	0.817198443	0.157552667	0.052001841	-0.517070479	0.117336578

Table S2. Cycle experimental data table. Included are 15 cycles experiments that include control n = 4 (1Pa), n = 6 (2Pa), gap-junction inhibition n = 2 (“palmitoleic_acid”), and low density n = 2 (“low_density”). The following readouts were recorded for each experiment: treatment, maximal shear stress (Pa), number of cycles, corr_async_vs_cycle (the Pearson correlation coefficient of the asynchronization over cycles), mean_async (the mean value of the asynchronization over cycles), mean_prob_gc_edge (the mean probability of GC edge over cycles), corr_prob_gc_edge_vs_cycle (the Pearson correlation coefficient of GC edge over cycles), corr_mem_tr/re_vs_cycle (the Pearson correlation coefficient of the transmission/receiver memory score over cycles, where the memory at cycle *i* is the Pearson correlation between the transmission/receiver score of *i* and *i+1*), max_mem_tr/re (the maximum value of the transmission/receiver memory score across cycles), mean_local_heterogeneity (the mean value of Esrada’s index over cycles), corr_collective_heterogeneity_vs_cycle (the Pearson correlation coefficient of the collective heterogeneity over cycles), mean_collective_heterogeneity (the mean value of the collective heterogeneity over cycles). Note that one gap-junction inhibition experiment (HUVEC_10uM_palmitolei_acid_60s_2_mbar_HUVEC_10uM_Palmitoleic_acid_60s_exp2) had high collective heterogeneity because it was dominated by cells without edges (see Methods) - 50% of the cells had a zero-degree rank.

STAR★Methods

Key resources table

REAGENT or RESOURCE	SOURCE	IDENTIFIER
Chemicals, peptides, and recombinant proteins		
TrypLE Select	Life Technologies	Cat#12604021
Palmitoleic acid	Sigma-Aldrich	Cat#76169
Dimethyl sulfoxide ≥99.9% USP, Multi-Compendial, J.T. Baker®	VWR	Cat#BDH1115-4LP
Krayden Dow Sylgard 184 Silicone Elastometer Kit (1.1lb)	Fisher scientific	Cat#NC9285739
EGMTM-2 Endothelial Cell Growth Medium-2 BulletKit	Lonza	Cat#CC-3162
ReagentPackTM Subculture Reagents, 100 mL	Lonza	Cat#CC-5034
Deposited data		
Raw and analyzed data	This work	https://doi.org/10.5281/zenodo.6568945
Raw data of gap-junction inhibition experiments	This work	https://figshare.com/s/2e2ba004102bdd96f414
Raw data of step function	This work	https://doi.org/10.6084/m9.figshare.19807864.v1
Raw data of step function	This work	https://doi.org/10.6084/m9.figshare.19807870.v1
Raw data of cyclic pressure	This work	https://doi.org/10.6084/m9.figshare.19807873.v2
Experimental models: Cell lines		
HUVEC – Human Umbilical Vein Endothelial Cells, Single Donor, in EGM™-2	Lonza	C2517A
Software and algorithms		
Source code and test data	This work	https://doi.org/10.5281/zenodo.6589859
Other		
Fluorescent calcium dye, Calbryte 520	AAT Bioquest	Cat#21130
CMOS camera	Hamamatsu	Flash 2.8
PID-regulated pressure pump	Elveflow	OB-1
flow sensor	Elveflow	BFS
NE-1000 One Channel Programmable Syringe Pump	New Era Pump Systems	Model#NE-1000
Corning BioCoat Collagen I-coated Flasks T-25 50/cs	VWR	Cat#12777-072

Flow switcher- 2 switch	Fluigent	

Resource availability

Lead contact

Further information and requests for resources and reagents should be directed to and will be fulfilled by the Lead Contact, Assaf Zaritsky (assafza@bgu.ac.il).

Materials availability

This study did not generate new materials.

Data and code availability

- Raw imaging data from a few representative experiments (step, cyclic, cyclic with gap junction inhibition), and all the processed data have been deposited at Zenodo and is publicly available. The rest of the raw imaging data will be available from the Lead Contact upon request. DOIs are listed in the key resources table.
- All original code has been deposited at GitHub and is publicly available. DOIs are listed in the key resources table.
- Scripts used to generate the figures presented in this paper are not provided in this paper but are available from the Lead Contact upon request.
- Any additional information required to reproduce this work is available from the Lead Contact upon request.

Experimental model and subject details section

Cell culture

Human Umbilical Vascular Endothelial Cells (HUVEC) were purchased from Lonza and were cultured following the vendor’s instructions. To prepare samples, cells were detached from culture dishes using TrypLE Select (Life Technologies) and suspended in growth mediums before being pipetted into the microfluidics devices at cell density of approximately 1800-2000 cells/mm^2 at 100% confluence (600-800 cells/mm^2 at 30%-50% confluence in the lower density experiments) allowing the cells to form monolayers. After overnight incubation, fluorescent calcium dye (Calbryte 520, AAT Bioquest) was loaded for 40 minutes prior to imaging. Palmitoleic acid (Sigma-Aldrich, MO) was used as gap junction inhibitor in our experiments. Palmitoleic acid was first dissolved in DMSO and then diluted to 10uM in growth medium. Before experiment, cells were treated with 10uM palmitoleic acid for 8 to 12 hours while seeding into the PDMS device. Then, 10uM palmitoleic acid was added to growth medium used for shear-stree experiments.

Methods details

Microfluidics

The organic elastomer polydimethylsiloxane (PDMS, Sylgard 184, Dow-Corning) used to create the microfluidic devices was comprised of a two part mixture - a base and curing agent - that were mixed in a 10:1 ratio, degassed, and poured over a stainless steel mold before curing at 65◦C overnight. Once cured, the microfluidic devices were cut from the mold, inlet/outlet holes were punched, and the device was affixed to a No. 1.5 coverslip via corona treatment. The cross section of the flow chambers was rectangular (2 mm X 1 mm). See Fig. 1.1A for depiction.

Applying controlled shear stress on the cells

The microfluidics flow rate was controlled by a PID-regulated pressure pump and was monitored using an inline flow sensor (Elveflow). To verify the stability of the flow profile we mixed 1 micrometer fluorescent particles in the solution and used particle image velocimetry to quantify the flow rate (Fig. 1.1B). To calculate the shear stress, we approximated the flow profile in the flow chamber as low-reynolds number pipe flow. We considered the cells in the field of view to experience uniform shear stress calculated at the center of the flow chamber. This was possible because the imaging window was narrow (470 μm) compared with the chamber width (1 mm).

In the “step” experiments we exposed the cells to a “step”-like shear stress of 0.1, 0.2, 0.6, 1 or 1.6 Pa for approximately 20 minutes. In the “cycles” experiments we applied multiple rounds of 2 minute long global external periodic mechanical stimuli. We limited the number of cycles for analysis to 13 at most, because of gradual accumulation of stage drifting and photo-damaging effects. Further experiments were performed to evaluate single cell calcium signal at the stimulation onset and its relaxation time after a single pulse (Fig. S1.11).

Live cell imaging

We imaged the calcium dynamics of HUVEC cells using a 20X magnification oil immersion objective lens (for step-stress experiments) and a 10X dry lens (for cyclic-stress experiments, to avoid flow-induced focus drift). The fluorescent images were captured with a CMOS camera

(Hamamatsu Flash 2.8) at 0.5 Hz and 1 sec exposure time. The images were stored as tif files of 960 X 720 pixels with physical pixel size of 0.65 µm X 0.65 µm (20X magnification) or 1.2 µm X 1.2 µm (10X magnification).

Measuring single cell calcium signaling

We manually annotated every cell center (Fig. 1.1A inset), and recorded the mean fluorescent intensity of approximately 40 μm^2 around the cell's center as a proxy of the intracellular calcium signal time-series of each cell. We normalized the calcium signal according to the approach described in (Sun et al., 2013) ("response curve normalization"). The response curve of each cell was defined as $R(t) = \frac{\Delta F}{F} = \frac{(F(t)-F_0)}{F_0}$, where $F(t)$ was calculated as the mean fluorescent intensity at time t, The baseline F_0 was calculated as the mean of the first 5 frames (10 seconds) of $F(t)$ before the mechanical stimulation was turned on. Temporal long-pass filter smoothed the R(t) time series to reduce the effects of outliers. Temporal smoothing was performed using Python's lowess function from statsmodels (statsmodels.nonparametric.smoothers_lowess) with the parameter frac=0.01. R(t) provides us with a dimensionless measure for the intracellular calcium magnitude relative to the cell's basal intensity.

To evaluate the change in the calcium signal in response to external mechanical stimulus we derived the cells' calcium signal in time: $\widehat{R_\iota}(t) \ = \frac{dR_i}{dt}(t) - \langle\frac{dR_i}{dt}(t)\rangle$, where $\langle\frac{dR_i}{dt}(t)\rangle$ is the mean value of $\frac{dR_i}{dt}(t)$, and $\frac{dR_i}{dt}(t)$ was calculated by Python's numpy convolution operator over the time series with the parameter values mode='same' and with a five point stencil filter [1, -8, 0, 8, -1] where the result was divided by constant of 12. A cell's calcium signal temporal derivative $\widehat{R_\iota}(t)$ was termed calcium dynamics.

The differentiation is necessary since both the exchange of IP3 and Ca^{2+} lead to a change of calcium concentration. Hence, the derivative is quantity directly related with communication (Sun et al., 2013; Sun et al., 2012). In addition, the derivative has properties such as: independent of basal level of signal, independent of slow systematic errors such as photo bleaching, and stationarity.

Measuring adaptation rate in “step” experiments

The adaptation rate is a non-parametric measurement for the speed that the multicellular system adapts to external stress. We defined the *adaptation rate* as $1 - \left(\frac{\int_{t_{max}}^{t_{max}+400} \sigma_{\widehat{R_\iota(t)}}(t)}{400 * \sigma_{\widehat{R_\iota(t_{max})}}}\right)$, where $\sigma_{\widehat{R_\iota(t)}}(t)$ is the population-level standard deviation of single-cell calcium dynamics $\widehat{R_\iota}(t)$ at time t after applying Hampel smooth function (Hampel, 1974) to remove outliers with the parameters of window size of 10 and threshold of 3σ, and $t_{max} = \underset{t}{argmax}\, \sigma_{\widehat{R_\iota(t)}}(t)$ is the time of the peak variability in calcium dynamics (Methods, Fig. 1.1E). When a system rapidly synchronizes, the adaptation rate approaches one. Conversely, if a system maintains a large deviation between the dynamics of individual cells, the adaptation rate is close to zero. In general, a higher adaptation rate implies faster multicellular adaptation to the external stress (Fig. 1.1E black curve adapts faster than blue curve). which measured the ratio between the area under the curve of ($\sigma_{\widehat{R_\iota(t)}}(t)$) from the peak variability in calcium dynamics over 400 seconds (Fig. 1.1E, the area marked in purple area or yellow + purple area for black and purple curve accordingly) with respect to the theoretical upper bound where the relative variability is zero (Fig. 1.1E, the combined areas marked in yellow, orange, and purple).

We choose a temporal window size of 400 seconds (200 frames) since several experiments had late peak times defining an upper bound on the temporal window (i.e., this was the maximal time-frame without excluding experiments, Table 1).

Measuring multicellular calcium adaption using a parametric exponential model

We devised an exponential parametric model to complement the non-parametric adaption rate measurement. We fitted the exponential model $A * e^{-Kt} + C$, to the standard deviation curve of the cell’s calcium dynamic using the non-linear least-squares method (Levenberg-Marquardt algorithm (Levenberg, 1944)). The initial coefficients values were set to A = 0.05, K = 0.01, C = 0. In experiments where the parameters failed to converge, we applied a linear least-squares fit to the logarithm of the signal. The coefficient K of the fitted model was used as the parametric measure for the adaptation rate.

Measuring synchronization in "cycle" experiments

We defined the *asynchronization* as a measure to quantify multicellular synchronization that relied on the standard deviation of single cell calcium dynamics at different time points ($\widehat{R_\iota}(t)$) in "cycle" experiments. Formally, we defined $\hat{R}(t) = \sum_{i=0}^{n} \frac{\widehat{R_\iota}(t)}{n}$, where *n* is the number of cells, as the mean calcium dynamic of all the cells at time *t* and $\sigma_{\widehat{R_\iota}(t)}(t)$ function as the standard deviation of the cells' calcium dynamic. The mean of $\sigma_{\widehat{R_\iota}(t)}(t)$ was calculated over the entire cycle time. Low values implied improved synchronization across the entire group.

Granger causality

Granger causality (GC) is a statistical method to quantify the information flow among multiple variables' time-series (Granger, 1969). Intuitively, time-series B is said to be "Granger causal" of time-series A, if the variability of A can be better explained by previous values of B and A, compared to using only previous values of A. Granger causality is an approximation to "transfer entropy" and under the assumption of Gaussian distribution it is exactly equivalent (Barrett et al., 2010).

Formally, given two-time series $x_i(t)$ and $x_j(t)$, where t ∈ Z. The autoregressive model of x_i is:

(1) $$x_i(t) = \sum_{k=1}^{p} \alpha_k x_i(t-k) + \varepsilon_i(t)$$

Where, p is the lag order, the number of previous observations used for prediction, α_k is the coefficient of x_i and ε_i is the prediction error at time t. The autoregressive model of x_i based also on the previous observations of x_j is:

(2) $$x_i(t) = \sum_{k=1}^{p} \alpha_{ik} x_i(t-k) + \sum_{k=1}^{p} \alpha_{jk} x_j(t-k) + \varepsilon_{ij}(t)$$

Where, p is the lag order,α_{ik} is the coefficient of $x_i(t-k)$, α_{jk} is the coefficient of $x_j(t-k)$ and $\varepsilon_{ij}(t)$ is the joint error of x_i and x_j predicting x_i.

Stationarity test

To avoid spurious causality connection, x_i and x_j both must comply with a stationary process before applying the granger causality test. Intuitively, stationary means that the statistical characteristics such as average and variance of a time series are independent of time. For each cell's $\widehat{R_\iota}(t)$ time series we applied two statistical tests for stationarity. First, Kwiatkowski–

Phillips–Schmidt–Shin (KPSS) (Kwiatkowski et al., 1992) tests the null hypothesis of stationarity against the alternative of unit root. Second, Augmented Dickey–Fuller (ADF) (Cheung and Lai, 1995) was applied as a complementary test for KPSS and tests the null hypothesis for unit root against the alternative of stationary. We excluded 24 of the 47 “step” experiments where less than 85% of the cells passed both the KPSS and the ADF stationary tests with significance of below 0.05 (Fig. S1.2A). From the remaining experiments we considered only cells with time-series that passed both stationarity statistical tests.

Pairwise calibration of the lag order

Granger Causality is based on linear regression and thus sensitive to the lag order, i.e., the number of past time frames used to make future predictions. In the context of a time-series, the autoregressive (AR) model is the estimator of the next time point value based on its own previous values. Higher lag-order reduces the bias but increases the variance while lower lag-order reduces the variance but increases the bias (Wooldridge, 2016). We selected the lag order, for each cell pair independently, as the minimal lag derived from four methods: Akaike information criterion (Akaike, 1973), Bayesian information criterion (Schwarz, 1978), Final Prediction Error (Akaike, 1970) and Hannan–Quinn information criterion (Hannan and Quinn, 1979). The minimum lag was selected to avoid overfitting without losing information backup by using Portmanteau test which checks for whiteness (i.e, the error does not contain a pattern) (Lütkepohl, 2005).

Granger causality statistical test

We applied a statistical test to infer granger causality between two $\widehat{R_\iota}(t)$ time series x_i andx_j (denoted, $GC_{x_j->x_i}$) (Granger, 1969). GC tests the null hypothesis that $x_j$is not contributing to the explained variance of x_i (Equation (2)) in relation to the model derived solely from past values of x_i (Equation (1)). This null hypothesis is rejected when at least one of the coefficients in equation (2) is different from zero. The statistic is based on the distribution:

$$(3) \qquad F_{value} = \frac{SSR_{Restricted} - SSR_{Unrestricted}}{SSR_{Unrestricted}} \left(\frac{T-k}{p}\right)$$

Where, $SSR_{Restricted}$ is the sum of square residuals of the model which take into account only self-previous observation of the random variable (Equation (1)), and $SSR_{Unrestricted}$ is the sum of square residuals of the other model which also takes into account the previous observation of the second random variable (Equation (2)). T is the sample size (number of observations in the time series used for prediction), p is the number of variables which was removed from the unrestricted model, in our case, the lag order, and k is the number of variables, in our case, twice the lag order. The null hypothesis is rejected when the F_{value} is larger than the F statistic (i.e., F's critical value) to conclude that $GC_{x_j->x_i}$. We derived the p-value from the F-statistic instead of directly using the F statistic to set up a global acceptance threshold.

Measuring collective heterogeneity

We measure the collective heterogeneity using the degree distribution of the network (Jacob et al., 2017). The measure characterizes the variability between the cell's degrees by measuring the variation of the probability for cells with each degree k, denoted P(k). Formally, the collective heterogeneity measure is defined as $H = \frac{\sqrt{\frac{1}{N}\sum_{k_{min}}^{k_{max}}\left(1-P(k)\right)^2}}{\sqrt{1-\frac{3}{N}}}$, where N is the overall number of cells, and the numerator is considered only for all k's such that $P(k) \neq 0$. The denominator is the approximate upper bound for N cells. The collective heterogeneity measure is bounded between 0 and 1 for large networks. $H = 0$, when all cells have the same degree (minimal heterogeneity). $H = 1$, for a specific network structure when the network's size converges to infinity, see (Jacob et al., 2017) for details. H could exceed the value of 1 for extremely small networks (see Fig. 1.2D). This measure is skewed for networks containing many vertices with zero degree because $P(k = 0)$ is high and the probability for other degrees $(k \neq 0)$ is low, maximizing the numerator (see gap-junction inhibition experiments in Table S2).

We defined the null model for the collective heterogeneity by random shuffling the GC edges (Fig. S1.3A). Formally, given a graph G and binary assignment of GC edge $\alpha\colon \left\{(v_i, v_j) \mid \forall\, v_i \in V(G)\ and\ v_j \in N_{\mathrm{v_i}}(1) \cup N_{v_i}(2)\right\} \rightarrow \{\alpha_1, \ldots., \alpha_s\}$, where $N_v(d)$ are the cells at topological distance d for cell v, $\alpha_i \in \{0,1\}$ is a binary edge assignment for all cell pairs at topological distance ≤ 2 from one another $\left\{(v_i, v_j) \mid \forall\, v_i \in V(G)\ and\ v_j \in N_{\mathrm{v_j}}(1) \cup N_{v_j}(2)\right\}$, and s is the number of such pairs. A random permutation was performed by shuffling the binary assignments. Observed collective heterogeneity was systematically higher than the null model (Fig. S1.3B).

Measuring local heterogeneity

We measure the local heterogeneity using the Estrada's index measure (Estrada, 2010). The measure focuses on the more local structural aspect of the network and is based on the Randić index score that is commonly used in chemistry for describing the molecule structure (Gutman et al., 2018). In contrast to the global collective heterogeneity that measures, Estrada index is based on the degree difference between all pairs of neighboring cells, thus capturing the heterogeneity in local network structure. Formally, the Estrada index is defines as $E = \frac{\sum_{i,j \in E}\left(k_i^{-\frac{1}{2}} - k_j^{-\frac{1}{2}}\right)^2}{n-2\sqrt{n-1}}$, where n is the number of cells and k_i is the degree rank of cell i. The Estrada index is bounded between 0 and 1. E = 0, when all cells have the same degree, and E = 1, for star topological structure, where one node has a degree of *n-1* and the other cells have a degree *1*.

We defined the null model for the local heterogeneity by spatially shuffling the cells' neighbors while preserving the same degree rank. We shuffle the cells' edges by rewiring two edges while preserving their degree. Formally, given two edges $e_i = (v_1, v_2)$ and $e_j = (u_1, u_2)$, a single rewiring is transforming e_i, e_j edges to $e_i' = (v_1, u_2)$ and $e_j' = (u_1, v_2)$. The rewiring function repeated $\left\lceil \frac{|E|}{2} * \log\frac{1}{\delta} \right\rceil$ times where the repeated factor δ is 10^{-6} following the rule of thumb termination criteria for generating independent random graph (Ray et al., 2015).

Calculating the transmission and receiver scores

The transmission and the receiver scores were calculated as the probability for an outgoing (respectively, ingoing) edge at topological distance ≤ 2 (nearest and next-to-nearest neighbor), where the topological distance was calculated using the Delaunay triangulation.

The transmission (denoted Tr) and receiver (denoted Re) scores were calculated independently for each cell c_i using its cell neighbours at topological distance one and two $N_{c_i}(1) \cup N_{c_i}(2)$:

$Tr(c_i) = \frac{\sum_{c_j \in N_{c_i}(1) \cup N_{c_i}(2)} 1_{GC_{c_i -> c_j}}}{\left|N_{c_i}(1) \cup N_{c_i}(2)\right|}$ and $Re(c_i) = \frac{\sum_{c_j \in N_{c_i}(1) \cup N_{c_i}(2)} 1_{GC_{c_i <- c_j}}}{\left|N_{c_i}(1) \cup N_{c_i}(2)\right|}$.

We treat each cell as an independent observation thus characterizing the role of each cell in the multicellular network without specifically committing on the exact network edges. To fix spurious edges due to multiple hypothesis testing we applied the strict Bonferroni correction that defines the edge significance threshold based on the number of edges considered (Bonferroni, 1936). In our case, with a significance threshold of 0.05 and n - number of potential edges we get a new significance threshold of 0.05/n. Edges passing this strict statistical test were termed *GC edges*.

The reason for using topological distances of up to two in calculating the transmission and receiver score is twofold. First, for analytic reasons and second due to irregularity in cell shape. Calculating the transmission and receiver score based on a small number of neighbors will increase the uncertainty. These neighborhood sizes were determined empirically for sufficient observations for statistics, and the expected short-range communication between the cells. Topological distance of two is a sweet spot in terms of reducing the false-positive errors. Specifically, increasing the number of neighbors makes the statistical test for determining GC edges stricter (from ~0.008 for topological distance of one to 0.003 for topological distance of two) because we use Bonferroni correction to determine statistical significance (Fig. S1.2B). This way, the statistical test also becomes less variable between cells since the variability in the number of neighbors also decreases.

A second reason for choosing to include next-to-nearest neighbor in the analysis due to the irregular shapes of the cells (Fig. S1.2C). Gap junctions often connect cells that are next-to-nearest neighbors as defined by Delaunay Triangulation. Nevertheless, the main results regarding heterogeneity, memory, and local-to-global information propagation held also when considering topological distance of size one (Fig. S1.12).

Note that the variance in the transmission and receiver scores gradually increased over time (Fig. S1.13). This result is in agreement with our results associating collective heterogeneity and synchronization.

Partitioning the normalized transmission-receiver space

The transmission and receiver scores of each cell were normalized across the population to allow direct comparison of single cell heterogeneity between cycles and between experiments. We calculated the receiver and transmission z-score for each cell c_i, the variation from the mean in units of standard deviations: Tr_norm(ci) = (Tr(ci)-μ)/σ, where μ is the mean transmission score across the population over all cycles, and σ is the standard deviation. The same normalization was applied for the receiver score. Kernel Density Estimation (Scott, 2015) was used for the visualization of the 2-dimensional normalized transmission and receiver score space (Fig. 1.5A).

We partitioned the normalized transmission-receiver space to five regions, and assigned each cell to one of these regions. Individual: transmission and receiver z-score < -0.5. Common: transmission z-score in the range of (-0.5, 0.5) and receiver z-score < 0.5 or receiver z-score in the range of (-0.5, 0.5) and transmission z-score < 0.5. Leader: transmission z-score > 0.5 and receiver z-score < 0.5. Follower: receiver z-score > 0.5 and transmission z-score < 0.5. Hub: transmission and receiver z-score > 0.5. The z-score threshold of 0.5 was selected to maintain sufficient number of cells in each role for statistical analysis.

Measuring information flow

GC edge probability was defined as the probability of a GC edge in the experiment. This was calculated as the ratio between the total number of GC edges and the total number of potential edges in the experiment (defined by topological distance ≤ 2 for each cell). Because GC edge probability is a proxy for the information flow within the multicellular network, we also used the term *information flow* to refer to the GC edge probability in the manuscript text.

Enrichment factor of cellular state transitions

We calculated the enrichment factor, the fold change in the observed transition probabilities of single cells from one state (functional role) to another cell state in consecutive cycles in relation to a null model derived from the expected transitions based on the marginal distribution of cells' functional roles.

First, we constructed the single cell transition matrix $tr_c^{c+1}(i,j,k)$ (Equation I), where the (i,j,k) bin holds the total number of transitions of the single cell $k \in K$ between state i and state j in consecutive cycles, $c, c+1 \in C$ observed throughout an experiment, and where S_c[k] indicates the state of cell k in cycle c.

I. $$tr_c^{c+1}(i,j,k) = \begin{cases} 1, & S_c[k] = i, S_{c+1}[k] = j \\ 0, & else \end{cases}$$

Second, we accumulated all transitions over all cells in the accumulated transition matrix $T(i,j)$ (Equation II).

II. $$T(i,j) = \sum_{k=1}^{|K|} \sum_{c}^{|C|-1} tr_c^{c+1}(i,j,k)$$

Third, we normalized each row of the accumulated matrix $T(i, j = 1, \ldots, |S|)$ to compute the Markov transition matrix $\hat{T}(i,j)$ (Equation III), the observed probability for a cell to transition from state i to state j throughout the experiment (Fig. S1.10 top-left).

III. $$\hat{T}(i,j) = \frac{T(i,j)}{\sum_{j=1}^{|S|} T(i,j)}$$

Finally, we calculated the enrichment factor matrix $\ddot{T}(i,j)$, the fold change in single cell transition from state i to state j in consecutive cycles in respect to the expected probability from a null model assuming random transitions drawn from the marginal state distribution $E(i,j)$ (Equation IV-VI, Fig. S1.10 bottom-left and right).

IV. $$f(i) = \frac{\sum_{k=1}^{|K|}\sum_{c=1}^{|C|} 1_{S_C[k]=i}}{\sum_{j=1}^{|S|}\sum_{k=1}^{|K|}\sum_{c=1}^{|C|} 1_{S_C[k]=j}}$$

V. $$E(i,j) = \frac{u \otimes_{\text{outer product}} u^T}{u}, \; u = [f(i=1), \ldots, f(i=|S|)]$$

VI. $$\ddot{T}(i,j) = \hat{T}(i,j) * \frac{1}{E(i,j)}$$

Measuring cell memory

To measure the cell memory we calculated the Pearson correlation of the cells transmission or receiver scores between consecutive cycles with step Δt (Δt = 1 in Fig. 1.4C, Δt ≥ 1 in Fig. S1.8B). We evaluated the significance of our results using a permutation test by shuffling the cells' spatial locations with over 1000 permutations. The permutation test was performed by concatenating the vector scores of the cycles c, c+Δt, shuffling the values, splitting back to two vectors, and calculating the absolute Pearson correlation. The p-value was set as the fraction of permutations where the shuffled correlation surpassed the observed experimental correlation. In this analysis, each stimulus cycle was considered as an independent event, although the cells' calcium dynamics ($\widehat{R_\iota}(t)$) never reached equilibrium between cycles because the shear stress was periodic and continuous. We performed an additional experiment with rest time between the applications of shear-stress periodic cycles. Even though the system did not synchronize well (in a single replicate), positive correlations were measured between cycles, specifically before and after the idle (i.e., pause in shear stress) cycle providing further evidence that the memory is a cell property that is independent across cycles (Fig. S1.14).

Activation Time

The activation time of a cell in a given cycle is the time where its calcium dynamics exceeds a threshold value of γ within a cycle. The threshold is parametrized by δ in the range of 0.1, 0.2 or 0.3 from the calcium dynamics range - the initial value subtracted from the maximal value within the cycle.

$$\gamma = \hat{R}_{C_i}(t = 0) + \delta * \left(\max\left(\hat{R}_{C_i}\right) - \hat{R}_{C_i}(t = 0)\right)$$

The initial time was shifted by 60 seconds (30 frames) from the onset of the cycle to the time where the mean value of the cells' calcium dynamics is zero to ensure that the single cell calcium signal is on the rise for the vast majority of the cells.

Correlating the topological distance between pairs of cells to their GC-edge probability

In Fig. 1.6B we correlated the topological distance to the corresponding GC edge probabilities. For each topological distance, for each cell, we randomly selected ten (or less in topological distances with smaller numbers) cells and calculated the GC statistical test for each cell pair in both directions. We evaluated the critical value (i.e., p-value correction) using FDR, to correct for multiple hypothesis testing. Finally, we calculated the probability for GC significant edge as the total number of significant edges divided by total GC tests performed.

Data

N = 47 biological replicates for the "step" experiments: n = 6 (0.1 Pa), n = 13 (0.2 Pa), n = 8 (0.6 Pa), n = 10 (1 Pa), n = 10 (1.6 Pa). N = 14 biological replicates for the "cycles" experiments: control n = 4 (0.1 Pa) and n = 6 (0.2 Pa), low density n = 2 (0.2 Pa), gap-junction inhibition n = 2 (0.2 Pa).

Supplemental Figures

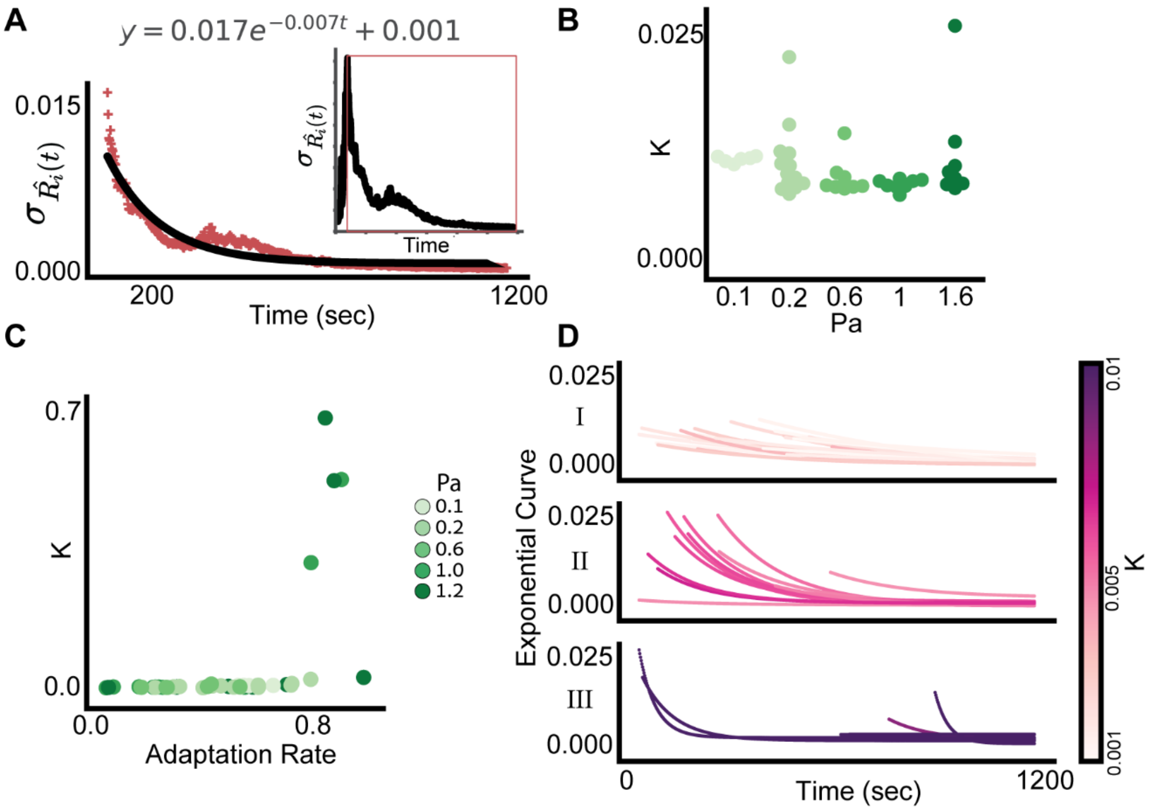

Figure S1.1: Parametric exponential model for multicellular calcium adaption.
(**A**) Fitting an exponential model A*e^-Kt + c (black) to experimental multicellular calcium dynamics (red '+' markers). Inset: calcium dynamics throughout the full experiment, the exponential fit considered the temporal range from the maximal signal until the end of the experiment (orange rectangle, Methods).
(**B**) The exponential model coefficient K for each pressure level. Each data point reports the K coefficient of the model fit for a single experiment. 4/47 experiments with K > 0.1 were excluded for visualization purposes.
(**C**) Correlation between the adaptation rate and K. N = 47 experiments pooled across all shear stress levels, Pearson correlation = 0.5160, p-value = 0.0002. Pearson correlation = 0.7140, p-value ≤ 0.0001 when excluding the 4 outlier experiments where the data did not fit the exponential model (K > 0.1).
(**D**) Exponential curves fitted for the N = 46 experiments across all shear stress levels. Color code (linear) encodes the K coefficient of the corresponding exponential fit. The curves were partitioned to 3 sub-panels for visualization purposes: (I) K < 0.004, (II) 0.004 ≤ K < 0.008 (III) K ≥ 0.008. One experiment was filtered (because the coefficient A was < 0).

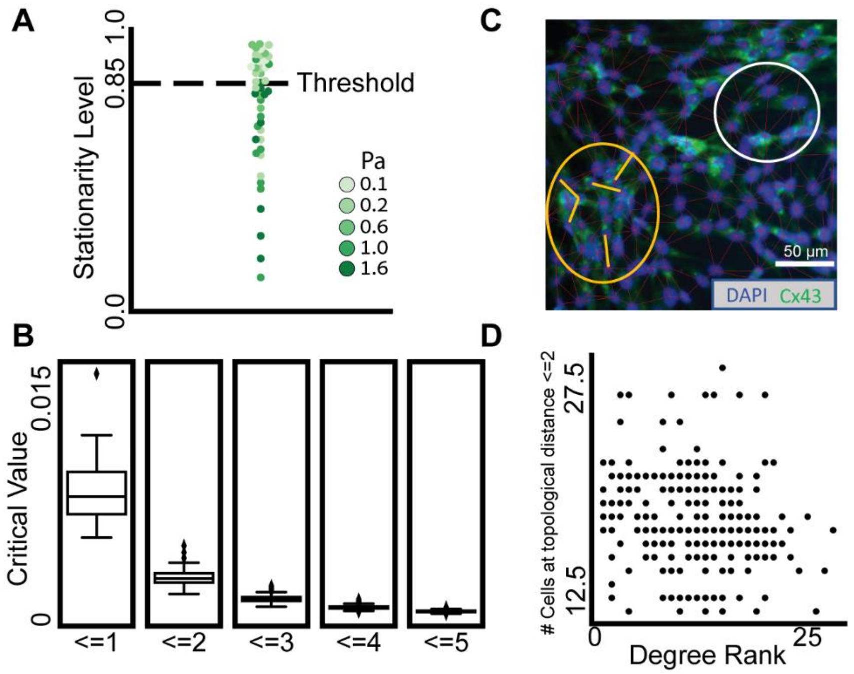

Figure S1.2: Stationarity and using topological distances of up to two in calculating the transmission and receiver score.

(A) Fraction of cells passing stationarity test per experiment. Each observation represents a biological replica. N = 47 biological replicates: n = 6 (0.1 Pa), n = 13 (0.2 Pa), n = 8 (0.6 Pa), n = 10 (1 Pa), n = 10 (1.6 Pa). In 23/47 experiments at least 85% of the cells passed both the KPSS and the ADF stationary tests with statistical significance levels below 0.05 (see Methods).

(B) Topological distance of two is a sweet spot in terms of reducing the false-positive errors (representative of ten experiments). Critical value range after Bonferroni correction for each topological distance upper bound (see Methods for details).

(C) Topological distance of two to reduce the effect of irregular shapes of the cells. Typical immunofluorescent image with dual labeling of cell nucleus (DAPI, blue) and gap junction proteins (Cx43, green). The thin red lines connect nuclei of nearest neighbor cells (defined with Delaunay Triangulation). In the low density region (e.g., white circle), gap junctions only appear between nearest neighbors. In the high density region (e.g., orange circle), gap junctions also connect cells that are nextto-nearest neighbors (see example pairs indicated by orange lines). Our shear-stress experiments were mostly high cell density, with confluence greater than 85%. Our shear-stress experiments were mostly high cell density, with confluence greater than 85%.

(D) The number of neighbors at topological distance ≤ 2 have weak correlation with the degree rank (accumulation of in-degree and out-degree edges). N = 295 cells from one experiment (representative of ten experiments). Pearson coefficient = -0.1678, p-value =0.0039.

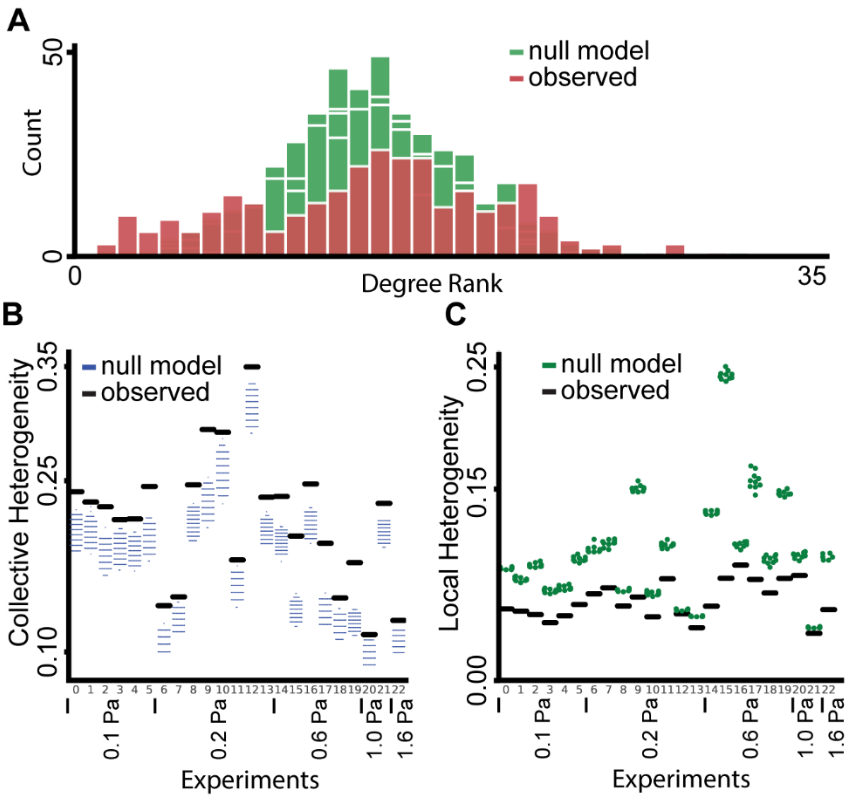

Figure S1.3: The multicellular network was characterized by collective heterogeneity and local homogeneity in its degree ranks.

(**A**) The degree rank distribution of n = 10 null model simulations (green, see Methods) and the observed network (red). The mean collective heterogeneity score as measured with (Jacob et al., 2017) (~0.29) is higher than the mean heterogeneity in the null models that considered random shuffling of GC edges while preserving the probability for an edge (~ 0.25, Methods). Representative of ten experiments.

(**B**) Collective heterogeneity across experiments. Observed collective heterogeneity (black) was higher than the null model (blue). N = 23 biological replicates, across shear stress levels, that passed the stationarity criterion.

(**C**) Local heterogeneity (Estrada's index (Estrada, 2010)) across experiments. Observed local heterogeneity (black) was lower (more homogeneous) than the null model (green) that rewired the edges while preserving the degree distribution of the original network. N = 23 biological replicates, across shear stress levels, that passed the stationarity criterion.

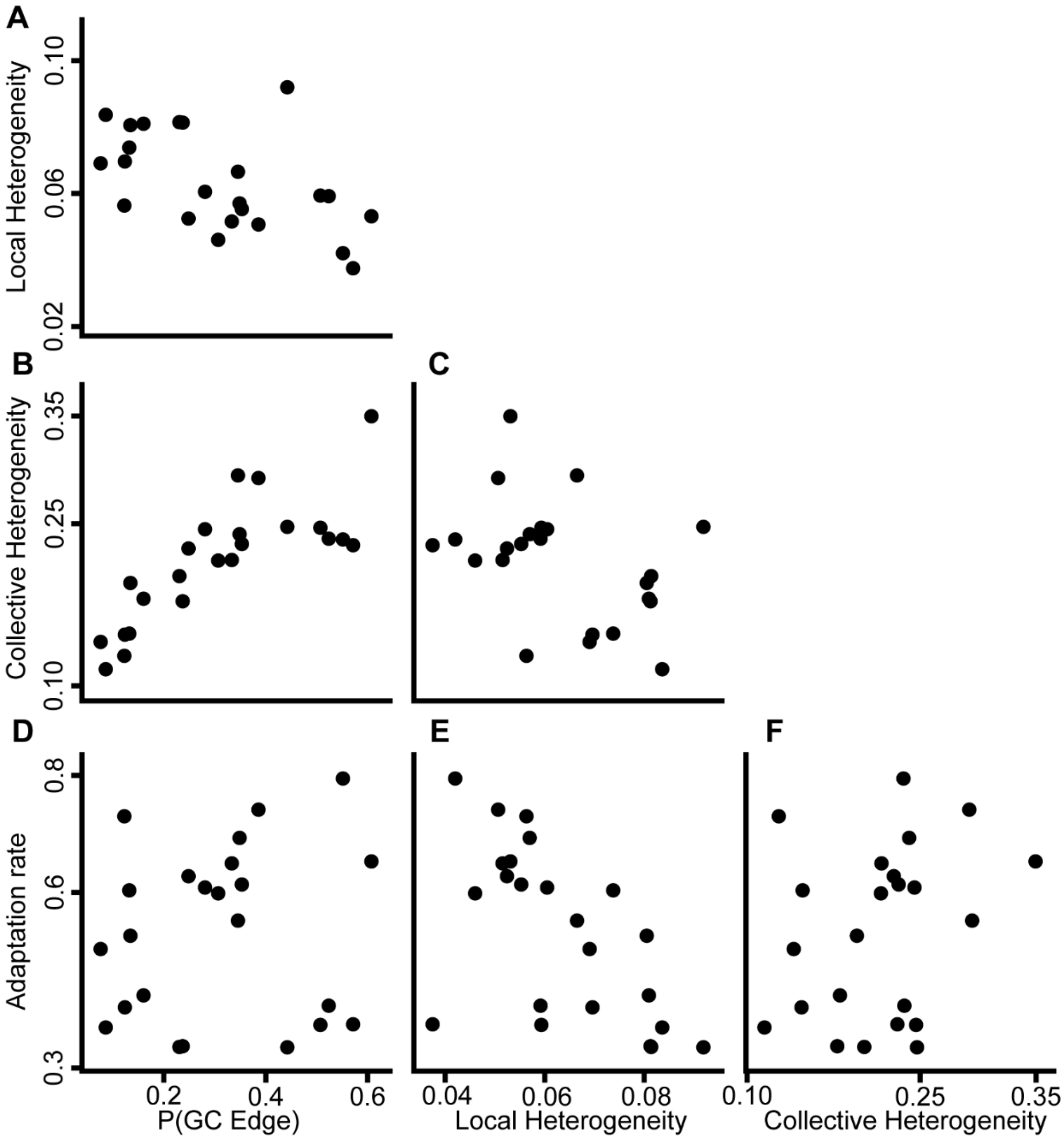

Figure S1.4: Correlating four measurements across experiments: multicellular adaptation, information flow, collective and local heterogeneity. N = 23 biological replicates, across shear stress levels, that passed the stationarity criterion were considered to calculate correlations.
(**A**) Local heterogeneity versus P(GC Edge). Pearson correlation = 0.55, p-value = 0.006.
(**B**) Collective heterogeneity versus P(GC edge). Pearson correlation = 0.80, p-value =0.000.
(**C**) Adaptation rate versus P(GC edge). Pearson correlation = 0.11, p-value = 0.615.
(**D**) Collective heterogeneity versus local heterogeneity. Pearson correlation = -0.41, p-value = 0.052.
(**E**) Adaptation rate versus local heterogeneity. Pearson correlation = -0.61, p-value = 0.002.
(**F**) Adaptation rate versus collective heterogeneity. Pearson correlation = 0.28, p-value =0.200.
Collective heterogeneity was correlated with the GC edge probability while the local heterogeneity was negatively associated with the adaptation rate as well as with the GC edge probability (and statistically marginally with the collective degree heterogeneity). The remaining measurement pair correlations were not statistically significant, but showed consistency in the correlation sign associating adaptation rate, GC edge probability, collective heterogeneity, and local homogeneity. One reason for the lack of statistical power could be the variability between experiments, including the varying shear stress

magnitudes.

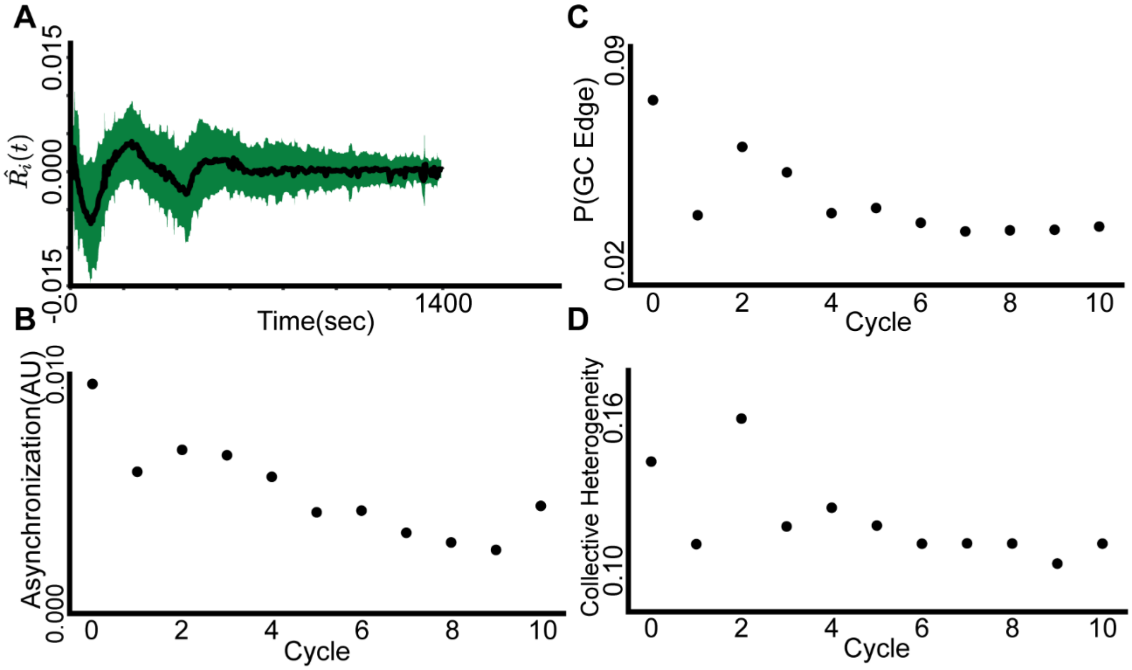

Figure S1.5: Sufficient cell density is required for multicellular synchronization. Shown are results for an experiment with sparse cell seeding. Representative of two experiments.

(**A**) Multicellular calcium dynamics over time in response to external mechanical stimuli. The calcium dynamics of each cell was represented by the time-derivative of its relative fluorescent intensity. Black: mean calcium *Ri*(*t*) dynamics; Green: standard deviation.

(**B**) Multicellular calcium dynamics synchronized over time for sparsely seeded cells. Pearson correlation = -0.8563, p-value = 0.0007. However, synchronization was less effective than in our baseline density experiments (compare to Fig. 1.3B and full results in Table S2).

(**C**) Information flow did not increase over time for sparsely seeded cells. Pearson correlation = -0.7581, p-value = 0.0068.

(**D**) Collective heterogeneity did not increase over time for sparsely seeded cells. Pearson correlation = -0.6517, p-value = 0.0298.

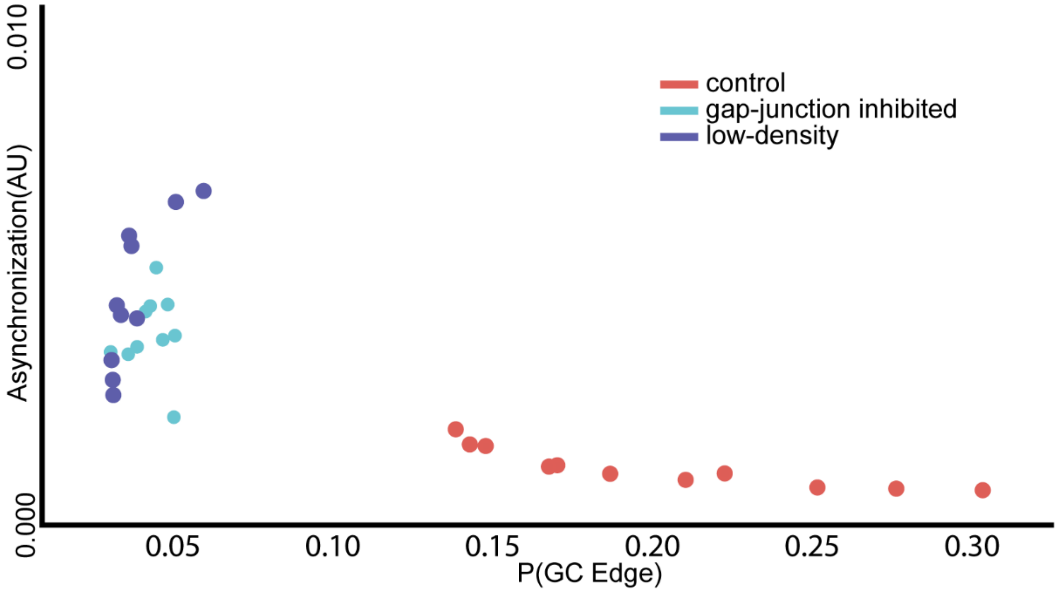

Figure S1.6: Asynchronization and GC edge probability. Control, representative of 10 experiments (red): asynchronization was negatively associated with GC edge probability (Pearson correlation = -0.8933, p-value ≤ 0.000091). Gap-junction inhibition, representative of two experiments (cyan): asynchronization is not associated with GC edge probability (Pearson correlation = 0.0077, p-value = 0.9829). Low density, representative of two experiments (purple): asynchronization is positively associated (i.e., cells are not synchronizing over time) with GC edge probability (Pearson correlation = 0.8151, p-value = 0.0040). This analysis considered 12 (control), 10 (gap-junction inhibition), 10 (low density) cycles. The first cycle was an outlier and was excluded from this analysis.

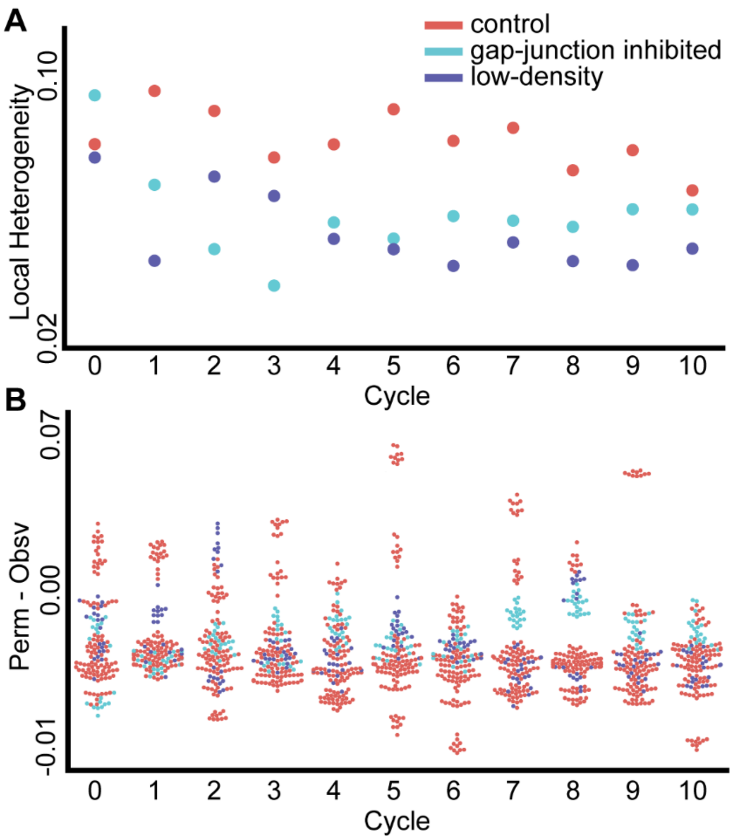

Figure S1.7: Local heterogeneity over time

(**A**) Control experiment, representative of ten experiments (red) (Pearson correlation = -0.6127, p-value = 0.0450), gap junction inhibition experiment, representative of two experiments (Pearson correlation = -0.2973, p-value = 0.3744) (cyan) and low density experiment, representative of two experiments (purple) (Pearson correlation = -0.6688, p-value = 0.0244).

(**B**) Each point represents the difference between a single permutation of the null model that spatially shuffles the cells' neighbors while preserving the same degree rank and the observed experiment for local heterogeneity (see Methods) over all the cycle experiments replication. Control experiments (red, n=10). Gap junction inhibition experiments (cyan, n=2). Low density experiments (purple, n=2). There is no clear separation between the control, gap-junction inhibited, and low-density experiments.

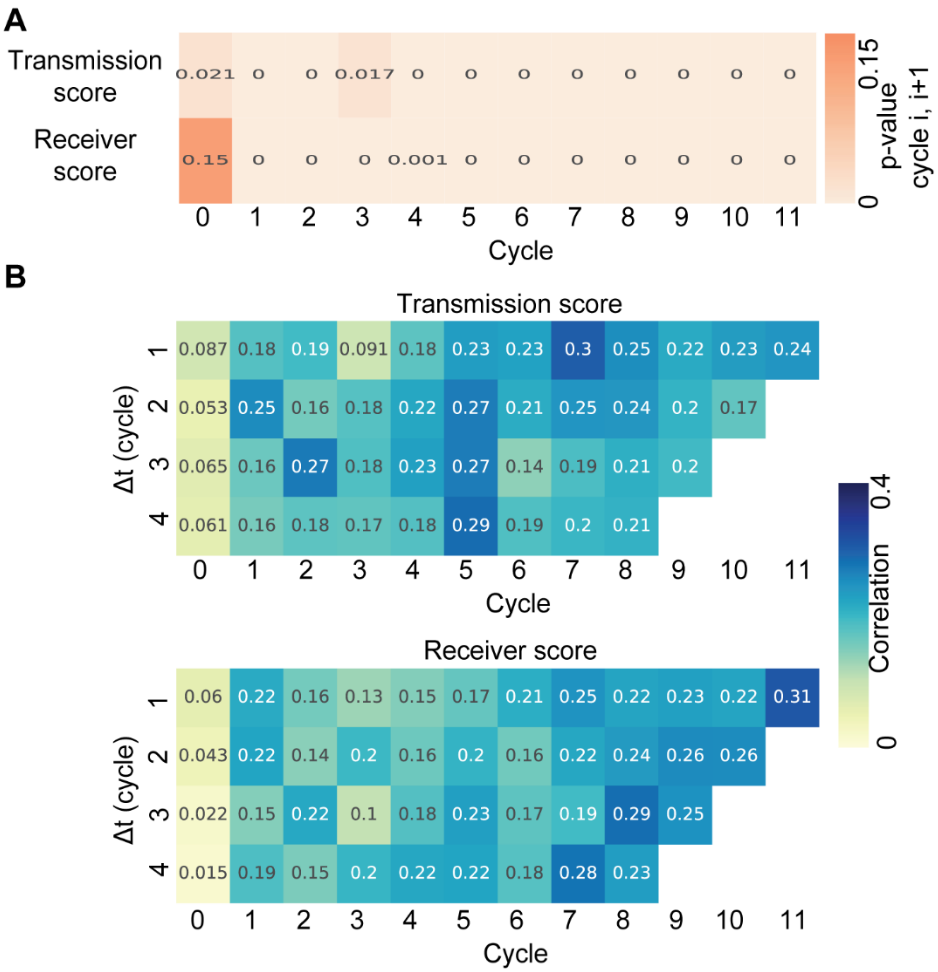

Figure S1.8: Single cell communication memory. Representative of ten control experiments.
(**A**) P-value of the correlation between the cells' transmission/receiver scores over consecutive cycles (x-axis), values correspond to the correlations in Fig 1.4A. The color scale is linear.
(**B**) Longer term memory. The temporal correlations between single cells' transmission (top) or receiver (bottom) scores with time gaps of 1-4 cycles (y-axis). The x-axis indicate time (cycle #) and the y-axis indicates the number of cycles considered when calculating the correlation. The color scale is linear.

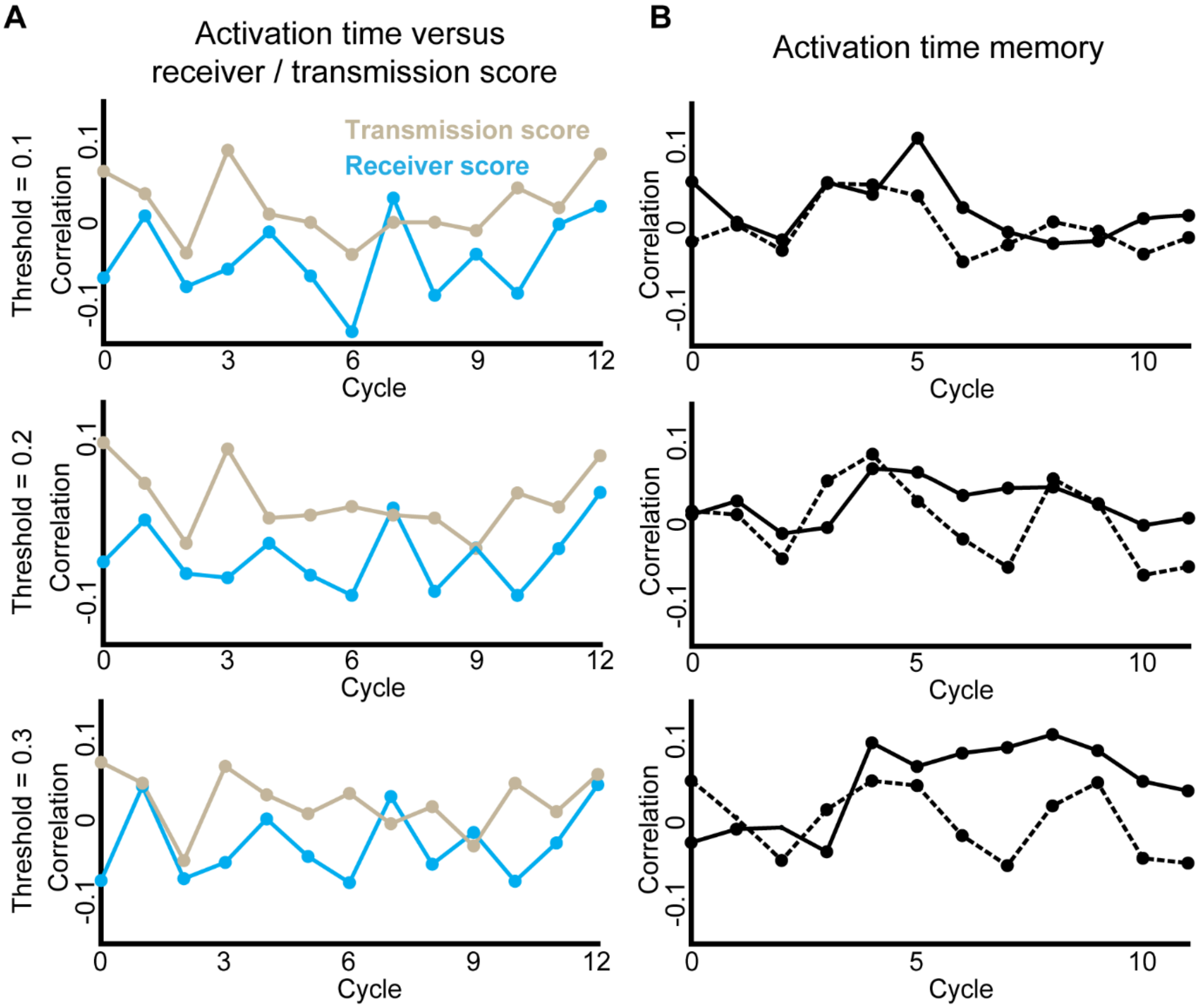

Figure S1.9: Single cell activation time. Representative of ten control experiments. A cell's activation time was defined as the time where the cell's calcium dynamics exceed δ= 0.1-0.3 (top-to-bottom) from it's maximal signal, see Methods for full details.

(A) Cells' activation time was not correlated with the transmission or the receiver score.

(B) Cells' activation time was not correlated across consecutive cycles (solid lines). The dashed lines were the calculated correlation after shuffling the cells in the next cycle.

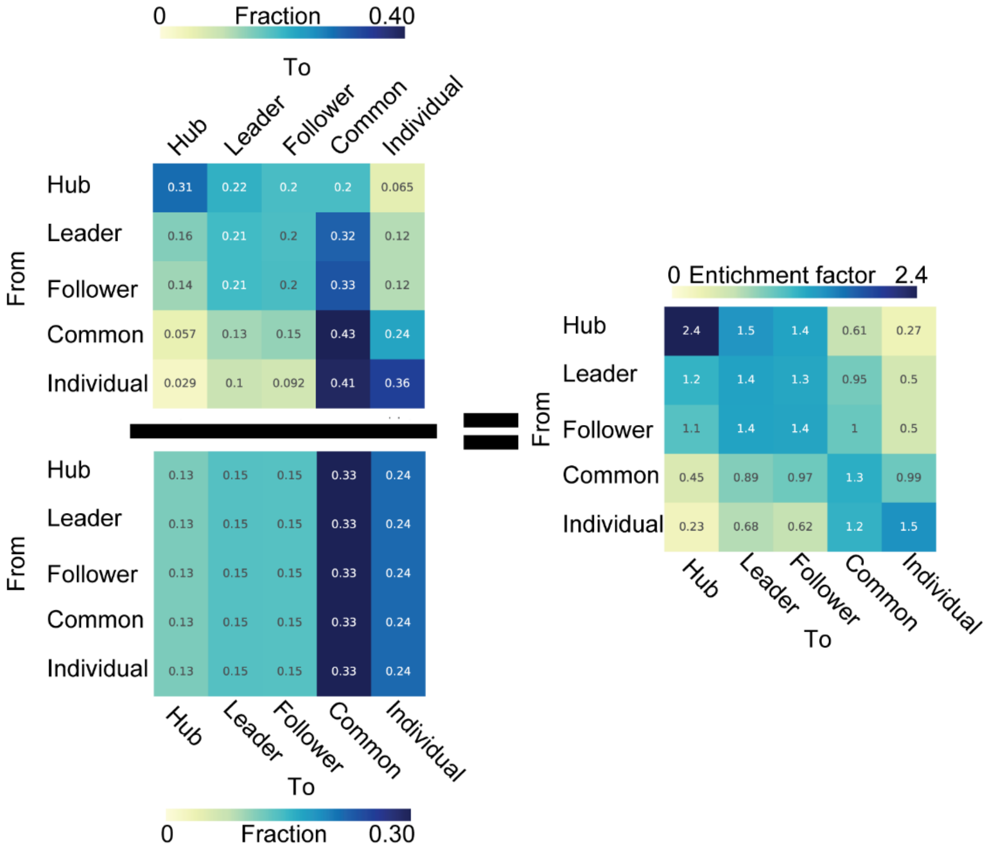

From \ To	Hub	Leader	Follower	Common	Individual
Hub	0.31	0.22	0.2	0.2	0.065
Leader	0.16	0.21	0.2	0.32	0.12
Follower	0.14	0.21	0.2	0.33	0.12
Common	0.057	0.13	0.15	0.43	0.24
Individual	0.029	0.1	0.092	0.41	0.36

From \ To	Hub	Leader	Follower	Common	Individual
Hub	0.13	0.15	0.15	0.33	0.24
Leader	0.13	0.15	0.15	0.33	0.24
Follower	0.13	0.15	0.15	0.33	0.24
Common	0.13	0.15	0.15	0.33	0.24
Individual	0.13	0.15	0.15	0.33	0.24

From \ To	Hub	Leader	Follower	Common	Individual
Hub	2.4	1.5	1.4	0.61	0.27
Leader	1.2	1.4	1.3	0.95	0.5
Follower	1.1	1.4	1.4	1	0.5
Common	0.45	0.89	0.97	1.3	0.99
Individual	0.23	0.68	0.62	1.2	1.5

Figure S1.10: Calculating the enrichment factor of cellular state transitions. Representative of ten control experiments. Top left: Markov transition matrix based on the observed single cell role transition over the cycles. Bottom left: The expected transition probability between two roles based on the cells' roles frequency over the cycles. Right: The enrichment transition matrix was followed by normalizing (scalar division) the Markov transition matrix with the expected transition matrix. The enrichment factor from hub to hub is higher than any other enrichment factor. (see only transitions above the expected, Fig. 1.5D).

The color scale is linear.

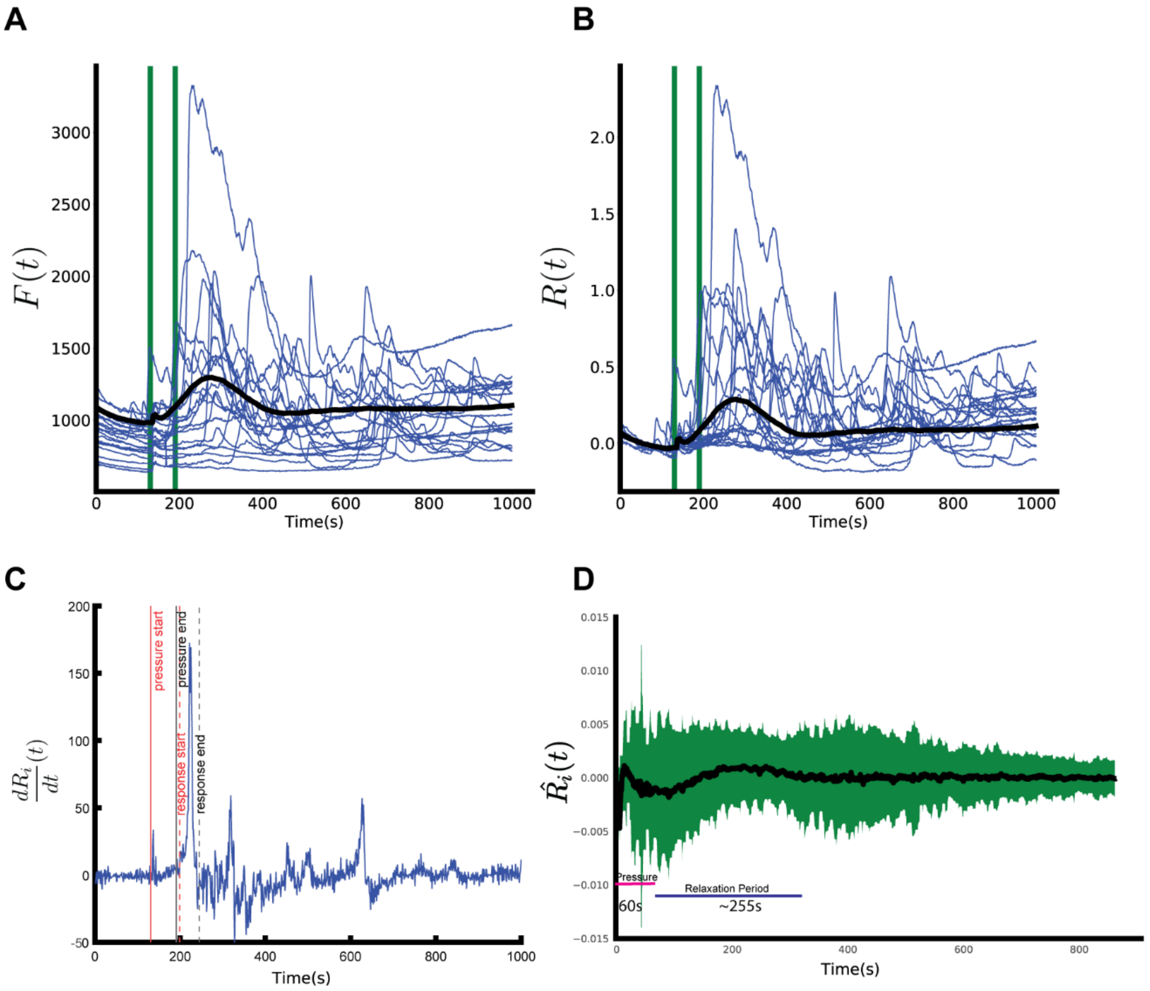

Figure S1.11: Analysis of stimulation onset and relaxation time after a single pulse of shear stress. Representative of two experiments. To assess single cell relaxation time we performed a new experiment (2 replicates) where, after 130 seconds without stimulation, we applied a pulse of shear stress (0.2 Pa) for 60 seconds and then released the stress and followed the relaxation.

(**A-B**) The raw (A) and normalized (B) calcium intensity time-profile of 20 randomly selected responding cells. For each cell, the calcium peak near the time to the pulse of shear stress application and the time where the cell settled (or "relaxed") were manually annotated. Black: mean intensity. Green vertical line marks the time of the stimuli onset and stop. Single cells reached a steady state ~70-110 seconds after their peak (mean 72.25 seconds, standard deviation 25.3 seconds) and full collective relaxation was achieved after approximately 285 seconds. The fluorescent intensity usually did not return to the prestimuli level, but the cells settled to a new basal level that is slightly higher than the original, and do not show changes in the intensity beyond short noise fluctuations (in fact, this is one of our reasons to analyze the temporal derivatives).

(C) Derivative of the normalized calcium intensity of a representative cell. The red solid line indicates the beginning of the pulse and the red dashed line the end of the pulse. The black solid line indicates the start of the manually annotated cell's response and black dashed line the cell's relaxation time.

(D) Multicellular calcium dynamics (black - mean calcium dynamics, green - standard deviation). The 60s of shear stress application is marked in red and the relaxation time is marked in blue.

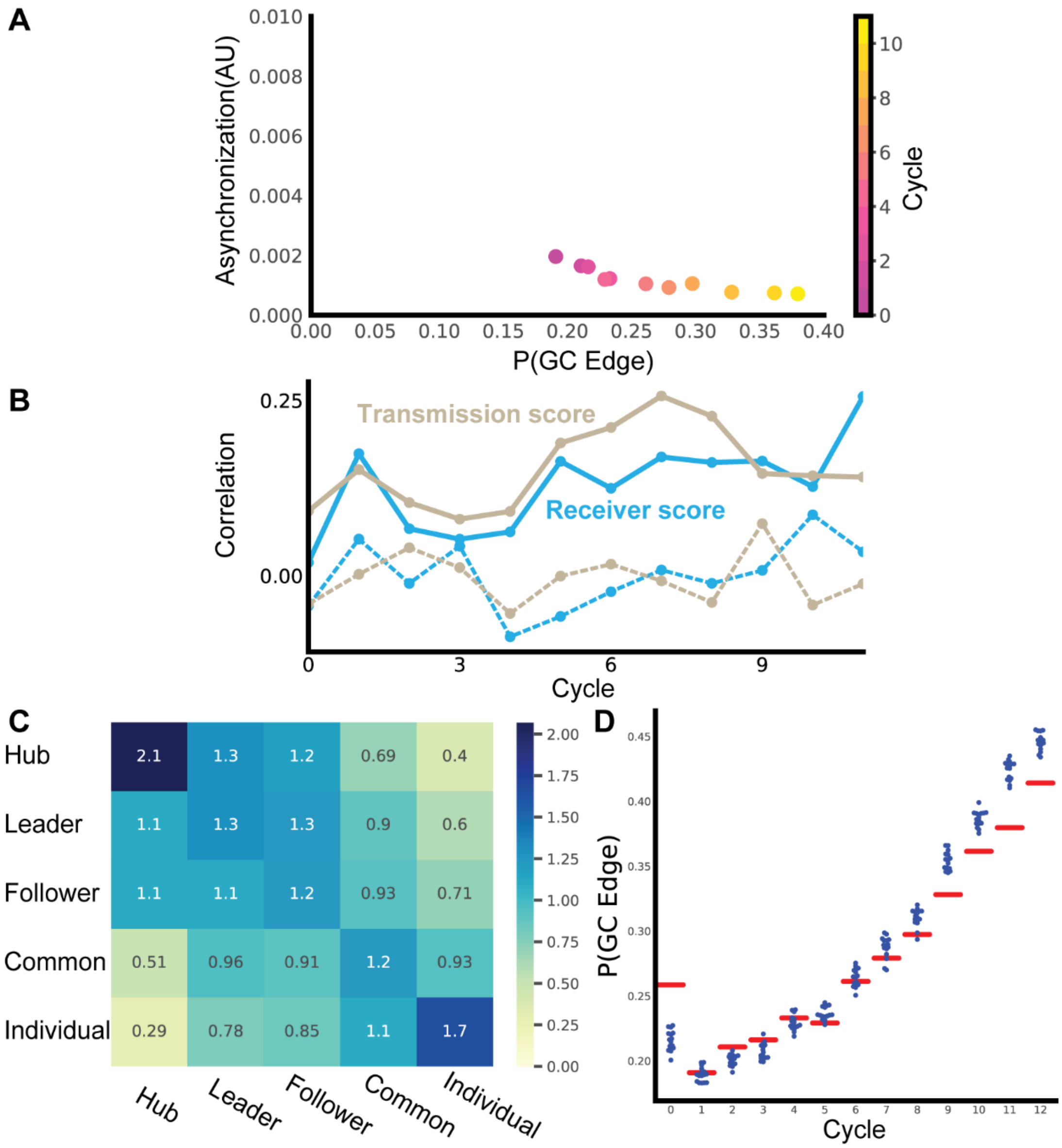

Figure S1.12: Replication of main results with topological distance of one. Representative of ten control experiments.

(A) Asynchronization was negatively associated with GC edge probability (Pearson correlation = -0.8972, p-value = 0.0002). The first cycle was an outlier and was excluded from this analysis. The color scale is linear.

(B) Cells transmission and receiver scores were correlated across consecutive cycles (solid lines), reinforced over time (Pearson coefficient = 0.5620, $p < 0.0044$), and were a local cell property as validated with permutation analysis – shuffling the cells in the next cycle and calculating correlation (dashed line, see Methods).

(C) The enrichment transition matrix**.** The enrichment factor from hub to hub is higher than any other enrichment factor. The color scale is linear.

(D) Gradual local to global transition in information spreading. The observed versus permuted Granger causality edge probability, P(GC edge), over the cycles. The red horizontal line is the experimental observation, while each blue dot is the result of one of ten independent spatial cell permutations.

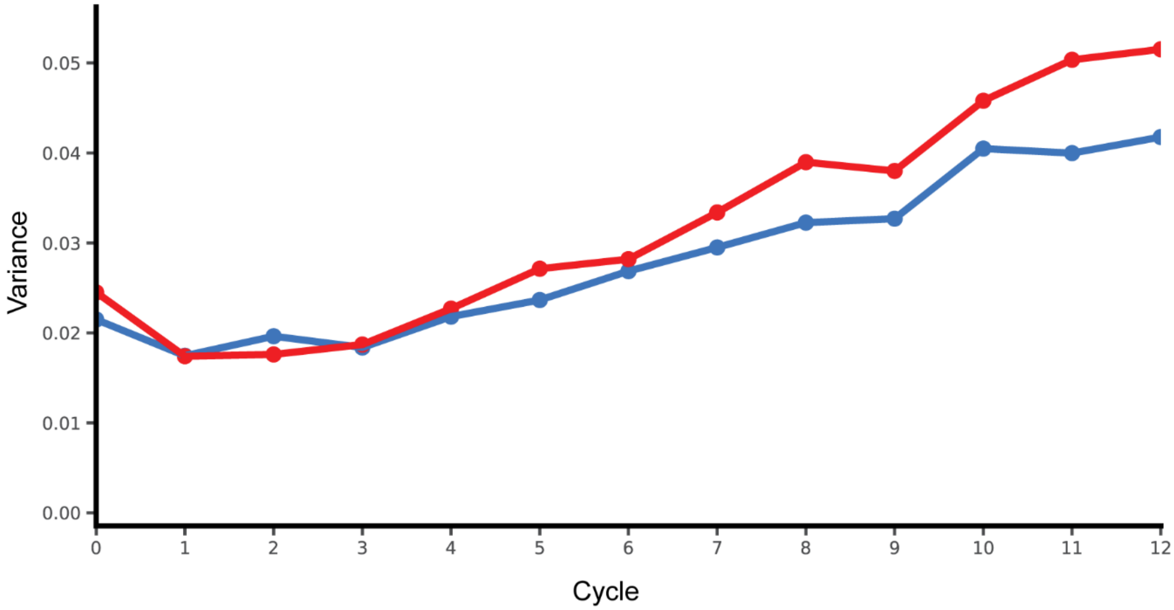

Figure S1.13: Variance in the cells' raw (i.e., before normalization) transmission (red) and receiver (blue) scores for each cycle. Representative of ten control experiments. The variance is increased over time in the transmission score (Pearson coefficient = 0.9541, $p < 0.0001$) and in the receiver score (Pearson coefficient = 0.9442, $p < 0.0001$).

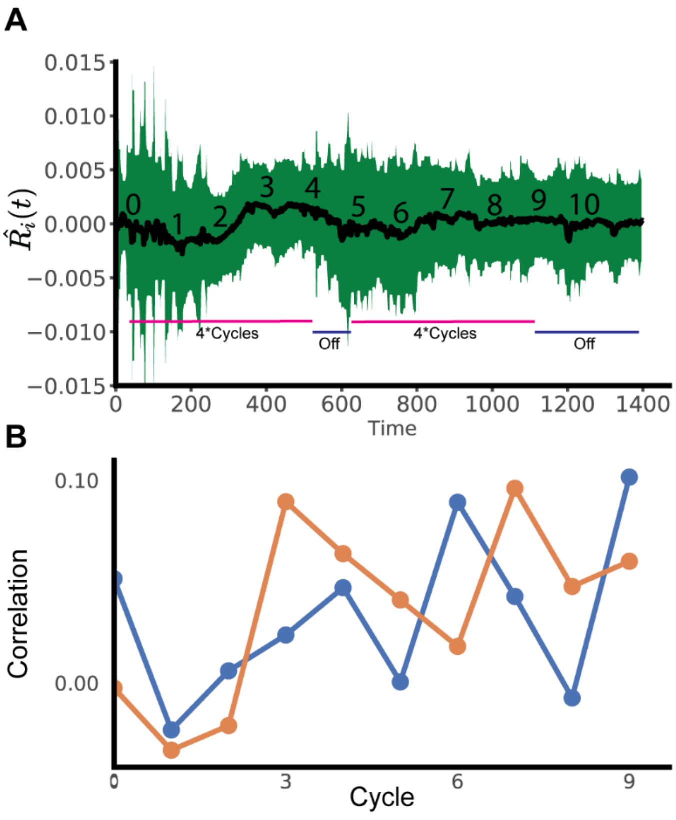

Figure S1.14: Cycle experiment were the shear stress was turned off for one cycle (cycle #4) showed weak memory.

(A) Multicellular calcium dynamic. Black indicates the mean calcium dynamics, and green the standard deviation. Numbers indicate periodic shear stress cycles, horizontal pink lines mark rounds of 4 consecutive cycles, and horizontal blue lines marks times were the shear stress was turned off.
(**B**) Cells transmission and receiver scores were marginally but positively correlated across consecutive cycles (solid lines), and slightly increased over time (Pearson coefficient = 0.6092, $p < 0.0616$). Shown are correlations with time delay of two cycles. This specifically included the positive correlation at cycle #3 (x-axis, between cycle 3 and 5) that involved the “idle” (i.e., no shear stress application) cycle.

Supplemental video and .csv table titles and legends

Video S1.1: A video of a representative "step" experiment with shear stress of 0.2 Pa. https://www.cell.com/cms/10.1016/j.cels.2022.07.002/attachment/05d1eca9-ea50-4209-ba0d-f540d31a00c3/mmc5.mp4

Video S1.2: A video of a cyclic experiment of shear stress of 0.2 Pa. https://www.cell.com/cell-systems/fulltext/S2405-4712(22)00292-7#mmc6

Video S1.3: A video depicting the transmission score of a representative "cycles" experiment with shear stress of 0.2 Pa. Each region represents a single cell. https://www.cell.com/cms/10.1016/j.cels.2022.07.002/attachment/ce55c74e-cc92-4de9-8605-781a53f1d87e/mmc7.mp4

Video S1.4: A video depicting the receiver score of a representative "cycles" experiment with shear stress of 0.2 Pa. Each region represents a single cell. https://www.cell.com/cms/10.1016/j.cels.2022.07.002/attachment/276b3958-6893-4782-a9c8-08ea96c575e2/mmc8.mp4

Video S1.5: A video depicting the evolution of the transmission and receiver scores of a representative "cycles" experiment with shear stress of 0.2 Pa. Showing is the kernel density estimate plot visualization of the normalized transmission and receiver score over the cycles. Partitioning of the z-score normalized transmission-receiver space to five regions (blue dashed lines), each cell (yellow dot) was assigned to a state or role (red text) according to the region they resided at. https://www.cell.com/cms/10.1016/j.cels.2022.07.002/attachment/1faabb37-5635-4272-9d6d-470d6f6409c3/mmc9.mp4

Video S1.6: A video depicting the single cell evolution in communication properties of a representative "cycles" experiment. Each region represents a single cell and the communication roles are color coded. https://www.cell.com/cms/10.1016/j.cels.2022.07.002/attachment/e4b52b8f-5ce1-46e6-8c7d-a056d4abc88a/mmc10.mp4

Chapter 2: Context-dependent spatial multicellular network motifs for single-cell spatial biology

Amos Zamir[1], Yael Amitay[2], Yuval Tamir[1], Leeat Keren[2], Assaf Zaritsky[1]

[1]Department of Software and Information Systems Engineering, Ben-Gurion University of the Negev, Beer-Sheva, Israel

[2]Department of Molecular Cell Biology, Weizmann Institute of Science

*Correspondence: assafzar@gmail.com

Summary

The clinical state of diseased tissue is caused by complex intercellular processes that go beyond pairwise cell-cell interactions and are difficult to infer due to the combinatorial explosion of such high-dimensionality. We present context-dependent identification of spatial motifs (CISM), a two-step method to identify local interconnected cell structures associated with a disease state in single cell spatial proteomics data. First, for each tissue, CISM enumerates structures of enriched reoccurring multicellular patterns that define the modular components ‘motifs’ in the multicellular network. Second, discriminative motifs are selected according to the context - their presence in patients at different clinical disease states. By applying CISM, we show that modular structures composed of as little as 3-5 cells and their relative spatial organization can encode differences in clinical disease states in cohorts of triple-negative breast cancer (TNBC) and melanoma patients. Machine learning validation indicated that discriminative motifs outperform state-of-the-art methods for disease state prediction while enabling interpretation of which interactions in what spatial context are associated with these predictions. CISM-derived discriminative motifs may define a higher layer of abstraction and modularity in multicellular organization and function with broad applicability in the domain of spatial single cell omics and beyond.

Introduction

The architecture and functional state of a healthy tissue relies on individual cells using their basic cellular machinery to influence and respond to neighboring cells through a complex interplay of chemical and physical cues. Dysfunctional regulation of molecular and cellular processes underlies the defected tissue organization and function in disease. How local interactions between single cells are integrated in space to contribute to function or loss of function at the tissue scale is yet to be resolved. Traditional tissue-scale bulk readouts cannot explain tissue scale cell organization because population averages mask the single cell types and cell states heterogeneity. Single cell 'omics' techniques overcome these limitations can not resolve the information regarding the tissue's spatial organization. Recent spatial single cell 'omics' techniques enable to determine for every cell its cell type and state and to map it back to its physiological tissue context in situ (Marx, 2021). These advances bring on the next technical challenges of systematically representing and bridging the different spatial scales of tissue organization from individual cells to physiological meaningful tissue state.

Most analysis efforts are currently focused on measuring cell type proportions, pairwise interactions between cell types (Ali et al., 2024; Dayao et al., 2023a; Keren et al., 2018; Risom et al., 2022; Samorodnitsky et al., 2024; Seal et al., 2024) cellular microenvironments (Dayao et al., 2023b; Jackson et al., 2020; Tamir et al., 2024; Wu et al., 2022; Wu & Zou, 2022) and graph modeling approaches (Ali et al., 2024; Jackson et al., 2020; Tamir et al., 2024; Wu et al., 2022; Wu & Zou, 2022). We hypothesize the existence of an intermediate spatial scale of tissue organization involving a few locally interacting cells that define modular components of different clinical states of diseased tissues. Such modular components can define a new layer of abstraction that can help reveal biologically meaningful higher-order intercellular interactions that are associated with tissue state, thus bridging the gap between pairwise interactions and tissue organization. However, the number of potential high-dimensional intercellular interactions grows exponentially as a function of the number of cells involved in these interactions, and thus are difficult to explicitly infer systematically.

Here, we adapt and extend the concept of "network motifs", reoccurring sub-networks that define "building blocks" of complex networks (Milo et al., 2002), to characterize the fine-scale organization of multicellular spatial networks of human disease tissues. Seminal studies starting at the beginning of the millennium established motifs in transcription networks of multiple experimental systems and organisms, suggestive of their role as modular and universal building blocks of transcription networks that are repeatedly selected by evolution for their biological function (Alon, 2007). Motifs also appeared in other biological and non-biological networks (Milo et al., 2004). We introduce a new method named Context-dependent Identification of Spatial Motifs (CISM) that identifies "discriminative" motifs in the spatial network that are associated with human disease states. Applied to investigate future metastasis in melanoma and short- versus long-term patient survival in triple-negative breast cancer, we demonstrated that CISM discriminative motifs of 3-5 cells represent a signature for tissue disease state. These discriminative motifs were used as features for accurate machine learning prediction, and their localization in the tissue revealed the spatial contexts for which motifs were associated with the disease state. We also revealed that the specific relative spatial organization of cells within the motif contributes to the disease discrimination beyond the motifs' cell type composition and demonstrated how the same patient-derived motifs can be differentially analyzed under varying disease contexts. Specifically, in (metastatic-free) sentinel lymph nodes of stage II melanoma patients, CISM identified discriminative motifs consisting of B cells and CD8 T cells that appear in the layer of B cells surrounding the germinal centers of tumor-free lymph nodes that progressed in five years to remote metastases. In TNBC patients, CISM identified discriminative motifs consisting of interactions between tumor cells and CD8 T cells or CD4 T cells that were associated with long-term survival. CISM-derived discriminative motifs may define a new layer of abstraction and modularity in a multicellular function with broad applicability in the domain of spatial single cell and beyond.

Results

Context-dependent Identification of Spatial Motifs (CISM)

We introduce context-dependent identification of spatial motifs (CISM) as a bottom-up method for grouping cells into fine-grained spatially resolved multicellular functional modules that provide meaningful information regarding physiological tissue states (Fig. 2.1). Following single cell segmentation and cell type classification (Fig. 2.1A), we define a *spatial multicellular network* representing the spatial organization of a tissue, where the nodes of the network are single cells with an edge between every pair of adjacent cells according to the Delaunay triangulation (Fig. 2.1B, left). This process creates a "colored" graph, where each node is colored according to its corresponding cell type. Network motifs are defined as sub-graphs (i.e., a set of cells and edges) that occur more than expected in the graph, where "more than expected" is determined according to a statistical significance test. Intuitively, a subgraph is considered a motif if its frequency in the observed graph precedes its frequency in random graphs generated by edge-switching that preserves the degree distribution (Methods). Existing methods for motif identification in "colored" graphs are bounded in the number of colors as a function of the motifs' size. This is a substantial limitation for single cell multiplexed data that is characterized by multiple cell types. Thus, we adjusted an existing implementation of a method called FANMOD (Wernicke & Rasche, 2006) to define FANMOD+ (see Methods). Our implementations can support up to 128-colored networks, going well beyond existing motif detection tools that support at most 15 colors for motifs at size 4-6, 3 colors for motifs of size 7 and 0 colors for motifs of size 8 (Smoly et al., 2017). Given a motif size *n* (i.e., number of cells), for each patient's tissue sample, CISM extracts and enumerates thousands of motifs and calculates for each motif its frequency with respect to the total number of corresponding subgraphs of size *n* in the patient's sample (Fig. 2.1B, right). To identify motifs that are associated with a clinical outcome, CISM selects the motifs that appear in at least a predetermined fraction of the patients with the corresponding clinical outcome and that do not appear in any patients with other clinical outcomes; we term these as *context-dependent discriminative motifs*. These discriminative motifs can provide concrete discriminative and biologically-meaningful interpretable information, at the spatial scale of a few cells, and of their potential local interactions. Notably, the same motifs, with different context-dependent inclusion criteria, can be used to tackle different questions. Altogether, the motifs are generated in an unsupervised fashion, and then selected, with supervision, according to the context-dependent discrimination criteria, such as disease state or clinical treatment.

CISM context-dependent discriminative motifs can be used to formulate a machine learning-based prediction of the tissue's disease state. Each patient is represented by the (sparse) vector of its discriminative motifs frequencies. Since patient cohorts are commonly limited to tens of patients, we evaluated the models in leave-one-patient-out cross validation: multiple rounds of training and testing, each round with one patient designated for a test, and all other patients are used as the training set. More specifically, each iteration followed the processes depicted in Fig. 2.1C (left-to-right): (1) keep one patient out, (2) extract discriminative motifs from all patients excluding the one that was left out, (3) use the most frequent discriminative motifs as representations to train a machine learning model to predict the tissue disease state, (4) apply the model on the kept out patient. Importantly, in this setting, the training process is fully independent of the patient at the test (Jones, 2019). This process was repeated for all patients, and the different models' prediction probabilities of each patient left out were pooled and evaluated with the area under the receiver operating characteristic curve (AUC-ROC). Discriminative motifs can be evaluated based on their prevalence across patients to infer motifs-induced pairwise interactions disease signatures and/or based on their contribution to the models' performance and can be mapped back to their spatial context within the tissue for biological interpretation (Fig. 2.1D).

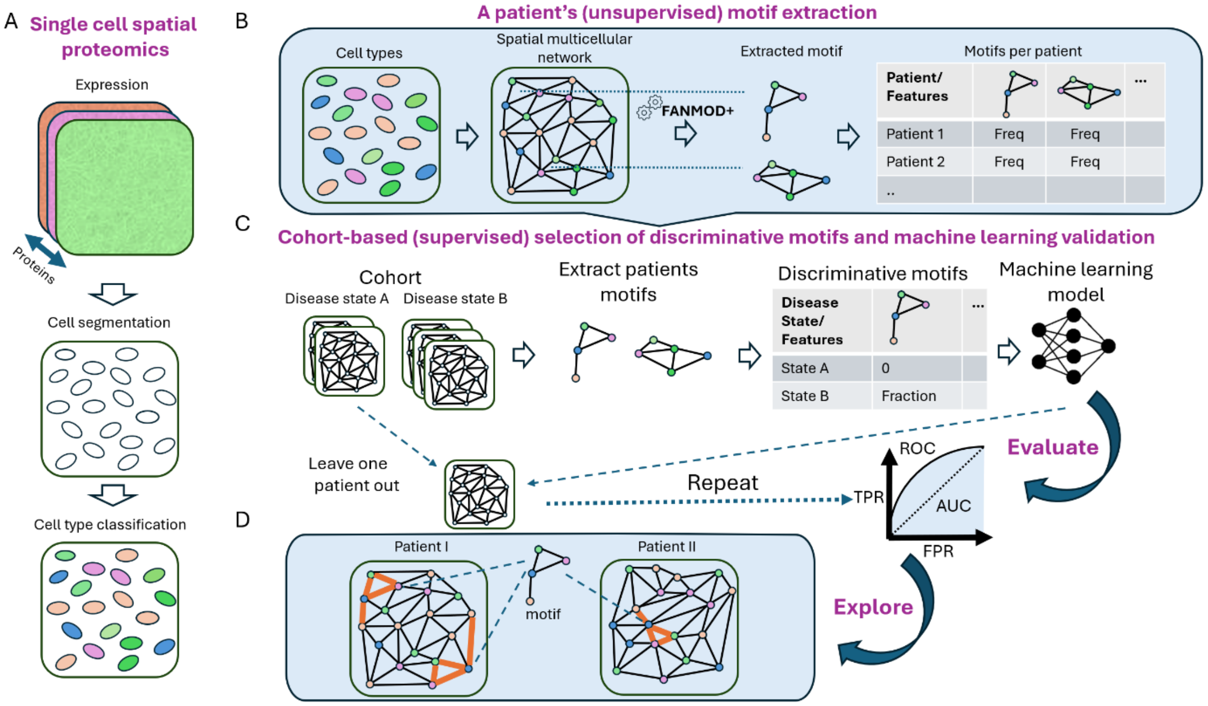

Figure 2.1. Extraction of spatial motifs, context-based selection, machine-learning evaluation, and visualization. (**A**) Single-cell type classification (top-to-bottom): multi-channel spatial proteomics data at single-cell resolution, cell segmentation, cell type classification. (**B**) Extract motifs using FANMOD+ from each patient and record the relative frequency of each motif. (**C**) Discriminative motifs and machine learning evaluation. Left-to-right: leave one patient out, extract motifs, select discriminative motifs, train a machine learning model to predict the disease tissue state using discriminative motifs as features, and evaluate the model on the left-out patient. Repeat this process for all patients and calculate the ROC according to the pooled prediction probabilities. (**D**) Moving back to space and interpreting. Overlaying the motifs on the spatial multicellular network – the motifs' localization in the tissue can infer the spatial contexts associating a motif to a disease state.

CISM classification of melanoma disease state

We were interested in the long-term metastatic propensity of early melanoma (stages I-II), defined as a primary tumor with no signs of spreading to nearby lymph nodes or to distant organs. Specifically, can we predict future widespread metastases in multiple distant organs from the single cell spatial organization of the (tumor-free) sentinel lymph node? We applied CISM to analyze a subcellular resolution 36 channels MIBI-TOF-acquired human cohort consisting of 76 tissue sections from lymph nodes of 38 stage I-II melanoma patients. Five years following treatment, the patients' clinical outcome was determined upon the prognosis of widespread metastases in distant organs (Fig. 2.2A). A patient with tumor-free lymph nodes and no distant metastases in five years was defined as negative-negative (NN). Correspondingly, those patients with remote metastases five years following diagnosis were defined as negative-positive (NP). We segmented single cells using DeepCell (Greenwald et al., 2022), applied CellSighter for cell type classified (Amitay et al., 2023), assigning each cell to one of 15 non-tumor lymph node microenvironment cell types according to their lineage relationships (Fig. S2.1, Methods), and defined the corresponding spatial multicellular network. The cell type distribution, defined by pooling all cells from all patients, was similar between NN and NP with a higher fraction of CD4 T-cells, Macrophages in NN and Germinal Center B cells, and Memory CD4 T-cells in NP (Fig. 2.2B). We applied FANMOD+ to extract hundreds to ten-thousands of 3-, 4-, and 5-cell motifs correspondingly. Next, we performed context-dependent motif selection according to the discrimination stringency parameter, which is the fraction of patients of a given clinical outcome (i.e., NN versus NP) that share a discriminating motif. This analysis showed similar numbers of discriminative motifs in NN and NP that exponentially decayed as a function of the fraction of the patients (with the corresponding clinical outcome) that shared the motif (Fig. 2.2C).

To systematically test whether discriminative motifs can provide a rich representation of the tissue disease state, we turned to machine learning validation. Specifically, we performed Random Forest-based leave-one-patient-out cross-validation where each patient was represented by a (sparse) feature vector of its discriminative motifs frequencies. Gradually increasing the discrimination stringency parameter revealed a trend of enhanced classification performance for discriminative motifs that appear in more patients for 3- and 4-cell motifs (Fig. 2.2D). The classification score reached a maximal AUC score of 0.88 with 4-nodes discriminative motifs that appeared in at least 46% of patients from one clinical outcome (and did not appear in patients from the other clinical outcome). Setting the discrimination stringency parameter to 0.46 has an additional benefit in limiting the number of discriminative motifs for downstream interpretation (Fig. 2.1D and Discussion). Motifs of size three led to inferior classification performance due to a lack of sufficient numbers of discriminative motifs (Fig. 2.2C-D), and 5-cell motifs reached an AUC score of 0.81 (discrimination stringency parameter = 0.2) that dropped for more stringent discrimination criteria due to training overfitting with few motifs per leave-one-out iteration (Fig. S2.2). CISM surpassed the alternative classification approaches of whole graph neural networks (Tamir et al., 2024) and pairwise cell type machine learning that reached a near random AUC of 0.53 (std = 0.02, Fig. 2.2D – cyan horizontal line) and 0.56 (std = 0.02, Fig. 2.2D – pink horizontal line) correspondingly (Methods for full details). To confirm that these results were not due to overfitting, we permuted the patients' clinical outcome labels and performed the full CISM classification pipeline. Repeating this permutation test 100 times produced AUC scores that were distributed around random (mean=0.4912, std=0.2138, p-value=0.01, Fig. S2.3). Cumulatively, CISM showed remarkable melanoma clinical outcome prediction, indicating that discriminative motifs can serve as multicellular modular signatures of a disease state with the fine spatial resolution of four cells and their spatial adjacencies.

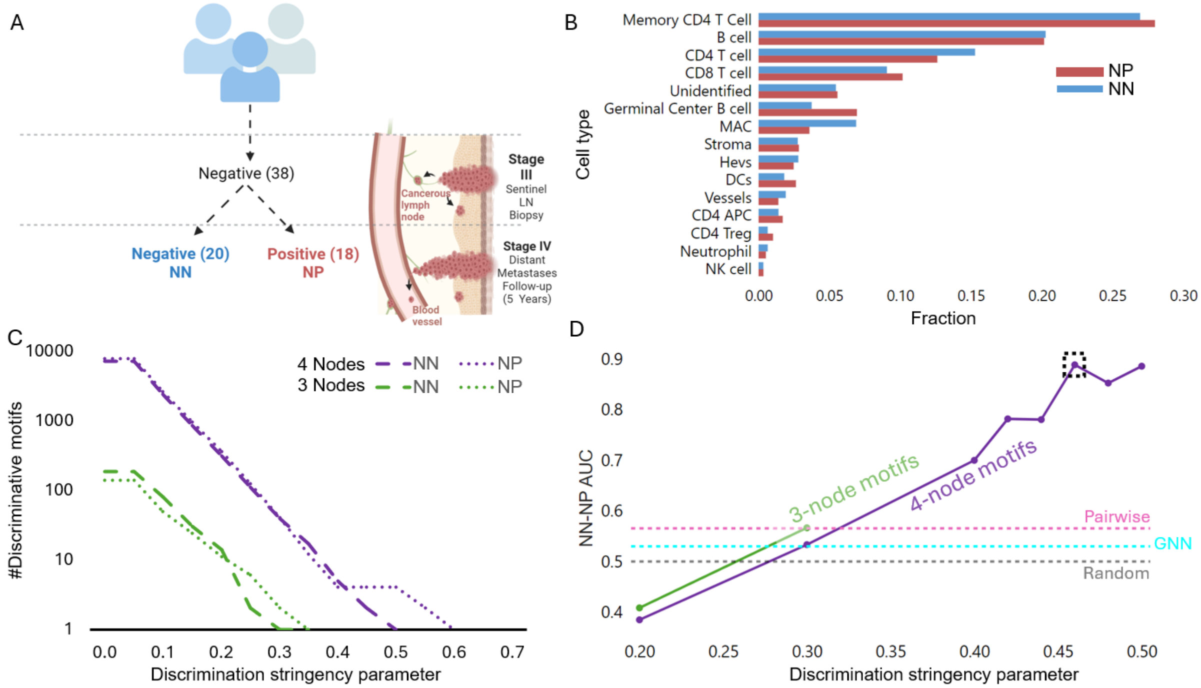

Figure 2.2. Context-dependent identification of spatial motifs (CISM) can predict melanoma disease state. (**A**) The melanoma cohort includes 38 patients diagnosed with a primary tumor with no apperant tumor cells spreading to the lymph node (i.e., melanoma stage I-II). 20 of these patients were not diagnosed with widespread melanoma metastasis five years following treatment (Negative-Negative, NN), while the remaining 18 patients were diagnosed with widespread metastases in distant organs (Negative-Positive, NP). (**B**) Cell type distribution for NN and NP patient groups. (**C**) The number of 3-cell (green) and 4-cell (purple) context-dependent discriminative motifs (y-axis, log scale) over the discrimination stringency parameter (x-axis) - a fraction of patients of a given clinical outcome that share a discriminating motif when none of the patients with the other clinical outcome share it. (**D**) Machine learning validation of melanoma disease state discrimination with CISM's discriminative motifs representation. Leave one patient out cross-validation (LOOCV) model performance (AUC) (y-axis) over the discrimination stringency parameter (x-axis) (green - 3-cell motifs, purple- 4-cell motifs). The pink, cyan, and black dashed horizontal lines represent the LOOCV AUC score of pairwise, GNN, and a random null model, correspondingly. The discriminative motifs derived from 4-cell motifs with the discrimination stringency parameter of 0.46 for discriminative motifs selection were used for further analysis. The sensitivity to the discrimination stringency parameter and to the number of motifs is shown in Fig. S2.4 and Fig. S2.5 correspondingly.

Discriminative motifs-induced pairwise cell-cell interactions

Can we use the discriminative motifs to learn discriminative cell-cell pairwise interactions that can not be obtained by direct analysis? To extract potential pairwise interactions from the motifs, we examined the 19 discriminative motifs (8/11 motifs associated with NN/NP correspondingly) that appeared most frequently in the machine learning analysis. Discriminative motifs-based pairwise interactions were measured according to the probability of two cell types being connected with an edge in the pooled set of instances of discriminative motifs appearances associated with NN or NP across the patient samples (Fig. 2.3A, Methods). This analysis revealed several potential pairwise interactions associated with one disease state and not the other. The top three highly ranked motifs-induced pairwise interactions disease signatures in NN and in NP are depicted in Fig. 2.3B. NN was associated with dominant interactions of Neutrophils with CD4 T-cells, Macrophages with CD8 T-cells, and CD8 T-cells with NK cells, while NP was associated with dominant interactions of B cells with CD8 T-cells, CD8 T-cells with CD8 T-cells, and Macrophages with CD8 T-cells. These disease state-associated pairwise interactions were not sensitive to the stringency of the motifs' discrimination criterion (Fig. S4). Importantly, explicitly enumerating the distribution of pairwise interaction for NN versus NP patients according to the probability of two cell types being connected with an edge in the multicellular network, without using the discriminative motifs, did not show a clear distinction in the context of disease state (Fig. 2.3C). This result suggested that the strict context-dependent discriminative motif selection refined the noisy landscape of cell-cell interactions in the full spatial multicellular network by focusing on the discriminative localized network motifs.

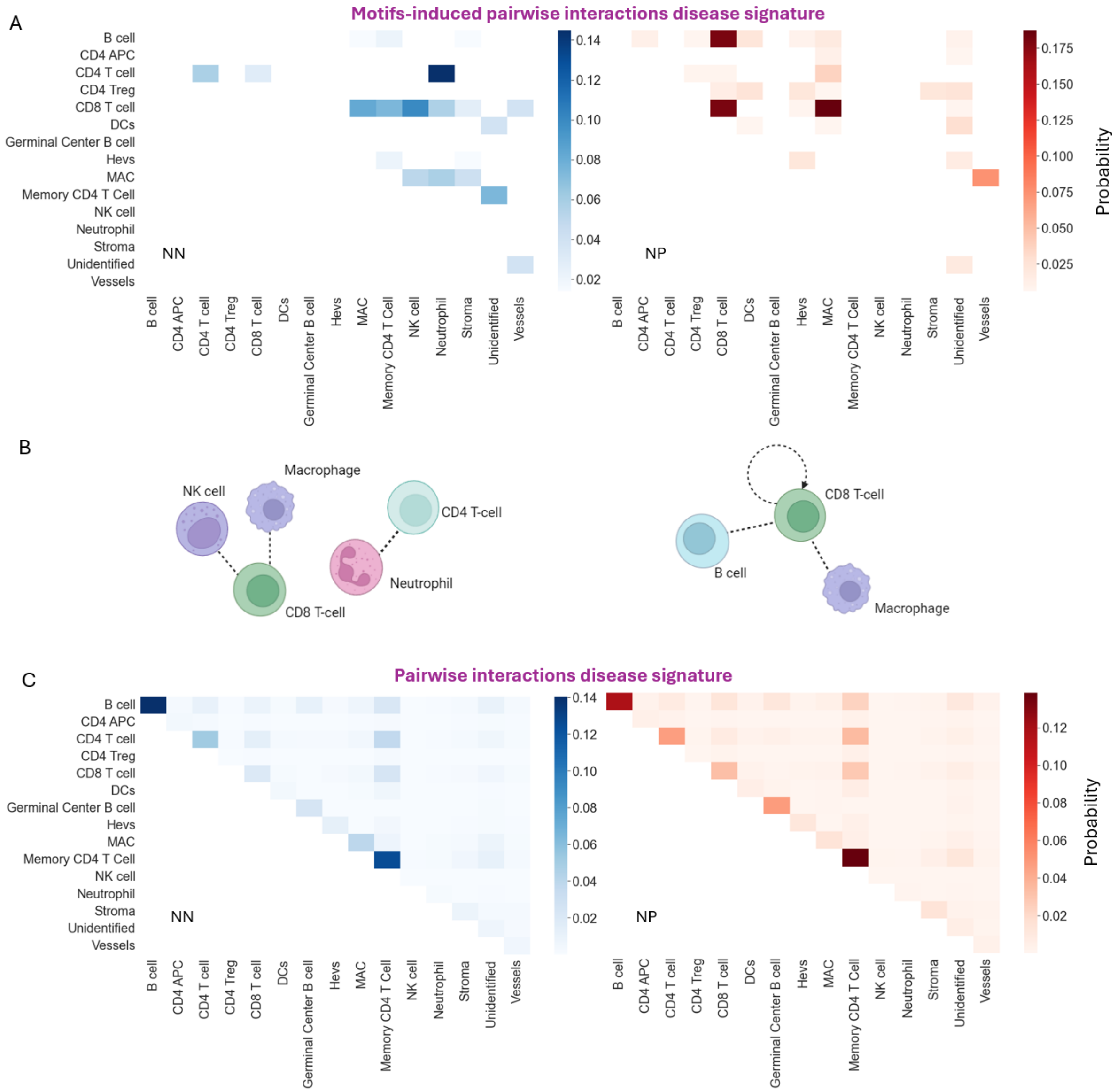

Figure 2.3. Context-dependent motifs-induced pairwise interactions melanoma disease state. (**A**) The distribution of motifs-induced pairwise interactions disease signature. The probability of two cell types to be connected with an edge in the cohorts' patients pooled set of instances of discriminative motifs associated with NN patients (left**,** n = 8 motifs) and NP patients (right**,** n = 11 motifs). (**B**) The top three highly ranked motifs induced pairwise interaction. (**C**) The distribution of pairwise interactions disease signature. The probability of two cell types to be connected with an edge in the cohorts' patients pooled set of multicellular networks.

The spatial organization of the cells within the motif contributes to the classification of melanoma disease state

A motif is defined according to its cell types and the edges between them. We next asked whether the discriminative motifs' cell type composition, i.e., the cell types without considering their relative spatial organization to one another, is sufficient to discriminate between the NN and NP disease states, or in other words – whether the spatial structure of discriminative motifs' matter for disease state classification? To answer this question, we repeated the steps of context-dependent motifs' selection and machine learning analysis, but instead of using the discriminative motifs we used the discriminative *cell type composition* representations. The cell type composition of a motif was represented as a sparse vector that encodes the number of occurrences of each cell type in the motif. For example, a 4-cell motif that includes two edges from a HEV to two memory CD4 T-cells and two edges from a B-cell to the same two memory CD4 T-cells is transformed to a sparse vector encoding a single B-cell, one HEV cell, and two memory CD4 T-cells (Fig. 2.4A). This cell type composition representation was less specific and thus induced much fewer discriminative cell type compositions with respect to the (more specific) discriminative motifs (Fig. S2.6A). Machine learning evaluation confirmed that the cell type composition representation failed to generalize to discriminate between NN and NP disease states (Fig. S2.6B).

To directly assess which of the discriminative motifs' spatial organizations are most associated with the disease state, we devised an approach that measures the gain in classification performance attributed to the inclusion of each discriminative motif's spatial organization instead of its corresponding cell type composition. First, we transformed the representation from the discriminative motifs space to the cell type composition space by replacing each discriminative motif with its corresponding cell type composition (Fig. 2.4B). Note that multiple discriminative motifs can be mapped to the same cell type composition, and that a cell type composition can include instances of motifs that did not meet the strict discrimination stringency parameter used to determine the discriminative motifs. This discriminative motifs-derived cell type composition representation reached a reduced AUC score of 0.655, which was used as a baseline (Fig. 2.4B, middle). Specifically, in this case each discriminative motif was mapped to one cell type composition. Second, beginning from this cell type composition representation, we iteratively introduced back the spatial information for each cell type composition by replacing it with discriminative motifs that induced it. This replacement created a hybrid representation that contained both cell type composition and discriminative motif features (Fig. 2.4B, right). This hybrid representation was used for machine learning assessment, where the contribution of the corresponding motifs' spatial organization was attributed to the classification gain with respect to the cell type composition baseline. The classification gain for each cell type composition was ranked, showing that the vast majority (17/19) of the motifs' spatial structure contributed to disease state prediction (Fig. 2.4C). The three highest ranked cell type compositions included "unidentified" cell types, i.e., cells without a specific classification, and thus were not further analyzed. The 4th highest ranked cell type composition contributed 0.11 to the cell type composition baseline AUC, and was composed of one B cell, one high-endothelial venule (HEVs) cell, and two memory CD4 T cells (Fig. 2.4C motif #I in green, this motif was used as an example in Fig. 2.4A-B). The 5th highest ranked cell type composition contributed 0.09 to the baseline AUC and was composed of a CD4 T cell, a pair of Macrophage cells, and a vessel cell (Fig. 2.4B motif #II in orange; this motif was used as an example in Fig. 2.4B). To further verify that the spatial structures of these motifs are more discriminate than their corresponding cell type compositions, we counted the number of instances of these motifs and their corresponding cell type compositions across the cohort's patients. While the number of instances of the cell type compositions induced by motifs I and II did not show clear discrimination between the disease states (Fig. 2.4D, top), the prevalence of motifs I and II clearly discriminated between NN and NP (Fig. 2.4D, bottom). Thus, distilling the contribution of the discriminative motifs' spatial structures indicates that the specific intra-motif direct cell-cell interactions are more sensitive as markers for disease state with respect to the corresponding motif's cell type composition.

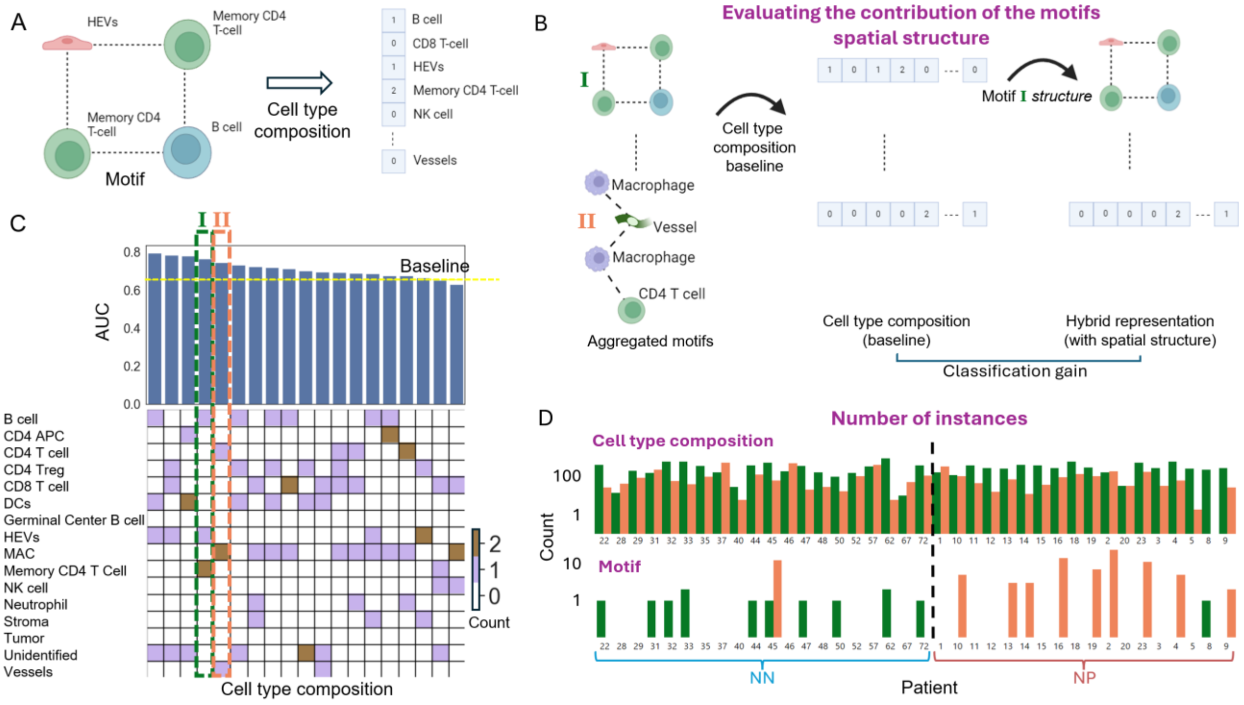

Figure 2.4. The spatial structures of discriminative motifs contribute to disease state classification. (**A**) An example of mapping a discriminative motif (left) to its corresponding cell type composition (right). The cell type composition representation is 16-dimensional, counting the number of instances of each cell type in the input discriminative motif. (**B**) Assessing the discriminative contribution of the spatial structure of discriminative motifs. First, all the discriminative motifs (left) are mapped to their corresponding cell type compositions (middle). This discriminative motifs-derived cell type composition representation is used to train a baseline machine learning model to predict the disease state. Second, the contribution of the spatial structure is measured as the classification performance gain by replacing one cell type composition with its corresponding discriminative motifs, one at a time (right). (**C**) The ranked classification gain for each cell type composition of the n = 19 discriminative motifs (x-axis). Specifically, each column represents a cell type composition, each row represents a cell type, and the color encodes the number of cell type instances in the corresponding cell type composition. For example, the cell type composition #I corresponds to one B cell, one HEV, and two memory CD4 T cells (see panel A). The deviation of the AUC of a cell type composition baseline (yellow dashed line, AUC = 0.655) with respect to its corresponding hybrid representation (blue bar) is the classification gain. The spatial structure of 17/19 of the motifs contributed to the disease state prediction. Two motifs and their corresponding cell type compositions (I – green, II - orange), whose spatial structure contributed the most while not containing (less interpretable) "unidentified" cell types, were highlighted for further analysis. (**D**) The number of instances of the cell type compositions I (green) and II (orange) are shown in panels B-C (top) and their corresponding motifs (bottom). The outlier motifs II (patient #45) and I (patient #8) were selected when the corresponding patient was used for the test (i.e., was selected as discriminative when not considering that patient). The cell type compositions did not discriminate between NN and NP (Mann-Whitney U test: cell type compositions I (green): p-value = 0.6398, cell type compositions II (orange): p-value = 0.5586), while the motifs significantly discriminate between NN and NP (motifs I (green): p-value = 0.0029, motifs II (orange): p-value = 0.0032)

Spatial interpretation of a NP-associated motif localization reveals an "adaptor" between the B cells surrounding the germinal center and the rest of the immune microenvironment

One of the most appealing attributes of CISM is the ability to locate instances of a discriminative motif in the multicellular network and characterize the stereotypic spatial contexts associated with its localization and the disease state. Observing that a discriminative motif is consistently localized in a specific microenvironment can drive the interpretation of potential mechanisms regarding the motif's physiological roles in the context of the disease. To decide which discriminative motifs to spatially interpret, we balanced between two desired properties: (1) generalization – discriminative motifs that appeared in many patients, and (2) interpretability – discriminative motifs with many instances per patient. Placing the 19 NN-NP discriminative motifs on this generalization-interpretability axes highlighted three motifs that appeared in many patients with many instances per patient, on average (Fig. 2.5A). Motif I (green) was NN-associated and included a Macrophage, Neutrophil, and a pair of CD4 T cells, motif II (magenta) was also NN-associated and comprised of an NK cell, a CD8 T cell, a Memory CD4 T cell, and an Unidentified cell, and motif III (yellow) was NP-associated and comprised of a Macrophage, a pair of CD8 T cells, and a B cell (Fig. 2.5B). Motif III was found to be the most abundant in several NP patients and was thus used for spatial interpretation (Fig. 2.5D). Localizing motif III in the tissue revealed a stereotypical spatial pattern appearing at the edges of B cell clusters that surround the germinal center (Fig. 2.5D, Fig. S2.7). The motif's B cell was part of the germinal center-associated B cell cluster that was adjacent to two CD8 T cells that were adjacent to a macrophage, perhaps serving as a specific "adaptor" of the germinal center to the rest of the immune microenvironment that associates with long-term metastasis progression. These results highlight the possibility of providing physiologically meaningful interpretation by observing the spatial localization of CISM-derived discriminative motifs.

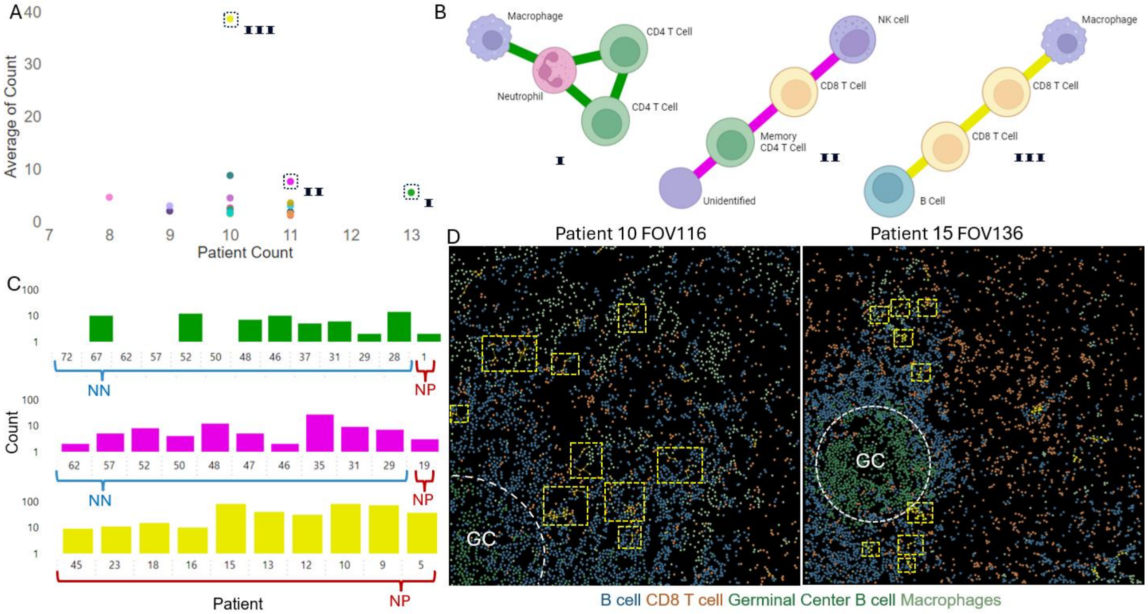

Figure 2.5. Moving back to space to characterize the microenvironment of abundant discriminative motifs. (**A**) The mean per-patient number of discriminative motif instances (y-axis) in relation to the number of patients that contained that motif (x-axis). Each dot represents a discriminative motif (n = 19). Note motifs I (green), II (magenta), and III (yellow) that appear in many patients and in many instances per patient. (**B**) The three discriminative motifs that were marked in A. The edge colors are consistent across the other figure panels. (**C**) The number of instances of motifs I-III (top-bottom, log scale) across patients. Only patients with at least one instance were listed. (**D**) Localizing motif III in the tissue of NP patients #10 (left) and #15 (right) and in additional patients (Fig. S2.7). Each dot represents a cell colored according to its cell type: B cell, CD8 T cell, Germinal Center B cells, and macrophages (other cell types are not shown). The germinal center (GC) is surrounded by a dashed white circle. Instances of motif III are marked with dashed yellow rectangles (larger rectangles indicate multiple instances of the motif).

Context-dependent NP-associated discriminative motifs

CISM's context dependency implies that the same motifs extracted from a specific tissue can be differentially analyzed according to the question at hand – via context-dependent selection of the discriminative motifs. To test how context can alter the motifs-induced pairwise interactions disease signature and the spatial interpretation of the motifs' localization, we turned to the extended melanoma cohort that included 13 stage III melanoma patients who healed, i.e., those patients with metastatic sentinel lymph nodes, and a five years follow up prognosis of tumor-free lymph nodes and no metastases, these were defined as positive-negative (PN). Specifically, we asked what were the similarities and differences in discriminative motifs extracted from NP patients in the different contexts of NN (Fig. 2.2A) versus PN (Fig. 2.6A). Focusing on changes in the organization of the lymph node immune microenvironment, we excluded all cells inside the tumor cell clusters in PN patients using a refined version of the convex hull algorithm (Kirkpatrick & Seidel, 1983, Methods). Cell type classification showed a similar cell type distribution for NP and PN patients (Fig. S2.8A). CISM analysis of NN versus NP found the optimal tradeoff between classification performance and sufficient discriminative motifs and their instances for interpretability in 5-cell motifs and discrimination stringency of 0.4 (Fig. S2.8B-C). CISM reached an AUC of 0.81, surpassing pairwise cell type machine learning (Fig. S2.8C – pink horizontal line) and GNN with an AUC of 0.674 (Fig. S2.8C – cyan horizontal line). The motif-induced pairwise interactions showed a clear signature distinguishing between the disease states (Fig. S2.9). PN was associated with interactions of Macrophages with Vessel cells, Vessel cells with Stroma cells, Germinal center B cells with B cells, and CD4 T-cell with B cells, while NP was associated with interactions of B cells with CD8 T-cells, B cells with B cells, and B cells with Memory CD4 T-cells (Fig. 2.6B). Most of the discriminative motifs' induced pairwise interactions appeared in either NP-vs-NN (Fig. 2.3A) or in NP-vs-PN (Fig. 2.6B), but not in both. The one pairwise interaction that appeared in NP in both contexts was between B cells and CD8 T-cells, suggesting these interactions as potential promoters of metastases. Remembering that interactions of B-cells and CD8 T-cells appeared, in the context of NN-vs-NP, as part of discriminative motifs localized at the edges of B cell zones that surrounded the germinal center (Fig. 2.5D), we repeated the spatial interpretation of three prominent discriminative motifs (Fig. 2.6C-F).

Since the function depends on the motif location in the tissue, we chose to observe the motif instance locations of the second and third motifs since both are located around the GC but in different layers. The second associated with PN is spatially located in the cross-layer surrounding the GC between the GC and inner circle of the B cell (Fig. 2.6F, right). The third associated with NP, its spatial location is repeated constantly in the layer of B cells surrounding the germinal center (Fig. 2.6F, left), the same as we observe with a third motif that was associated with NP in the context of NP versus NP (Fig. 2.5D). Altogether, both the top pairwise interaction between the B cell and CD8 T cell and the spatial location of the motifs within the tissue suggest that the interaction of B cell with CD8 T cell could act as a predictor for Melanoma disease prognosis.

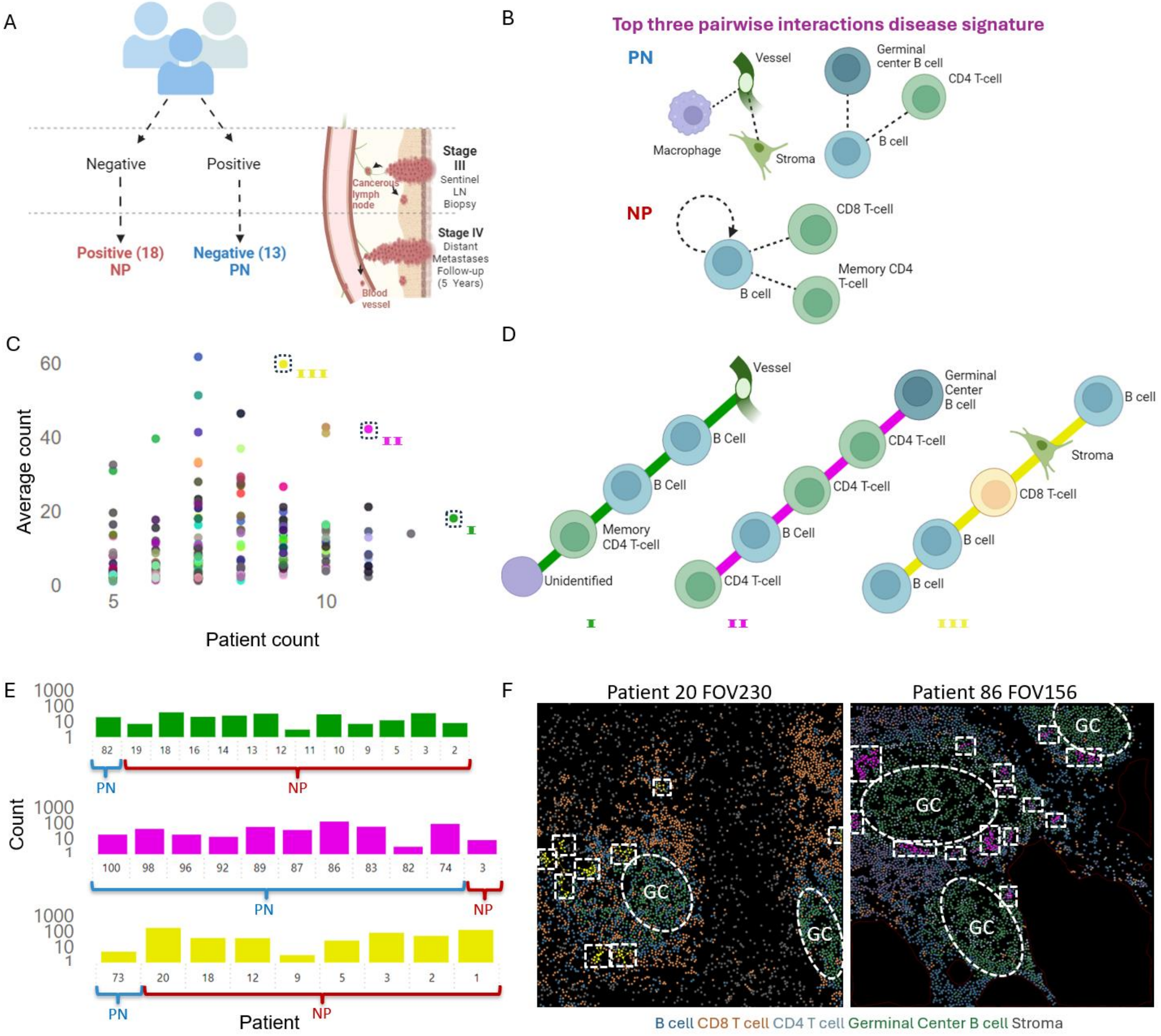

Figure 2.6. CISM analysis of NP versus PN. (**A**) The cohort includes 18 patients diagnosed with a primary tumor with no apparent tumor cells spreading to the lymph node (i.e., melanoma stage I-II) with widespread melanoma metastasis five years following treatment (Negative-Positive, NP), and extended

with 13 stage III melanoma patients who healed, i.e., those patient with metastatic sentinel lymph nodes, and a five years follow up prognosis of tumor-free lymph nodes and no metastases (Postive-Negative, PN). (**B**) The top three highly ranked motifs induced pairwise interaction. The full distribution of motifs-induced pairwise interactions disease signature appears in Fig. S2.9A. (**C**) The mean per-patient number of discriminative motif instances (y-axis) in relation to the number of patients that contained that motif (x-axis). Each dot represents a discriminative motif (n = 210). Note motifs I (green), II (magenta), and III (yellow) that appear in many patients and in many instances per patient. (**D**) The three discriminative motifs that were marked in C. The edge colors are consistent across the other figure panels. (**E**) The number of instances of motifs I-III (top-bottom, log scale) across patients. Only patients with at least one instance are listed. (**F**) Localizing motif III in the tissue of NP patient #20 (left) and motif II in the tissue of PN patient #86 (right). Each dot represents a cell colored according to its cell type: B cell, CD8 T-cell, CD4 T-cell, Germinal Center B cells, and Stroma (other cell types are not shown). The germinal center (GC) is surrounded by a dashed white circle. Instances of motifs II and III are marked with dashed pink and yellow rectangles (larger rectangles indicate multiple instances of the motif).

Generalizing CISM to reveal motifs associated with triple-negative breast cancer disease state

To demonstrate generalization, we applied CISM to analyze a MIBI-TOF-acquired human TNBC cohort consisting of 38 tissue sections of 37 patients (Keren et al., 2018). We partitioned the patients into short-term (less than 1000 days, N = 7 patients) and long-term (more than 1000 days, N = 30) survivors according to the time a person lived after diagnosis (Fig. S2.10A). Using the cell type classification (Fig. S2.10B) we applied CISM to extract 3- and 4-cell motifs and then selected those that discriminated between short- and long-term survivors with a smaller number of short-term associated discriminative motifs attributed to the imbalance between the disease states (Fig. S2.11). Note that unlike the melanoma cohort, where lymph nodes did not necessarily include tumor cells (NN and NP), in the TNBC cohort we did consider the tumor cells and their interactions with cells in the tumor microenvironment.

Machine learning validation reached an AUC of 0.88, surpassing pairwise cell type machine learning and GNN (Fig. 2.7A, Fig. S2.12). Discriminative motifs-based pairwise interactions revealed that long-term survivors were associated with the pairwise interactions of DC/MONO cells with CD4 T cells, CD8 T cells with CD4 T cells, and between CD4 T cells, while the pairwise interactions associated with short-term survival were of Mesenchyme cells with a CD8 T cells and Neutrophils with CD8 T cells (Fig. 2.7B, Fig. S2.13). These results propose interactions of CD4 T cells with other immune cells as a marker for long-term survival in contrast to interactions of CD8 T cells with other tumor microenvironment cells as a marker for short-term survival.

We next repeated the spatial interpretation of three prominent long-term survivors-associated discriminative motifs (Fig. 2.7C-F). Two of these three motifs (I and III) included interactions that involved CD4 T cells. In (Keren et al., 2018), we discovered that a clear spatial boundary between tumor and immune cells, termed “compartmentalization”, was associated with long-term survival. Here, we show that the appearance of discriminative motifs associated with long-term survival might resolve the survival of patients with a “mixed” (i.e., not compartmentalized) tumor-immune phenotype. For example, patient #1 survived over 7 years since diagnosis, with the “mixed” phenotype (Fig. 2.7F). These results raise the possibility that specific interactions between CD4 T cells and tumor and/or dendritic cells may be markers for long-term survival in the “mixed” phenotype.

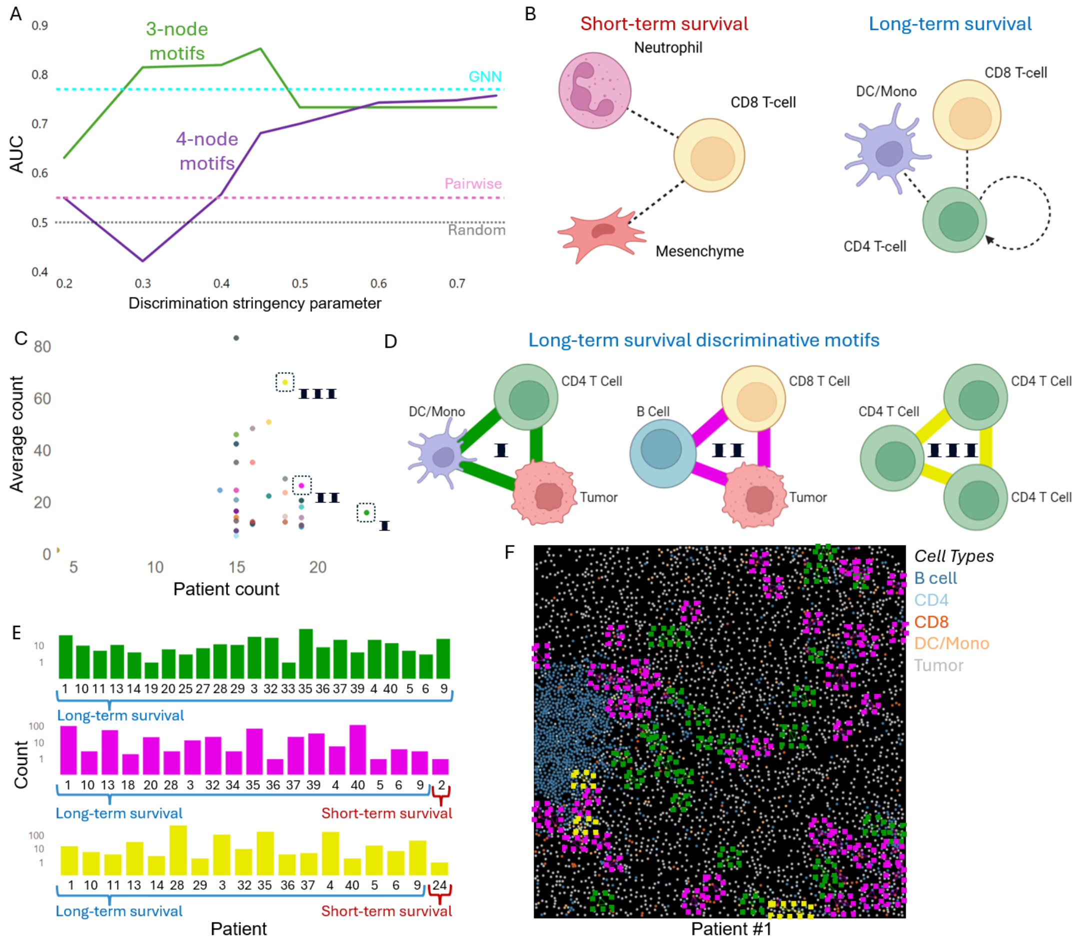

Figure 2.7. CISM analysis of triple-negative breast cancer cohort. (**A**) Machine learning validation of CISM's discriminative motifs representation of TNBC short-term versus long-term survival discrimination. Leave one patient out cross-validation (LOOCV) model performance (AUC) (y-axis) over the discrimination stringency parameter (x-axis) (green - 3-cell motifs, purple- 4-cell motifs). The pink, cyan, and black dashed horizontal lines represent the LOOCV AUC score of pairwise, GNN, and a random null model, correspondingly. The discriminative motifs derived from 3-cell motifs with the discrimination stringency parameter of 0.45 were used for further analysis. (**B**) The top three highly ranked interactions of motifs induced pairwise interaction. (Fig. S2.13A) Note that short-term survival had a single discriminative motif and thus, there are two interactions. (**C**) The mean per-patient number of discriminative motif instances (y-axis) in relation to the number of patients that contained that motif (x-axis). Each dot represents a discriminative motif (n = 33). Note that motifs I (green), II (magenta), and III (yellow) are all associated with long-term survival and appeared in many patients and in many instances per patient. (**D**) The three discriminative motifs that were marked in C. The edge colors are consistent across the other figure panels. (**E**) The number of instances for motifs I-III (top-to-bottom, log scale) across patients. Only patients with at least one instance were listed. (**F**) Localizing motifs I-III in the tissue of patient #1. Each dot represents a cell colored according to its cell type (right legend; other cell types are not shown). Instances of motifs I, II, and III are marked with dashed green, pink, and yellow rectangles correspondingly. Larger rectangles indicate multiple instances of the motif.

Discussion

CISM is a two-step method for identification and characterization of fine-grained spatial inter-cellular modules associated with the physiological tissue states. First, using our FANMOD+ implementation, we are able to extract, in an unsupervised manner, all of the many spatial motifs in the patients' multicellular spatial networks. Second, we select, in a supervised manner, the discriminative motifs according to the patients' context. This approach distills the discriminative motifs from the noisy landscape of all possible cell-cell interactions. These discriminative motifs can then be used for several downstream applications that we demonstrated in 3 different contexts in melanoma and TNBC: machine learning prediction of tissue's physiological context, identifying "signature" discriminative motifs and motifs-derived pairwise interactions that associate with the physiological context, and moving back to space to interpret the discriminative motifs' stereotypic localization patterns. CISM outperforms GNN and pairwise interactions representations in predicting disease tissue state, indicating that discriminative motifs can serve as powerful representations of tissue disease state. Importantly, the exact spatial organization of the cells within the motifs, in terms of their specific cell-cell adjacencies (as indicators of potential interactions), contributed to the discrimination between different disease states. These results suggest that the local organization of a few cells as discriminative motifs are emergent properties that may define an intermediate spatial scale driving tissue function.

Although GNNs have shown great promise in classifying tissue states across multiple diseases (Tamir et al., 2024; Wu et al., 2022; Wu & Zou, 2022), their success comes at the cost of "black box" poor interpretability. This inherent difficulty in providing human meaningful explanations for the GNN's decision hampers the possibility of generating specific mechanistic hypotheses. CISM approach of feature (i.e., discriminative motif) selection resembles the more interpretable classic machine learning approach, with "engineered" features that are easier to decipher. The exhaustive enumeration of all motifs provides these desired joint properties of discrimination power along with interpretability. Specifically, CISM offers several layers of interpretability. First, discriminative motifs-induced pairwise interactions disease signatures highlight specific cell-cell interactions that associate with the tissue state. Second, the ability to map discriminative motifs back to their location in the tissue space enables the linking of the two different spatial scales by characterizing the (fine scale) motif's localization in relation to a (coarse scale) specific spatial context, who are jointly stereotypic in a specific disease state. We demonstrated these interpretability capacities when associating the discriminative motifs-induced pairwise interactions of B cells with CD8 T-cells in the signature of tumor-free lymph nodes that progressed to widespread metastases in distant organs (i.e., NP patients). This pairwise discriminative association appeared in both contexts of PN and of NN patients.). These results suggest that the interactions of B cells with CD8 T-cells might act as tumor promoters in the early stages of melanoma metastasis. This observation possibly adds the interaction with CD T-cells as a potential explanation for specialized B regulatory cells that take a key role in immune suppression by the production of IL-10+ cytokines and act as a pro-tumorigenic factor (Griss et al., 2019; Sarvaria et al., 2017; Shen & Fillatreau, 2015), and with other studies suggesting a pro or anti-tumor role of B-cells (Griss et al., 2019). Linking the interaction through discriminative motifs back to space, we found out that the spatial location of the dominant discriminative motif (Fig. 2.5B III associated with NP) in the layer of B cells surrounding the germinal center in the context of NP versus NN embodies the interaction of B cell and CD8 T-cell, repeated constantly in the context of PN versus NP in different dominant motif (Fig. 2.6D III associated with NP, Fig. 2.6F, left). Similarly, when applying CISM to TNBC, we associated long-term survival with interactions of CD4 T-cells with CD8 T-cells and with DC/Mono cells, aligning with previous studies showing the importance of interactions between CD4 T-cells and DC cells to suppress tumor cells (Lei et al., 2023), and associating survival with higher ratios of CD4 to CD8 T-cells (Tenggara et al., 2024).

Beyond enabling biological insight at the spatial scale of a few cells, CISM benefits from several additional advantages. The strategy of unsupervised motifs enumeration followed by supervised context-dependent selection enables us to use the same motifs to answer different questions as shown for melanoma NP versus NN/PN. Moreover, this approach is suitable to characterize differences in small cohorts, for example, in matched healthy-versus-disease tissue of the same single patient. However, like any other method, CISM also suffers from several drawbacks. The fine resolution of a few cells and their spatial organization inherently implies that CISM is not forgiving to errors in cell segmentation and in cell type classification. Also, CISM has multiple parameters that must be carefully configured. First, the cell type lineage resolution. Using more cell types provides better discrimination and more specific biological insight at the cost of combinatorically increasing the size of the motifs space. Thus, beyond increasing the required computational resources, this implies a dramatic decrease in the number and prevalence of discriminative motifs. Similar considerations take place regarding the choice of the motif's size and the discrimination stringency parameter with better discrimination, in principle, but lower probabilities to generalize across patients. Practically, CISM users should balance these parameters according to readout, such as the plot of the number of discriminative motifs (Fig. 2.2C) and the discrimination performance (Fig. 2.2D) as a function of the discrimination stringency parameter. For example, in the melanoma dataset, 15 cell types generalized better than the full resolution 26 cell types, allowing us to be more strict in setting the discrimination stringency range. Automated parameter calibration is a possible direction for future research. The strict definition of a discriminative motif as appearing in a sufficient fraction of patients of one clinical outcome but excluded from all patients of the other outcome could be too restrictive, especially with the expected increase in cohorts' sizes in upcoming years, which inherently decreases the probability for the presence of discriminative motifs. This requirement for "hard" discrimination can lead to situations where motifs appear in many patients and even in many instances of patients of one clinical outcome but also in very small fractions of patients of the other outcome. These "almost discriminative" motifs could have great discriminative and interpretative value but are currently entirely excluded from our analysis. To remedy this limitation, CISM could incorporate a more flexible "soft" discriminative approach that selects the motifs according to a distance function between distributions of motif frequencies of each clinical outcome (e.g., the Wasserstein distance (Vaseršteĭn, 1969)). The implementation of "soft" discrimination could also be useful in extending CISM to support discrimination of multiple disease states and to incorporate motifs with finer resolution in their cell types and cell states. These ideas are left to future studies.

Methods

Experimental data

Melanoma MIBI-TOF

We analyzed a soon-to-published MIBI-TOF-acquired cohort of 51 human melanoma patients from Leeat Keren's lab at the Weizmann Institute of Science. The patients' disease state was determined according to the clinical diagnostic of the sentinel lymph nodes (SLN) and then five years following treatment. Patients with or without the existence of tumor cells in their SLNs were defined as "positive" or "negative," respectively. Those patients who were diagnosed with the prognosis of widespread metastases in distant organs five years following treatment were defined as "negative-positive" (NP), while those who did not were defined as "negative-negative" (NN) or "positive-negative" (PN) according to their initial diagnosis. Cumulatively, we analyzed three patient groups: NN (N patients = 20, n tissue sections FOVs = 40), NP (N = 18, n = 36), and PN (N = 13, n = 42). The dataset includes 36-channel MIBI-TOF of SLNs with a resolution of 0.5x0.5 µm per pixel. Segmentation masks were generated using DeepCell2 (Bannon et al., 2021a, 2021b), and each cell was classified using CellSighter (Amitay et al., 2023) into one of 26 subtypes. We reduced the cell type resolution to 16 cell types according to their lineages (Fig. S2.1).

TNBC MIBI-TOF

We analyzed a published MIBI-TOF-acquired human cohort TNBC dataset (Keren et al., 2018) that included 37 patients and 36 tissue sections with 36 protein channels and a spatial resolution of 0.5x0.5 µm per pixel. We used cell segmentation masks and assignment of each cell to one of 16 cell types as in the original study. The cell types used in this dataset include Tumor, Endothelial, Mesenchyme, Tregs, CD4 T cells, CD8 T cells, CD3 T cells, NK cells, B cells, Neutrophils, Macrophages, DC, DC/Mono, Mono/Neu, Immune other and Unidentified. We used the number of survival days since diagnosis as the clinical readout where patients who survived less than 1,000 days were defined as "short-term" survivors, and those who survived at least 1,000 days were defined as "long-term" survivors.

Computational modeling

Defining the spatial multicellular network

We defined the spatial multicellular network, where single cells define the network nodes and are “colored” according to their cell type. Close-adjacent pairs of cells are connected with an edge using the Delaunay triangulation, excluding those edges between cells that are more distant than 50 µm away from one another.

Excluding tumor clusters from melanoma PN patients’ lymph node

In the melanoma cohort, we focused on disease-associated alterations of the lymph node immune microenvironment, specifically because NN and NP patients did not have tumor cells in their lymph nodes. Thus, when handling PN patients, we had to exclude tumor cells. We opted to exclude from the multicellular network all cells (tumor and non-tumor) in regions enriched with tumor cells to avoid potential tumor-immune interactions, as an obvious bias indicative of PN patients, which could serve as a “shortcut” for classification. Thus, we used the “alpha shape” (Kirkpatrick & Seidel, 1983), a generalization of the convex hull for a set of points in space (in our case - cell localizations) based on parameter α that controls the shape’s sensitivity. For α equal to zero, the alpha shape of a point set is the same as its convex hull. As α increases, the alpha shape shrinks with concave regions (derived from the point set) beginning to appear, gradually "cutting out" voids and indentations in the shape. We empirically set α to 0.01 after manual calibration (Fig. S2.14). Overall, we adjusted the multicellular network using the following pipeline: (1) identify all tumor cells, (2) divide them into connected components in the multicellular network, (3) calculate the alpha shape, and (4) exclude all cells inside the alpha shape from further analysis.

FANMOD+ implementation enables the extraction of large and multi-colored motifs

We adapt and extend the concept of “network motifs”, reoccurring sub-networks that define “building blocks” of complex networks (Milo et al., 2002), to characterize the fine-scale organization of multicellular spatial networks of human disease tissues. One of the important characteristics of the motif is a statistical measurement of its significance. A subgraph is considered a motif if its frequency in the observed graph precedes its frequency in random graphs generated by edge-switching that preserves the graph's degree distribution. There are several existing tools to extract network motifs, but all have limitations regarding the motif size (i.e., number of cells) and the number of node "colors", and graph type support (i.e., multigraph, directed/undirected graph). The only method that we found that supports node coloring is called FANMOD (Wernicke & Rasche, 2006). However, FANMOD has limitations on the number of colors as a function of the motifs' size that it can analyze. Specifically, the maximum number of node colors that FANMOD can analyze is 15, and this number decreases as the motif size increases: at most, 15 colors for 4-node motifs and no coloring for 8-node motifs. This is a severe limitation for spatial single cell multiplexed data characterized by multiple cell types. We realized that this was an implementation (rather than algorithmic) limitation and thus adjusted the FANMOD source code, using the C++ boost library, to enable larger motif detection. We call our implementation FANMOD+ and it is publicly available at https://github.com/zaritskylab/FANMODPlus.

In more detail. To enumerate the set of all unique subgraphs within the network, Fanmod generates a unique representation of each subgraph, known as the "canonical representation", that is invariant for different organizations of nodes and edges (i.e., isomorphic graphs are mapped to the same representation). Specifically, Fanmod is using the Nauty algorithm (McKay & Piperno, 2014) to generate a canonical representation that is encoded as a sequence of bits. FANMOD+ increases the space (i.e., number of bits) for the canonical representation from 64-bit fixed allocation to 128-bit dynamic allocation (i.e., physical memory allocation extended when used) (Schäling, 2011). Thus, FANMOD+ subgraph canonical representation enables the encoding of more colors and larger motifs, supporting the analysis of modern spatial multiplex single cell omics data. For instance, with 0-32 colors, FANMOD+ can support a maximal motif size of 5 nodes; with 128 colors, FANMOD+ can support a maximal motif size of 4 nodes. Note that increasing the motif size or the number of colors still has a computational cost (Fig. S2.15, description on next section).

FADMOD+ benchmarking

To assess how the execution time increases as a function of more colors and larger motifs, we performed benchmarking using randomly generated graphs (Fig. S2.15). Since, on average, there are 10,000 cells in each patient's sample, we generated random graphs with n = 10,000 cells, each represented as a pixel, randomly spread on a grid of size 10,000 x 10,000 pixels and connected nearest neighbors cells using Delaunay triangulation with ~30,000 edges (~3n following the Euler rule for planar graph when $n \geq 3$). We generated five random graphs for each combination of motif size (3-5) and colors (in the range of 8-128). Due to RAM usage limitations of 64GB, we limited our benchmarking to five nodes and 32 colors. The benchmarking was executed on an AMD Ryzen 9 5900HX CPU with 64GB RAM.

Extracting network motifs with FANMOD+

We applied FANMOD+ to each patient's tissue sample to extract and enumerate thousands of motifs of size 3-to-5 cells. We calculated each n-cells motif's frequency with respect to the total number of corresponding subgraphs of size *n* in the patient's sample. We used 1000 random graphs for the statistical test and included only the significant motifs for the analysis ($p\text{-value} < 0.05$).

Selecting discriminative motifs

Context-dependent discriminative motifs are those motifs that sufficiently appear in patients of one physiological context and do not appear at all in patients of the other physiological context. The degree of presence of a motif in each given context is measured as the fraction of patients in that context that had at least one instance of that motif. Discriminative motifs were selected based on a tunable *discrimination stringency parameter* that defines a threshold on the degree of presence in a given context with the constraint that the motif does not appear in any of the patients of the other context.

Ranking discriminative motifs

To reduce the computational complexity, easier interpretability and removing relatively redundant features, in each iteration of leave-on-out we selected the top *n_disc_motifs* discriminative motifs. The ranking of the patients' discriminative motifs was determined according to their frequencies - the ratio between the number of motif instances to the total number of corresponding subgraphs (of the motif's size) in the patient's sample. With fewer features, it's easier to understand and explain the model's decision-making process and reduce noise from discriminative motifs with relatively very low frequency. Our assumption was that motifs that appears in more patients and in more instances per patient are a preferable representation of the physiological context.

Machine learning evaluation of the discriminative motifs representation

To assess the discriminative capacity of motifs' representation of the disease tissue state we performed Random Forest-based leave-one-patient-out cross-validation for binary classification between two disease contexts. The reason for the leave-one-patient-out cross-validation was the small cohorts sizes that are usually limited to tens of patients. Thus, we performed iterations of training and testing, each iteration with one patient at the test and the rest used for training. Each iteration followed the processes depicted in Fig. 2.1C (left-to-right): (1) keeping one patient out, (2) extracting motifs from all remaining patients, (3) selecting discriminative motifs and ranking the top *n* discriminative motifs (i.e., *n_disc_motifs*), (4) representing a patient by the (sparse) feature vector encoding the per-patient frequencies of these highest ranked discriminative motifs. We used the RandomForest binary classification model with default parameters because of its simplicity, efficient and fast execution, and being suitable for interpretability. From the aggregated patient classification probabilities, we computed the receiver operating characteristic curve (ROC) and calculated the corresponding area under the curve (AUC) score. We set the number of features (*n_disc_motifs*) to *30* in all classification tasks throughout this manuscript because it provided a nice balance between stable performance and rich representation. By stable performance, we refer to a representation that was not susceptible to fluctuations in the AUC scores as a function of the discrimination stringency parameter that typically occurs when using small number of features. By rich representation, we refer to a sufficient number of discriminative motifs for high discriminative performance along with a manageable number of discriminative motifs for downstream evaluation and interpretation.

Bootstrap validation of the machine learning performance

To assess if the prediction results and the selected features are significant and not overfitted to the data, we conduct a permutation test by permutating the patient's disease states, i.e., their classification labels. We executed the complete evaluation pipeline and measured the ROC-AUC score for each permutation. If there are zero discriminative motifs in at least one of the iterations, we consider that permutation trial a failure and exclude it from the results. This permutation statistical test’s p-value was determined as the ratio between the number of permutations that resulted with AUC scores higher than the observed labels, and the total number of permutation trials.

Explicit pairwise interactions disease signature

We measure the probability of an edge connecting two cell types across patients for each disease state. First, we created a pairwise cell-type interactions matrix with the probability of an edge connecting to two cell types for each field of view (FOV) from a patient at the given disease state:

(Equation 1) $FOV_l(i,j) = \frac{\sum count(i,j)}{\sum_{e \in E} count(e)}$

Where l is a field of view and i, j are cell types. Then, we summed the overall frequencies across the field of views and normalize:

(Equation 2) $M(i,j) = \frac{\sum_{l \in FOV} FOV_l(i,j)}{\sum_{a,b \in Cell\,Type\,Pair} \sum_{l \in FOV} FOV_l(a,b)}$

Where l is a field of view and $a,\ b,\ i,\ j$ are cell types.

Evaluating Machine learning evaluation of pairwise cell-cell interactions

We used machine learning to evaluate the discriminative capacity of pairwise interactions. We represented a patient with M (Equation 2) and followed the Random Forest leave-one-out-cross-validation. From the aggregated patient classification probabilities, we computed the receiver operating characteristic curve (ROC) and calculated the corresponding area under the curve (AUC) score.

Measuring motifs-induced pairwise interactions disease signature

The discriminative motif-based pairwise interactions were derived from the pool of discriminative motifs. For a given disease state we pooled all the discriminative motif instances across patients’ field of views (FOVs) from that disease state and calculated the motifs-induced pairwise interactions disease signature:

(Equation 3) $InteractionMatrix(i,j) = \frac{\sum_{m \in DM:G=(V,E)} \sum_{(i,j) \in E(m)} w_m}{\sum_{m \in DM:G=(V,E)} \sum_{\forall e \in E(m)} w_m}$

Where i and j are cell types, m is a discriminative motif, DM is the set of all discriminative motifs derived from all patients of a given disease state, and w_m is the mean motif frequency across patients.

Measuring the contribution of the motif's spatial organization to disease state prediction. To measure the contribution of the motif structure compared to only considering the cell type composition, we replaced each discriminative motif with its corresponding cell type composition vector and used machine learning to evaluate the derived cell type composition representation in respect to the motifs representation. Next, we incorporated motif information back to the cell type composition representation, one motif at a time, to evaluate the residual contribution of each motif to the cell type composition. More specifically, the cell type composition vector derived from a motif was represented as a vector of a fixed length according to the number of cell types, where each entry holds the number of instances of the corresponding cell type in the motif. For example, cell type composition I in Fig. 2.4C (green column) is composed of a B-cell, a HEVs cell, and two Memory CD4 T-cells. Note that different motifs can be mapped to the same cell type composition. For instance, two motifs with different inner structures that comprised of 2 * x, 1 * y, and 2 * z cell types are mapped to the same cell type composition vector of (2, 1, 0, 2), given cell types (x, y, t, z). Thus, the evaluation was performed as follows. First, we replaced all discriminative motifs with their corresponding cell type composition vectors and measured the AUC of the cell type composition representation using Random Forest leave-one-patient-out as the baseline. Note that each cell type composition can correspond to multiple motifs, where some of these motifs do not meet the strict discrimination criterion used to define the discriminative motifs. Second, starting from this cell type composition representation, we introduced back the spatial information of one cell type composition by replacing the cell type composition feature with its corresponding discriminative motifs. This replacement induced a hybrid representation that contains both cell type composition and discriminative motif features. This representation was used for machine learning assessment, where the classification gain with respect to the cell type composition baseline was attributed to the contribution of the corresponding motifs' spatial organization. This process was iteratively repeated for each cell type composition, that were then ranked according to the contribution of the corresponding motifs' spatial organization. The difference between the residual gain and the baseline score captures the contribution of the specific set of discriminative motifs for prediction compared to the generalization of the cell type composition.

Machine learning evaluation of the discriminative cell type composition representation

To evaluate the motifs cell type composition information without the specific inner structure, we repeated the steps of context-dependent motifs' selection and machine learning analysis, but instead of using the discriminative motifs, we used the discriminative cell type composition representations, i.e., cell type compositions that sufficiently appear in patients of one physiological context and do not appear at all in patients of the other physiological context. Each patient is represented by the (sparse) vector of its cell type composition frequencies. For instance, if *n* motifs are matched to a single cell type composition, the frequency is the sum of *n* motifs count with respect to the total subgraph in patient samples. The cell type composition representation is less specific than the motif representation and, therefore, expects to generate a smaller number of discriminate cell type compositions.

Evaluation with graph neural network (GNN) model

We performed a whole graph classification to predict the disease state using a three-layer graph convolutional network (GCN) (Kipf & Welling, 2016). The spatial multicellular network defines the input for the GCN where the attribute of each node was its corresponding cell type. We aggregated the information across nodes after the final layer, using global max pooling, to a single disease state prediction. The model was optimized with the Adam optimizer (Kingma & Ba, 2014) and using the cross-entropy loss function:

(Equation 4) $L(y, \hat{y}) = -\sum_{c=1}^{M} y_{i,c} \log(\hat{y}_{i,c})$.

We performed leave-one-patient-out cross-validation, as described above.

Supplementary Figures

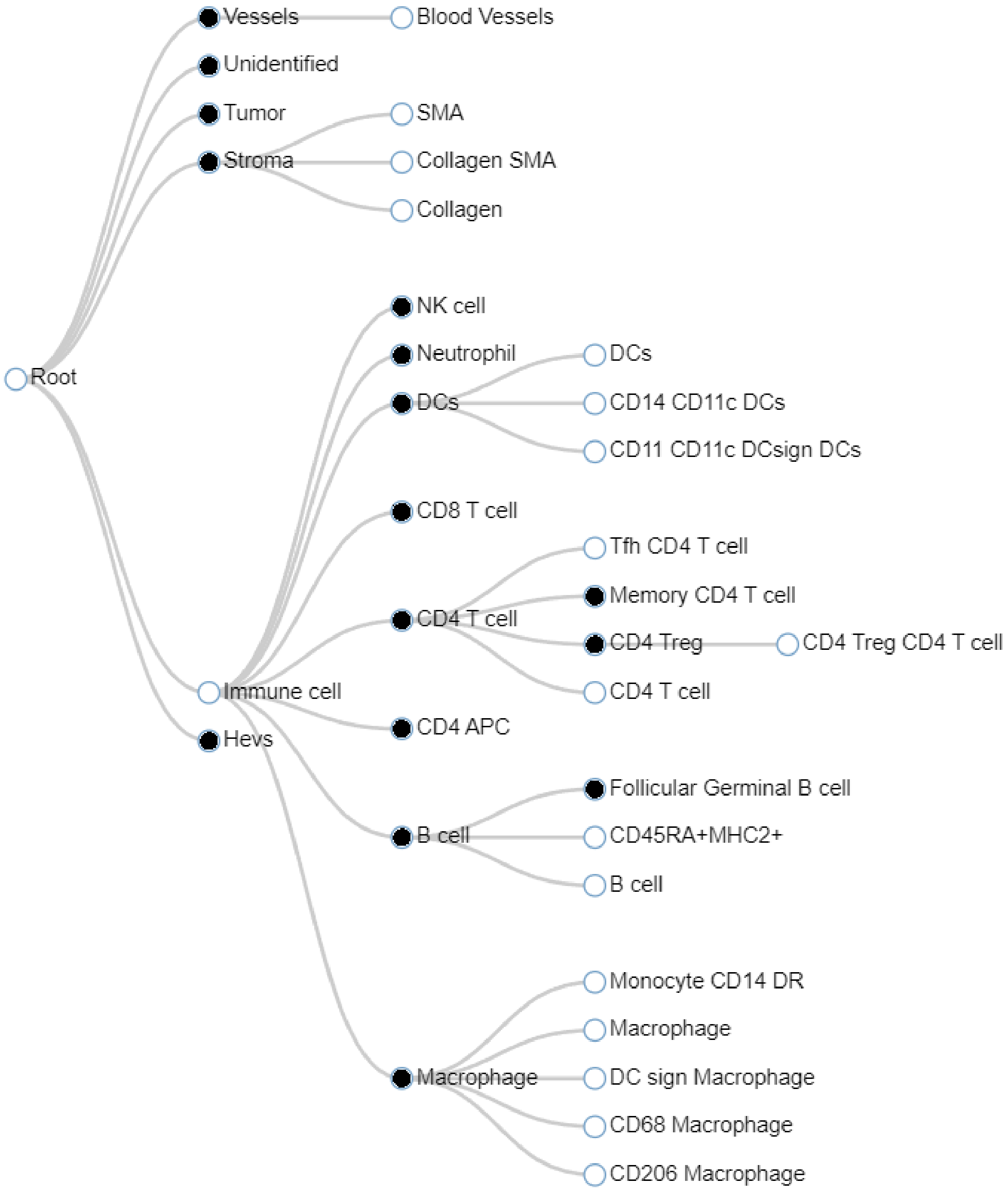

Figure S2.1. Melanoma cell type hierarchy. The hierarchy tree's leafs (n=26) are the full-resolution cell types. Full nodes (n = 16) represent the cell types used in this study as input to CISM.

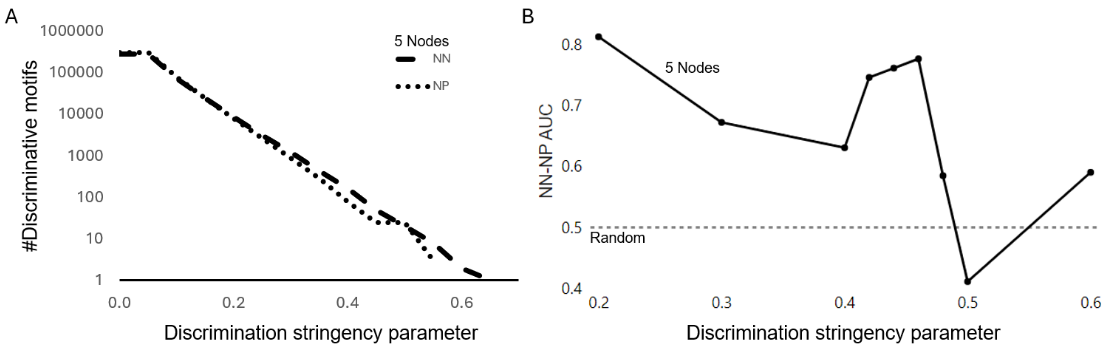

Figure S2.2. CISM analysis of NN versus NP with 5-node motifs. (**A**) The number of 5-cell discriminative motifs (y-axis, log scale) over the discrimination stringency parameter (x-axis). (**B**) Machine learning validation of melanoma disease state discrimination with CISM's discriminative motifs representation. Leave one out cross-validation (LOOCV) model performance (AUC) (y-axis) over the discrimination stringency parameter (x-axis).

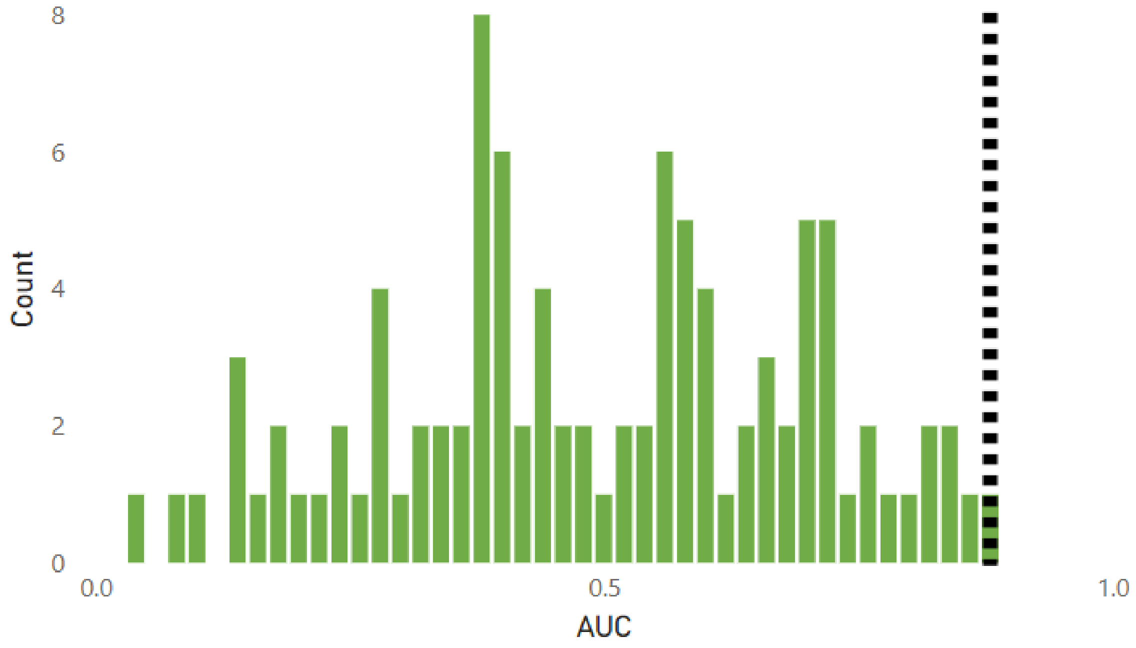

Figure S2.3. Patient disease state permutation test in the context of NN versus NP. The green bars are the AUC result of n=100 random samples (3 were exceeded with zero discriminative features) with a bin size 0.05 and p-value of 0.01. The dashed black line is the control AUC result of 0.88.

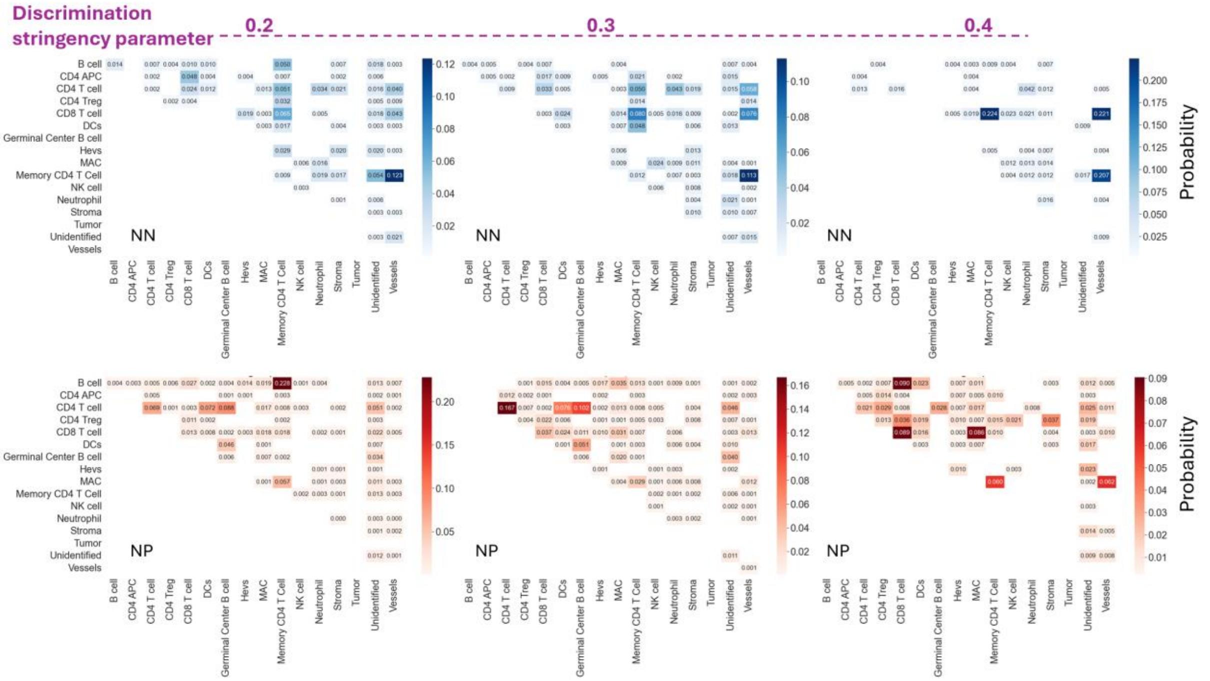

Figure S2.4. Stability of discriminative motifs cell-cell signature. The probability of two cell types to be connected with an edge in the pooled set of instances of discriminative motifs associated with negative patients (1st row) and positive (2nd row) for the four nodes and [0.2, 0.3, 0.4] fraction-of-patients parameter. The number of motifs in NN and NP by order (0.2: 56, 0.3: 49, 0.4: 16), (0.2: 100, 0.3: 84, 0.4: 34). The Spearman correlation across consecutive thresholds has a higher correlation than with between disease state: The correlation between consecutive thresholds - NN[0.2]-NN[0.3]: corr = 0.6560, p-value ≤ 0.0001; NN[0.3]-NN[0.4]: corr = 0.4485, p-value ≤ 0.0001; NP[0.2]-NP[0.3]: corr = 0.7167, p-value ≤ 0.0001; NP[0.3]-NP[0.4]: corr = 0.4295, p-value ≤ 0.0001; The correlation between disease state - NN[0.2]-NP[0.2]: corr = 0.3696, p-value ≤ 0.0001; NN[0.3]-NP[0.3]: corr = 0.1711, p-value ≤ 0.0657; NN[0.4]-NP[0.4]: corr = 0.0151, p-value ≤ 0.86989

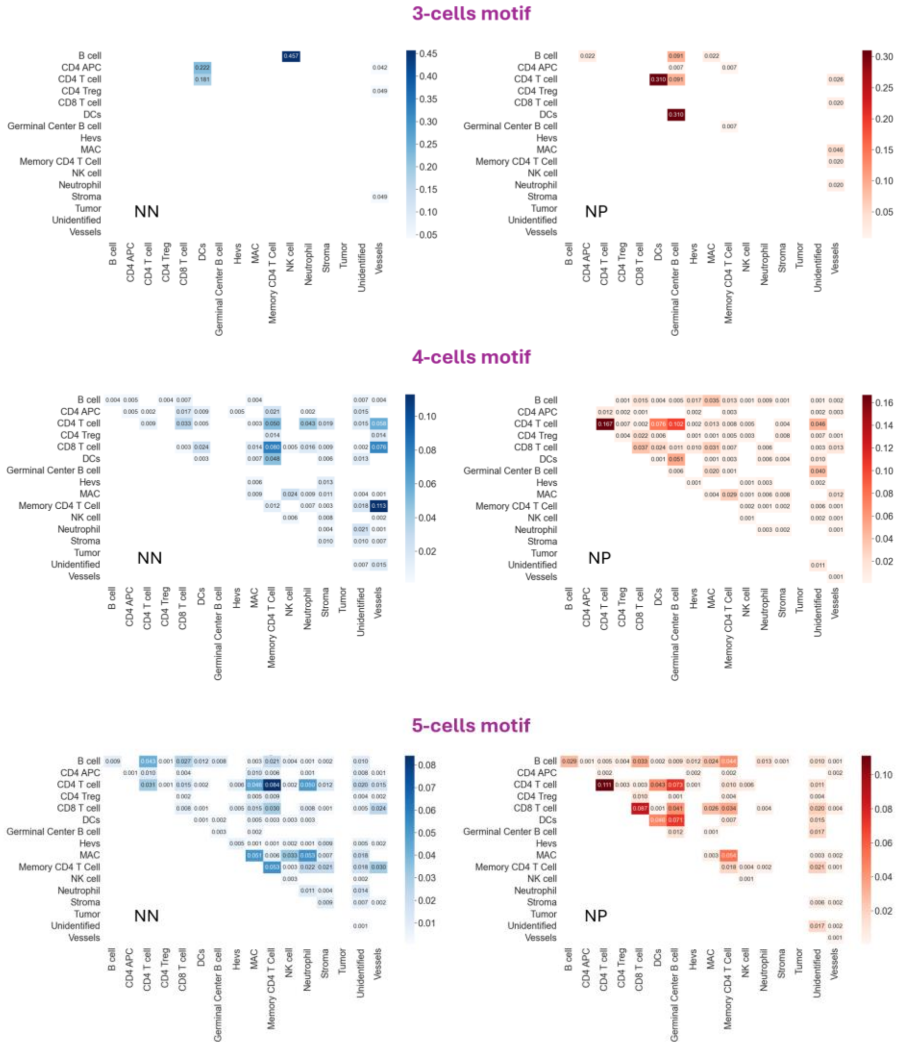

Figure S2.5. Stability of discriminative motif-induced pairwise interactions disease signature. The probability of two cell types to be connected with an edge in the pooled set of instances of discriminative motifs associated with negative patients (1st column) and positive (2nd column) for the 3-, 4-, 5- cells for the maximum common 0.3 discrimination stringency parameter. The number of motifs in NN and NP by order (3-cells: 4, 4-cells: 49, 5-cells: 137), (3-cell: 7, 4-cell: 84, 5-cell: 102). The Spearman correlation across consecutive motif size has a higher correlation than between disease state: The correlation between consecutive motif size - for NN: [3-cells]-[4-cells]: corr = 0.0808, p-value = 0.38; [4-cells]-[5-cells]: corr = 0.5346, p-value ≤ 0.0001; for NP: [3-cells]-[4-cells]: corr = 0.1960, p-value ≤ 0.0319; [4-cells]-[5-cells]: corr = 0.6434, p-value ≤ 0.0001; The correlation between disease state – for NN versus NP 3-cells: corr = 0.0485, p-value ≤ 0.5982; 4-cells: corr = 0.1711, p-value ≤ 0.0616; 5-cells: corr = 0.3503, p-value ≤ 0.0001.

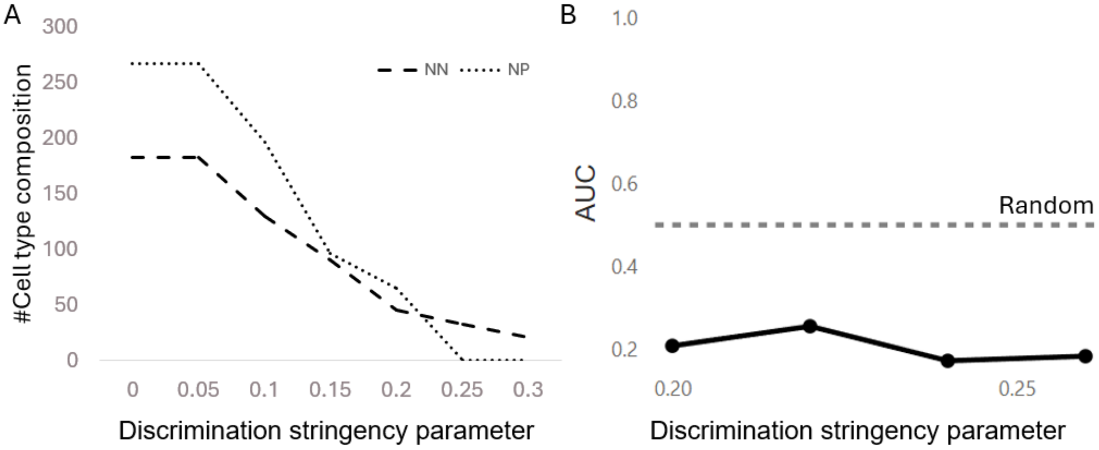

Figure S2.6. Model performance with cell type composition as discriminator. (A) Number of discriminative cell type composition across a fraction of patients. (B) Classification results between NN and NP using cell type composition across a fraction of patients.

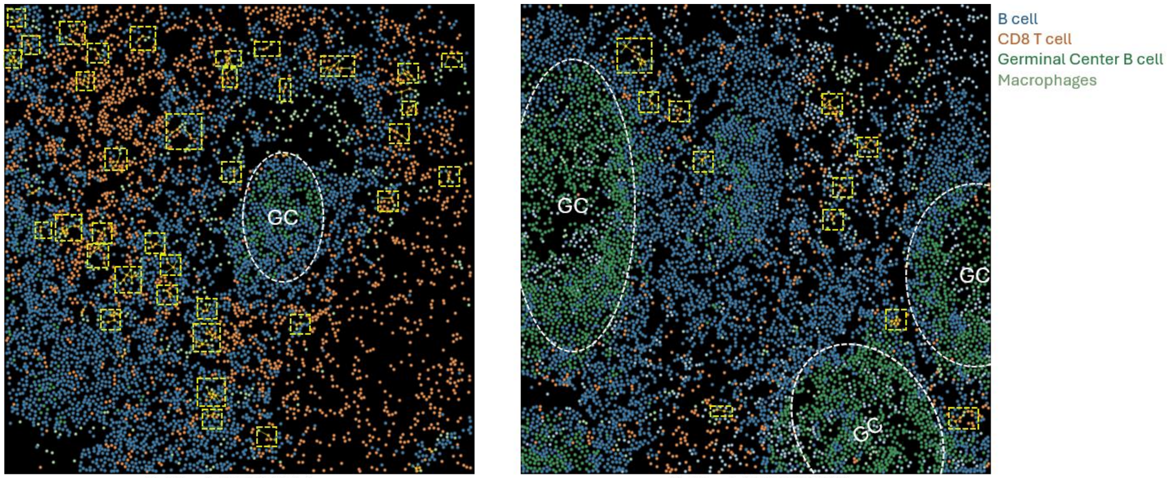

Patient 9 FOV114

Patient 13 FOV130

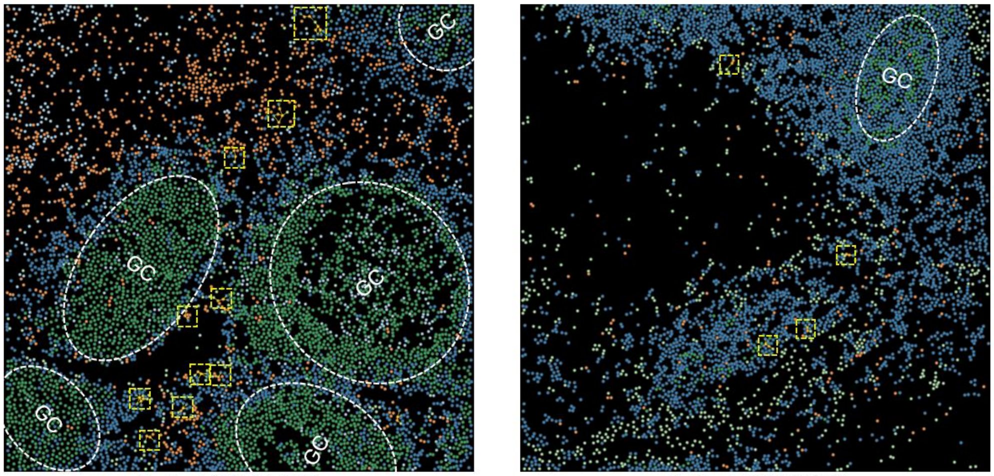

Patient 12 FOV123

Patient 23 FOV238

Figure S2.7. Additional patient tissue section with Motif III instances around the GC. Localizing motif III (Fig. 5B) in the tissue of NP patients #9 (top left), #13 (top right), #12 (bottom left), and #23 (bottom right). Each dot represents a cell colored according to its cell type: B cell, CD8 T cell, Germinal Center B cells, and macrophages (other cell types are not shown). The germinal center (GC) is surrounded by a dashed white circle. Instances of motif III are marked with dashed yellow rectangles (larger rectangles indicate multiple instances of the motif).

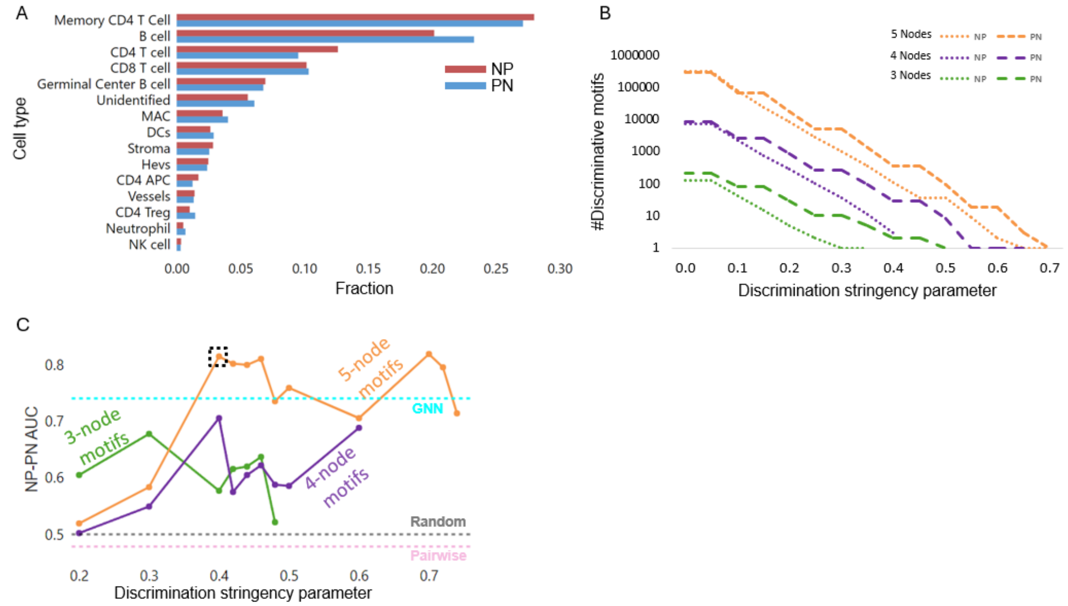

Figure S2.8. Context-dependent identification of spatial motifs (CISM) classification prediction between PN and NP disease state (**A**) Cell type distribution for PN and NP patient groups. (**B**) The number of 3-cell (green), 4-cell (purple), and 5-cell (orange) context-dependent discriminative motifs (y-axis, log scale) over the discrimination stringency parameter (x-axis) - a fraction of patients of a given clinical outcome that share a discriminating motif when none of the patients with the other clinical outcome share it. (**C**) Machine learning validation of melanoma disease state discrimination with CISM's discriminative motifs representation. Leave one patient out cross-validation (LOOCV) model performance (AUC) (y-axis) over the discrimination stringency parameter (x-axis) (green - 3-cell motifs, purple- 4-cell motifs, orange- 5-cell motifs). The pink, cyan, and black dashed horizontal lines represent the LOOCV AUC score of pairwise, GNN, and a random null model, correspondingly. The discriminative motifs derived from 5-cell motifs with the discrimination stringency parameter of 0.4 for discriminative motifs selection were used for further analysis.

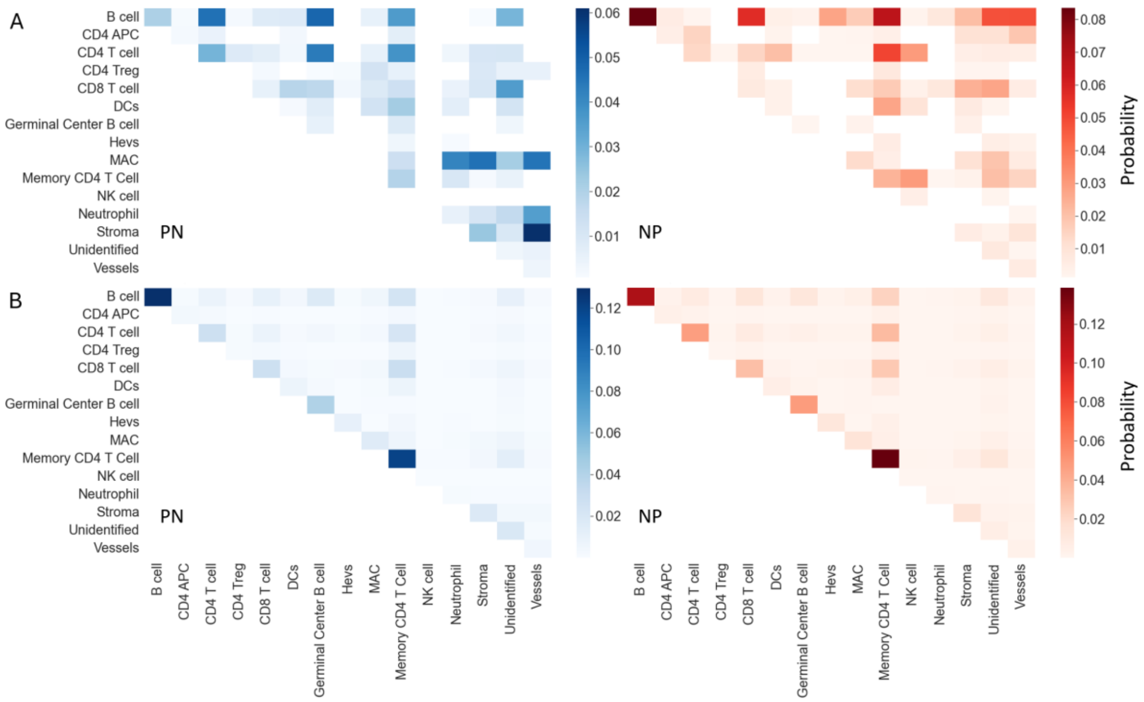

Figure S2.9. Motifs-induced pairwise interactions disease signature in the context of PN versus NP. (**A**) The distribution of motifs-induced pairwise interactions disease signature. The probability of two cell types to be connected with an edge in the cohorts' patients pooled set of instances of discriminative motifs associated with NN patients (left, n = 120 motifs) and NP patients (right, n = 90 motifs). (**B**) The distribution of pairwise interactions disease signature. The probability of two cell types to be connected with an edge in the cohorts' patients pooled set of multicellular networks.

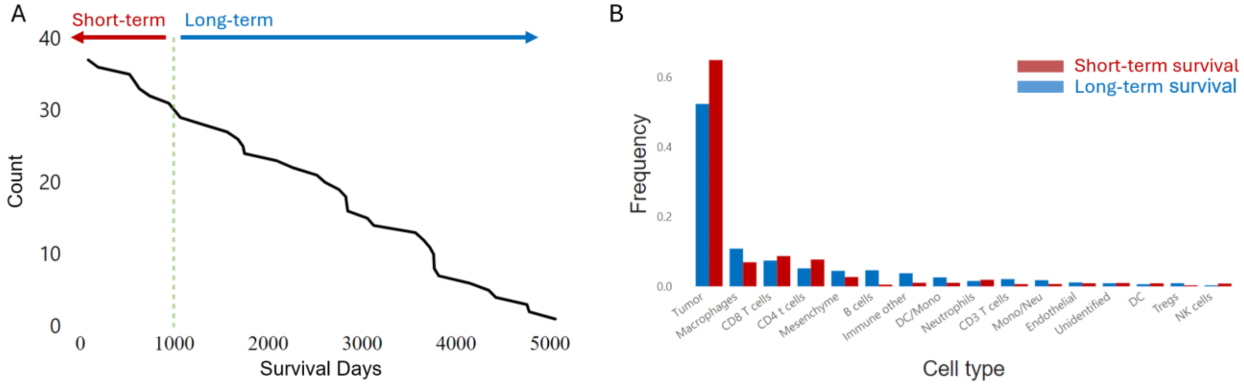

Figure S2.10. TNBC cohort. (**A**) Number of patients who survived over time in days. The green dashed line is the cutoff between aggressive (n=7) and non-aggressive (n=30) disease. (**B**) Cell type distribution for Positive and Negative patient groups.

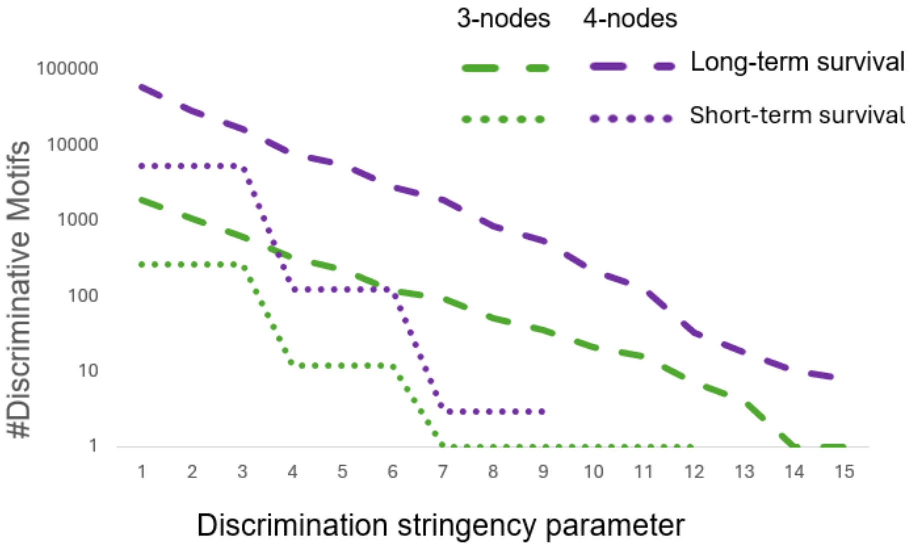

Figure S2.11. Number of discriminative motifs in TNBC. The number of 3-cell (green), 4-cell (purple) context-dependent discriminative motifs (y-axis, log scale) over the discrimination stringency parameter (x-axis) - a fraction of patients of a given clinical outcome that share a discriminating motif when none of the patients with the other clinical outcome share it.

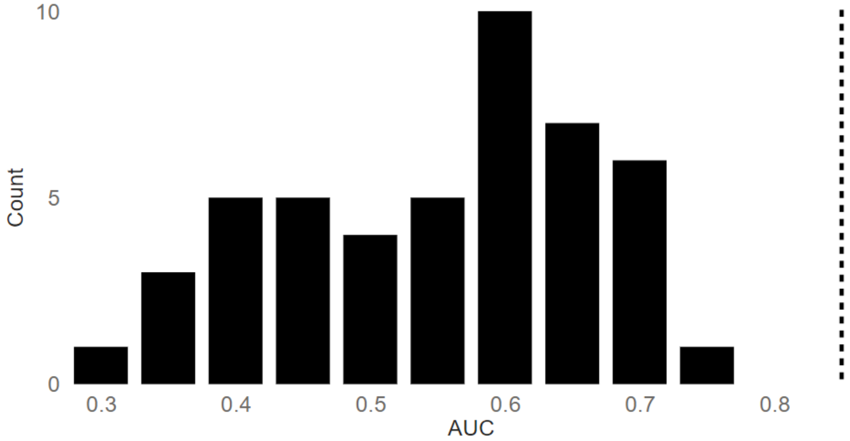

Figure S2.12. TNBC patient disease state permutation test. The green bars are the AUC result of n=100 random samples (53 were exceeded with zero discriminative features) with a bin size 0.05 and p-value < 0.01. The dashed black line is the control AUC result of 0.85.

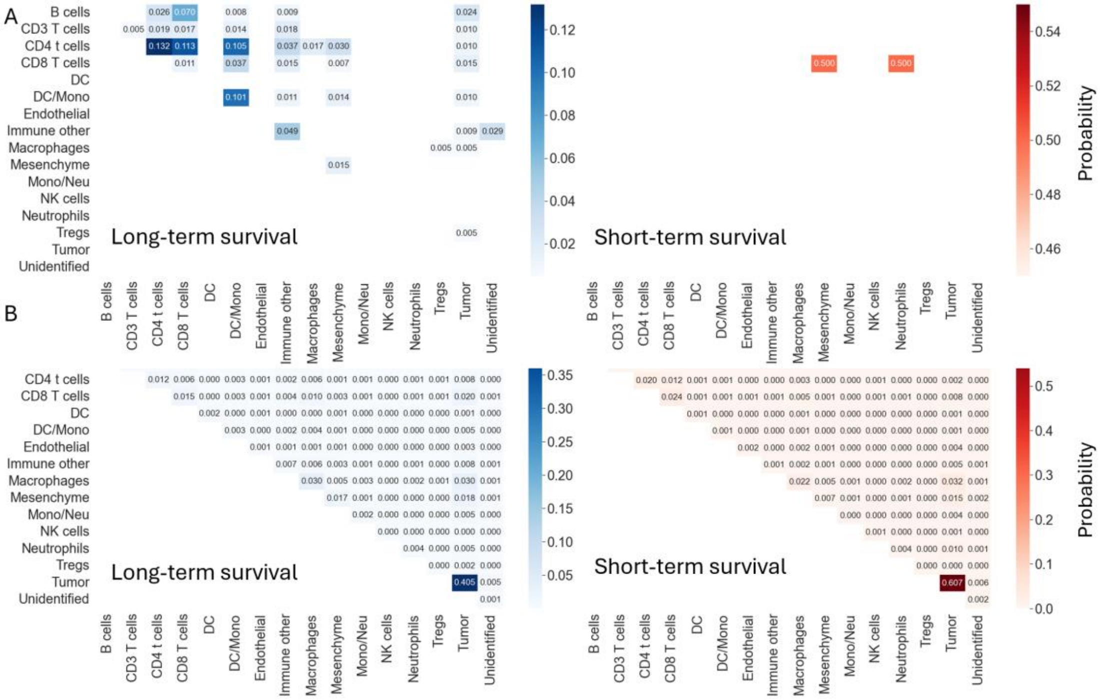

Figure S2.13. TNBC discriminative motifs-induced pairwise interactions. (**A**) The distribution of motifs-induced pairwise interactions disease signature. The probability of two cell types to be connected with an edge in the cohorts' patients pooled set of instances of discriminative motifs associated with long-term survival patients (left**,** n = 31 motifs) and short-term survival patients (right**,** n = 1 motif). Explicitly enumerating the distribution of pairwise interaction for long-term survival versus short-term survival patients according to the probability of two cell types being connected with an edge in the multicellular network did not show a clear distinction in the context of disease state. (**B**) The distribution of pairwise interactions disease signature. The probability of two cell types to be connected with an edge in the cohorts' patients pooled set of multicellular networks..

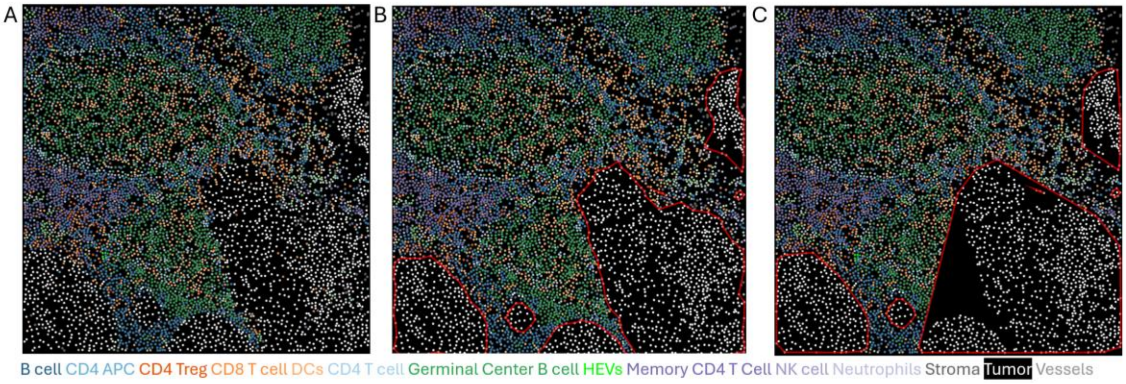

Figure S2.14. Excluding tumor clusters to analyze the lymph node tumor microenvironment. An example of the tissue's derived alpha shape for different α values. (**A**) Lymph node tissue section of patient #86 FOV #156, which includes tumor cells. (**B-C**) alpha shape clusters (red polygons) for α = 0.01 (B) versus α = 0 (Convex Hull) (C). Only tumor cells are shown inside the alpha clusters to emphasize non-tumor cell exclusion.

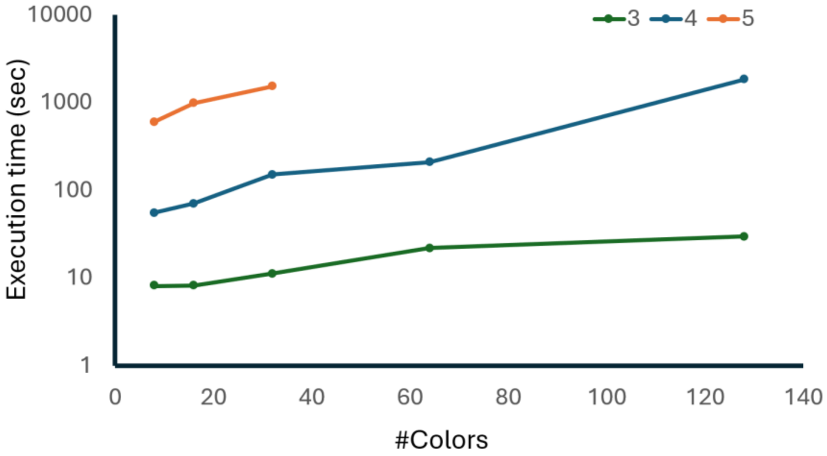

Figure S2.15. FANMOD+ benchmark for 3,4,5 nodes motif size. FANMOD+ benchmarking. A benchmark test for the execution time (y-axis in log scale) of FANMOD+ with respect to the number of node colors (x-axis) and motif size (3-nodes in green, 4-nodes in blue, and 5-nodes in orange). Each data point was calculated according to the mean execution time of five random planar graphs with n = 10,000 nodes, e ~ 30,000 edges and 8-128 colors (Methods). The calculated significance of each motif in the network (p-value) was based on a random factor of 100 random networks.

Final Remarks

In this dissertation, I have explored the fundamental question of how cellular heterogeneity and noisy interactions between individual cells converge to regulate the emergence of tissue-scale architecture and function. Biological systems function at various spatial and temporal levels, where the precise coordination of cellular processes leads to the formation of healthy tissues. In contrast, dysfunction in these processes contributes to disease. However, the complex interplay between individual cells and their collective behavior at the tissue level remains a challenge to fully understand.

The work presented here provides new insights into the intricate relationship between single-cell interactions and the emergent properties of tissues. In the first chapter, I introduced a novel approach to quantitatively assess the dynamics of multicellular synchronization at the single-cell level. By leveraging data-driven methodologies and tools from information theory, we identified how increased connectivity and heterogeneity among cells contribute to the global synchronization of a multicellular network. This finding underscores the importance of local interactions and information flow in stabilizing tissue self-organization.

In the second chapter, I presented the Context-dependent Identification of Spatial Motifs (CISM) method, which offers a new way of characterizing tissue disease states through the identification of recurrent patterns of cell types' spatial organization. By applying this method to proteomics imaging datasets from melanoma and triple-negative breast cancer (TNBC), we demonstrated its ability to predict disease states and reveal differences in immune cell organization between tissues. The CISM method, with its focus on modular components at the spatial scale of a few cells, opens the door to new avenues for hypothesis generation and explanatory modeling in tissue biology.

Together, these studies highlight the importance of bottom-up approaches for bridging the scales of biological organization—from individual cells to complex multicellular structures. By focusing on the dynamics of single-cell interactions and the modular components of tissue organization, this work advances our understanding of how collective cellular behavior emerges to maintain tissue function. The methods and findings presented here not only contribute to the basic understanding of multicellular systems but also hold promise for informing future research on tissue development, regeneration, and disease.

References

Aihara Courtney L.; Korman Abraham; Perry Nicholas P.J.; Prasad Vikram; Shull Gary E.; Montrose Marshall H., E. H. (2013). In Vivo Epithelial Wound Repair Requires Mobilization of Endogenous Intracellular and Extracellular Calcium. *The Journal of Biological Chemistry*, *288*(47), 33585–33597. https://doi.org/10.1074/jbc.m113.488098

Akaike, H. (1970). Statistical predictor identification. *Annals of the Institute of Statistical Mathematics*, *22*(1), 203–217. https://doi.org/10.1007/BF02506337

Akaike, H. (1973). Maximum likelihood identification of Gaussian autoregressive moving average models. *Biometrika*, *60*(2), 255–265.

Albuquerque Christopher M.; Savla Ushma; Schnaper H. William; Flozak Annette S., M. L. C. ; W. (2000). Shear stress enhances human endothelial cell wound closure in vitro. *American Journal of Physiology. Heart and Circulatory Physiology*, *279*(1), H293-302. https://doi.org/10.1152/ajpheart.2000.279.1.h293

Ali, M., Kuijs, M., Hediyeh-Zadeh, S., Treis, T., Hrovatin, K., Palla, G., Schaar, A. C., & Theis, F. J. (2024). GraphCompass: spatial metrics for differential analyses of cell organization across conditions. *Bioinformatics (Oxford, England)*, *40*(Suppl 1), i548–i557. https://doi.org/10.1093/BIOINFORMATICS/BTAE242

Alon, U. (2007). Network motifs: theory and experimental approaches. *Nature Reviews. Genetics*, *8*(6), 450–461. https://doi.org/10.1038/NRG2102

Amaral Antonio; Barthelemy Marc; Stanley H. E., L. A. N. S. (2000). Classes of small-world networks. *Proceedings of the National Academy of Sciences of the United States of America*, *97*(21), 11149–11152. https://doi.org/10.1073/pnas.200327197

Amitay, Y., Bussi, Y., Feinstein, B., Bagon, S., Milo, I., & Keren, L. (2023). CellSighter: a neural network to classify cells in highly multiplexed images. *Nature Communications*, *14*(1). https://doi.org/10.1038/S41467-023-40066-7

Bannon, D., Moen, E., Schwartz, M., Borba, E., Kudo, T., Greenwald, N., Vijayakumar, V., Chang, B., Pao, E., Osterman, E., Graf, W., & Van Valen, D. (2021a). DeepCell Kiosk:

scaling deep learning-enabled cellular image analysis with Kubernetes. *Nature Methods*, *18*(1), 43–45. https://doi.org/10.1038/S41592-020-01023-0

Bannon, D., Moen, E., Schwartz, M., Borba, E., Kudo, T., Greenwald, N., Vijayakumar, V., Chang, B., Pao, E., Osterman, E., Graf, W., & Van Valen, D. (2021b). Publisher Correction: DeepCell Kiosk: scaling deep learning-enabled cellular image analysis with Kubernetes. *Nature Methods*, *18*(2), 219. https://doi.org/10.1038/S41592-021-01059-W

Barrett Lionel; Seth Anil K., A. B. ; B. (2010). Multivariate Granger causality and generalized variance. *Physical Review. E, Statistical, Nonlinear, and Soft Matter Physics*, *81*(4), 41907. https://doi.org/10.1103/physreve.81.041907

Bintu John; Antebi Yaron E.; McCue Kayla; Kazuki Yasuhiro; Uno Narumi; Oshimura Mitsuo; Elowitz Michael B., L. Y. (2016). Dynamics of epigenetic regulation at the single-cell level. *Science (New York, N.Y.)*, *351*(6274), 720–724. https://doi.org/10.1126/science.aab2956

Bonferroni, C. (1936). Teoria statistica delle classi e calcolo delle probabilita. *Pubblicazioni Del R Istituto Superiore Di Scienze Economiche e Commericiali Di Firenze*, *8*, 3–62.

Brangwynne Gijsje H.; MacKintosh Fred C.; Weitz David A., C. P. ; K. (2009). Intracellular transport by active diffusion. *Trends in Cell Biology*, *19*(9), 423–427. https://doi.org/10.1016/j.tcb.2009.04.004

Calderón Mauricio A., J. F. ; R. (2016). Regulation of Connexins Expression Levels by MicroRNAs, an Update. *Frontiers in Physiology*, *7*(NA), 558. https://doi.org/10.3389/fphys.2016.00558

Charbonier, F. W., Zamani, M., & Huang, N. F. (2019). Endothelial Cell Mechanotransduction in the Dynamic Vascular Environment. *Advanced Biosystems*, *3*(2), 1800252-NA. https://doi.org/10.1002/adbi.201800252

Cheng Brooks; Ourthiague Diana R.; Hoffmann Alexander, Z. T. (2015). Distinct single-cell signaling characteristics are conferred by the MyD88 and TRIF pathways during TLR4 activation. *Science Signaling*, *8*(385), ra69-NA. https://doi.org/10.1126/scisignal.aaa5208

Cheung, Y.-W., & Lai, K. S. (1995). Lag Order and Critical Values of the Augmented Dickey–Fuller Test. *Journal of Business & Economic Statistics*, *13*(3), 277–280. https://doi.org/10.1080/07350015.1995.10524601

Davies, P. F. (2008). Hemodynamic shear stress and the endothelium in cardiovascular pathophysiology. *Nature Clinical Practice. Cardiovascular Medicine*, *6*(1), 16–26. https://doi.org/10.1038/ncpcardio1397

Dayao, M. T., Trevino, A., Kim, H., Ruffalo, M., D'angio, H. B., Preska, R., Duvvuri, U., Mayer, A. T., & Bar-Joseph, Z. (2023a). Deriving spatial features from in situ proteomics imaging to enhance cancer survival analysis. *Bioinformatics (Oxford, England)*, *39*(39 Suppl 1), I140–I148. https://doi.org/10.1093/BIOINFORMATICS/BTAD245

Dayao, M. T., Trevino, A., Kim, H., Ruffalo, M., D'angio, H. B., Preska, R., Duvvuri, U., Mayer, A. T., & Bar-Joseph, Z. (2023b). Deriving spatial features from in situ proteomics imaging to enhance cancer survival analysis. *Bioinformatics (Oxford, England)*, *39*(39 Suppl 1), I140–I148. https://doi.org/10.1093/BIOINFORMATICS/BTAD245

De la Fuente Carlos; Malaina Iker; Fedetz María; Carrasco-Pujante Jose; Morales Miguel; Knafo Shira; Martínez Luis; Pérez-Samartín Alberto; López José I.; Pérez-Yarza Gorka; Boyano María Dolores, I. M. ; B. (2019). Evidence of conditioned behavior in amoebae. *Nature Communications*, *10*(1), 3690. https://doi.org/10.1038/s41467-019-11677-w

Dieterle Jiseon; Irimia Daniel; Amir Ariel, P. B. ; M. (2020). Dynamics of diffusive cell signaling relays. *ELife*, *9*(NA), NA-NA. https://doi.org/10.7554/elife.61771

Elowitz Arnold J.; Siggia Eric D.; Swain Peter S., M. B. ; L. (2002). Stochastic Gene Expression in a Single Cell. *Science (New York, N.Y.)*, *297*(5584), 1183–1186. https://doi.org/10.1126/science.1070919

Eming Paul; Tomic-Canic Marjana, S. A. ; M. (2014). Wound repair and regeneration: Mechanisms, signaling, and translation. *Science Translational Medicine*, *6*(265), 265sr6-NA. https://doi.org/10.1126/scitranslmed.3009337

Estrada, E. (2010). Quantifying network heterogeneity. *Physical Review. E, Statistical, Nonlinear, and Soft Matter Physics*, *82*(6), 066102-NA. https://doi.org/10.1103/physreve.82.066102

Faehling Jens; FöHr Karl J.; Fellbrich Guido; Mayr Ulrike; Trischler Gerlinde; Waltenberger Johannes, M. K. (2002). Essential role of calcium in vascular endothelial growth factor A-induced signaling: mechanism of the antiangiogenic effect of carboxyamidotriazole. *The FASEB Journal*, *16*(13), 1–29. https://doi.org/10.1096/fj.01-0938fje

Fancher, S., & Mugler, A. (2017). Fundamental Limits to Collective Concentration Sensing in Cell Populations. *Physical Review Letters*, *118*(7), 078101. https://doi.org/10.1103/PhysRevLett.118.078101

Fujii Shohei; Morita Mitsuhiro, Y. M. (2017). Astrocyte calcium waves propagate proximally by gap junction and distally by extracellular diffusion of ATP released from volume-regulated anion channels. *Scientific Reports*, *7*(1), 13115. https://doi.org/10.1038/s41598-017-13243-0

Goglia Maxwell Z.; Jena Siddhartha G.; Silbert Jillian; Basta Lena P.; Devenport Danelle; Toettcher Jared E., A. G. ; W. (2020). A Live-Cell Screen for Altered Erk Dynamics Reveals Principles of Proliferative Control. *Cell Systems*, *10*(3), 240-253.e6. https://doi.org/10.1016/j.cels.2020.02.005

Granger, C. W. J. (1969). Investigating Causal Relations by Econometric Models and Cross-Spectral Methods. *Econometrica*, *37*(3), 424–438. https://doi.org/10.2307/1912791

Greenwald, N. F., Miller, G., Moen, E., Kong, A., Kagel, A., Dougherty, T., Fullaway, C. C., McIntosh, B. J., Leow, K. X., Schwartz, M. S., Pavelchek, C., Cui, S., Camplisson, I., Bar-Tal, O., Singh, J., Fong, M., Chaudhry, G., Abraham, Z., Moseley, J., … Van Valen, D. (2022). Whole-cell segmentation of tissue images with human-level performance using large-scale data annotation and deep learning. *Nature Biotechnology*, *40*(4), 555–565. https://doi.org/10.1038/S41587-021-01094-0

Gregor Koichi; Masaki Noritaka; Sawai Satoshi, T. F. (2010). The Onset of Collective Behavior in Social Amoebae. *Science (New York, N.Y.)*, *328*(5981), 1021–1025. https://doi.org/10.1126/science.1183415

Griss, J., Bauer, W., Wagner, C., Simon, M., Chen, M., Grabmeier-Pfistershammer, K., Maurer-Granofszky, M., Roka, F., Penz, T., Bock, C., Zhang, G., Herlyn, M., Glatz, K., Läubli, H., Mertz, K. D., Petzelbauer, P., Wiesner, T., Hartl, M., Pickl, W. F., … Wagner, S. N. (2019). B cells sustain inflammation and predict response to immune checkpoint blockade in human melanoma. *Nature Communications*, *10*(1). https://doi.org/10.1038/S41467-019-12160-2

Gut Markus D.; Pelkmans Lucas, G. H. (2018). Multiplexed protein maps link subcellular organization to cellular states. *Science (New York, N.Y.)*, *361*(6401), NA-NA. https://doi.org/10.1126/science.aar7042

Gut Michelle D.; Pe'er Dana; Pelkmans Lucas; Liberali Prisca, G. T. (2015). Trajectories of cell-cycle progression from fixed cell populations. *Nature Methods*, *12*(10), 951–954. https://doi.org/10.1038/nmeth.3545

Gutman Boris; Katanic Vladimir, I. F. (2018). Randić index and information. *AKCE International Journal of Graphs and Combinatorics*, *15*(3), 307–312. https://doi.org/10.1016/j.akcej.2017.09.006

Hampel, F. R. (1974). The Influence Curve and Its Role in Robust Estimation. *Journal of the American Statistical Association*, *69*(346), 383–393. https://doi.org/10.1080/01621459.1974.10482962

Handly Roy, L. N. W. (2017). Wound-induced Ca2+ wave propagates through a simple release and diffusion mechanism. *Molecular Biology of the Cell*, *28*(11), 1457–1466. https://doi.org/10.1091/mbc.e16-10-0695

Hannan, E. J., & Quinn, B. G. (1979). The determination of the order of an autoregression. *Journal of the Royal Statistical Society: Series B (Methodological)*, *41*(2), 190–195.

Hasenauer Steffen; Doszczak Malgorzata; Radde Nicole; Scheurich Peter; Allgöwer Frank, J. W. (2011). Identification of models of heterogeneous cell populations from population snapshot data. *BMC Bioinformatics*, *12*(1), 125. https://doi.org/10.1186/1471-2105-12-125

Hill Monica L.; Lenertz Lisa Y.; Bertics Paul J., L. M. ; G. (2010). Extracellular ATP May Contribute to Tissue Repair by Rapidly Stimulating Purinergic Receptor X7-Dependent Vascular Endothelial Growth Factor Release from Primary Human Monocytes. *Journal of Immunology (Baltimore, Md. : 1950)*, *185*(5), 3028–3034. https://doi.org/10.4049/jimmunol.1001298

Ho Rohan J.; Carr Rosalyn L.; Tanentzapf Guy, K. Y. L. ; K. (2021). A gap-junction-mediated, calcium-signaling network controls blood progenitor fate decisions in hematopoiesis. *Current Biology : CB*, *31*(21), 4697-4712.e6. https://doi.org/10.1016/j.cub.2021.08.027

Huang Hongkai; Bhaya Devaki; Grossman Arthur R.; Granier Sébastien; Kobilka Brian K.; Zare Richard N., B. W. (2007). Counting Low-Copy Number Proteins in a Single Cell. *Science (New York, N.Y.)*, *315*(5808), 81–84. https://doi.org/10.1126/science.1133992

Jackson, H. W., Fischer, J. R., Zanotelli, V. R. T., Ali, H. R., Mechera, R., Soysal, S. D., Moch, H., Muenst, S., Varga, Z., Weber, W. P., & Bodenmiller, B. (2020). The single-cell pathology landscape of breast cancer. *Nature*, *578*(7796), 615–620. https://doi.org/10.1038/S41586-019-1876-X

Jacob K. P.; Misra Ranjeev; Ambika G., R. H. (2017). Measure for degree heterogeneity in complex networks and its application to recurrence network analysis. *Royal Society Open Science*, *4*(1), 160757. https://doi.org/10.1098/rsos.160757

Jain Victoire M L; Narayana Gautham Hari Narayana Sankara; de Beco Simon; D'Alessandro Joseph; Cellerin Victor; Chen Tianchi; Heuzé Mélina L; Marcq Philippe; Mège René-Marc; Kabla Alexandre; Lim Chwee Teck; Ladoux Benoit, S. C. (2020). The role of single-cell mechanical behaviour and polarity in driving collective cell migration. *Nature Physics*, *16*(7), 802–809. https://doi.org/10.1038/s41567-020-0875-z

Jones, D. T. (2019). Setting the standards for machine learning in biology. *Nature Reviews. Molecular Cell Biology*, *20*(11), 659–660. https://doi.org/10.1038/S41580-019-0176-5

Keren, L., Bosse, M., Marquez, D., Angoshtari, R., Jain, S., Varma, S., Yang, S. R., Kurian, A., Van Valen, D., West, R., Bendall, S. C., & Angelo, M. (2018). A Structured Tumor-Immune Microenvironment in Triple Negative Breast Cancer Revealed by Multiplexed Ion Beam Imaging. *Cell*, *174*(6), 1373-1387.e19. https://doi.org/10.1016/J.CELL.2018.08.039

Kingma, D. P., & Ba, J. L. (2014). Adam: A Method for Stochastic Optimization. *3rd International Conference on Learning Representations, ICLR 2015 - Conference Track Proceedings*. https://arxiv.org/abs/1412.6980v9

Kipf, T. N., & Welling, M. (2016). Semi-Supervised Classification with Graph Convolutional Networks. *5th International Conference on Learning Representations, ICLR 2017 - Conference Track Proceedings*. https://arxiv.org/abs/1609.02907v4

Kirkpatrick, D. G., & Seidel, R. (1983). On the Shape of a Set of Points in the Plane. *IEEE Transactions on Information Theory*, *29*(4), 551–559. https://doi.org/10.1109/TIT.1983.1056714

Kohn Riccardo; Spoonster Joseph; Wersto Robert P.; Liotta Lance A., E. C. ; A. (1995). Angiogenesis: role of calcium-mediated signal transduction. *Proceedings of the National Academy of Sciences of the United States of America*, *92*(5), 1307–1311. https://doi.org/10.1073/pnas.92.5.1307

Kumar Norton B., N. M. ; G. (1996). The Gap Junction Communication Channel. *Cell*, *84*(3), 381–388. https://doi.org/10.1016/s0092-8674(00)81282-9

Kwiatkowski Peter C.B.; Schmidt Peter; Shin Yongcheol, D. P. (1992). Testing the null hypothesis of stationarity against the alternative of a unit root: How sure are we that economic time series have a unit root? *Journal of Econometrics*, *54*(1–3), 159–178. https://doi.org/10.1016/0304-4076(92)90104-y

Lacar Stephanie Z.; Platel Jean-Claude; Bordey Angélique, B. Y. (2011). Gap junction-mediated calcium waves define communication networks among murine postnatal neural progenitor cells. *The European Journal of Neuroscience*, *34*(12), 1895–1905. https://doi.org/10.1111/j.1460-9568.2011.07901.x

Lee Min Tae; Rhodes Garrett; Sack Kelsey; Son Sung Jun; Rich Celeste B.; Kolachalama Vijaya B.; Gabel Christopher V.; Trinkaus-Randall Vickery, Y. K. (2019). Sustained Ca2+ mobilizations: A quantitative approach to predict their importance in cell-cell communication and wound healing. *PloS One*, *14*(4), e0213422-NA. https://doi.org/10.1371/journal.pone.0213422

Lei, X., Khatri, I., de Wit, T., de Rink, I., Nieuwland, M., Kerkhoven, R., van Eenennaam, H., Sun, C., Garg, A. D., Borst, J., & Xiao, Y. (2023). CD4+ helper T cells endow cDC1 with cancer-impeding functions in the human tumor micro-environment. *Nature Communications*, *14*(1). https://doi.org/10.1038/S41467-022-35615-5

Levenberg, K. (1944). A METHOD FOR THE SOLUTION OF CERTAIN NON – LINEAR PROBLEMS IN LEAST SQUARES. *Quarterly of Applied Mathematics*, *2*(2), 164–168. https://doi.org/10.1090/qam/10666

Lütkepohl, H. (2005). *New introduction to multiple time series analysis*. Springer Science & Business Media.

Lyashenko Mario; Dixit Purushottam D.; Lim Sang Kyun; Sorger Peter K.; Vitkup Dennis, E. N. (2020). Receptor-based mechanism of relative sensing and cell memory in mammalian signaling networks. *ELife*, *9*(NA), NA-NA. https://doi.org/10.7554/elife.50342

Malinverno, C., Corallino, S., Giavazzi, F., Bergert, M., Li, Q., Leoni, M., Disanza, A., Frittoli, E., Oldani, A., Martini, E., Lendenmann, T., Deflorian, G., Beznoussenko, G. V., Poulikakos, D., Ong, K. H., Uroz, M., Trepat, X., Parazzoli, D., Maiuri, P., … Scita, G. (2017). Endocytic reawakening of motility in jammed epithelia. *Nature Materials*, *16*(5), 587–596. https://doi.org/10.1038/nmat4848

Malmersjö Paola; Smedler Erik; Planert Henrike; Kanatani Shigeaki; Liste Isabel; Nanou Evanthia; Sunner Hampus; Abdelhady Shaimaa; Zhang Songbai; Andäng Michael; Manira Abdeljabbar El; Silberberg Gilad; Arenas Ernest; Uhlén Per, S. R. (2013). Neural progenitors organize in small-world networks to promote cell proliferation. *Proceedings of the National Academy of Sciences of the United States of America*, *110*(16), 201220132–201220179. https://doi.org/10.1073/pnas.1220179110

Marx, V. (2021). Method of the Year: spatially resolved transcriptomics. *Nature Methods*, *18*(1), 9–14. https://doi.org/10.1038/S41592-020-01033-Y

McKay, B. D., & Piperno, A. (2014). Practical graph isomorphism, II. *Journal of Symbolic Computation*, *60*, 94–112. https://doi.org/10.1016/J.JSC.2013.09.003

Milo, R., Itzkovitz, S., Kashtan, N., Levitt, R., Shen-Orr, S., Ayzenshtat, I., Sheffer, M., & Alon, U. (2004). Superfamilies of evolved and designed networks. *Science (New York, N.Y.)*, *303*(5663), 1538–1542. https://doi.org/10.1126/SCIENCE.1089167

Milo, R., Shen-Orr, S., Itzkovitz, S., Kashtan, N., Chklovskii, D., & Alon, U. (2002). Network motifs: simple building blocks of complex networks. *Science (New York, N.Y.)*, *298*(5594), 824–827. https://doi.org/10.1126/SCIENCE.298.5594.824

Muldoon Yishan; Bagheri Neda; Leonard Joshua N., J. J. ; C. (2020). Macrophages employ quorum licensing to regulate collective activation. *Nature Communications*, *11*(1), 878. https://doi.org/10.1038/s41467-020-14547-y

Nahum, A., Koren, Y., Ergaz, B., Natan, S., Miller, G., Tamir, Y., Goren, S., Kolel, A., Jagadeeshan, S., Elkabets, M., Lesman, A., & Zaritsky, A. (2023). Inference of long-range cell-cell force transmission from ECM remodeling fluctuations. *Communications Biology*, *6*(1), 811. https://doi.org/10.1038/s42003-023-05179-1

Ng Mary A.; Mehta Arnav; Siu Sharmayne; Irwin Blythe; Pease Shirley; Hirose Satoshi; Elowitz Michael B.; Rothenberg Ellen V.; Kueh Hao Yuan, K. K. N. ; Y. (2018). A stochastic epigenetic switch controls the dynamics of T-cell lineage commitment. *ELife*, *7*(NA), NA-NA. https://doi.org/10.7554/elife.37851

Nicholson Roberto, S. M. ; B. (1997). Gap junctions: Getting the message through. *Current Biology : CB*, *7*(6), 340–344. https://doi.org/10.1016/s0960-9822(06)00169-2

Nitsan Stavit; Lewis Yair E.; Cohen Shlomi; Tzlil Shelly, I. D. (2016). Mechanical communication in cardiac cell synchronized beating. *Nature Physics*, *12*(5), 472–477. https://doi.org/10.1038/nphys3619

Okamoto Eiji; Takagi Yoshimi; Akita Nobuyuki; Hayashi Tatsuya; Park Eun Jeong; Suzuki Koji; Shimaoka Motomu, T. K. (2017). Gap junction-mediated regulation of endothelial cellular stiffness. *Scientific Reports*, *7*(1), 6134. https://doi.org/10.1038/s41598-017-06463-x

Paszek Sheila; Ashall Louise; Sillitoe Kate; Harper Claire V.; Spiller David G.; Rand David A.; White Michael R. H., P. R. (2010). Population robustness arising from cellular heterogeneity. *Proceedings of the National Academy of Sciences of the United States of America*, *107*(25), 11644–11649. https://doi.org/10.1073/pnas.0913798107

Perkins Peter S., T. J. ; S. (2009). Strategies for cellular decision-making. *Molecular Systems Biology*, *5*(1), 326. https://doi.org/10.1038/msb.2009.83

Potter Tommy A.; Mugler Andrew; Sun Bo, G. B. (2016). Communication shapes sensory response in multicellular networks. *Proceedings of the National Academy of Sciences of the United States of America*, *113*(37), 10334–10339. https://doi.org/10.1073/pnas.1605559113

Raj Alexander, A. van O. (2008). Nature, Nurture, or Chance: Stochastic Gene Expression and Its Consequences. *Cell*, *135*(2), 216–226. https://doi.org/10.1016/j.cell.2008.09.050

Ray, J., Pinar, A., & Seshadhri, C. (2015). A stopping criterion for Markov chains when generating independent random graphs. *Journal of Complex Networks*, *3*(2), 204–220. https://doi.org/10.1093/comnet/cnu041

Risom, T., Glass, D. R., Averbukh, I., Liu, C. C., Baranski, A., Kagel, A., McCaffrey, E. F., Greenwald, N. F., Rivero-Gutiérrez, B., Strand, S. H., Varma, S., Kong, A., Keren, L., Srivastava, S., Zhu, C., Khair, Z., Veis, D. J., Deschryver, K., Vennam, S., … Angelo, M. (2022). Transition to invasive breast cancer is associated with progressive changes in the structure and composition of tumor stroma. *Cell*, *185*(2), 299-310.e18. https://doi.org/10.1016/J.CELL.2021.12.023

Rubanyi Paul M., G. M. ; V. (1988). Calcium and activation of the release of endothelium-derived relaxing factor. *Annals of the New York Academy of Sciences*, *522*(1), 226–233. https://doi.org/10.1111/j.1749-6632.1988.tb33360.x

Samorodnitsky, S., Campbell, K., Ribas, A., & Wu, M. C. (2024). A Spatial Omnibus Test (SPOT) for Spatial Proteomic Data. *Bioinformatics (Oxford, England)*, *40*(7). https://doi.org/10.1093/BIOINFORMATICS/BTAE425

Sarvaria, A., Madrigal, J. A., & Saudemont, A. (2017). B cell regulation in cancer and anti-tumor immunity. *Cellular & Molecular Immunology 2017 14:8*, *14*(8), 662–674. https://doi.org/10.1038/cmi.2017.35

Schäling, B. (2011). *The boost C++ libraries*. Boris Schäling.

Schwarz, G. (1978). Estimating the Dimension of a Model. *The Annals of Statistics*, *6*(2), 461–464. https://doi.org/10.1214/aos/1176344136

Scott, D. W. (2015). *Multivariate density estimation: theory, practice, and visualization*. John Wiley & Sons.

Seal, S., Neelon, B., Angel, P. M., O'Quinn, E. C., Hill, E., Vu, T., Ghosh, D., Mehta, A. S., Wallace, K., & Alekseyenko, A. V. (2024). SpaceANOVA: Spatial Co-occurrence Analysis of Cell Types in Multiplex Imaging Data Using Point Process and Functional ANOVA. *Journal of Proteome Research*, *23*(4), 1131–1143. https://doi.org/10.1021/ACS.JPROTEOME.3C00462

Seth Adam B.; Barnett Lionel, A. K. ; B. (2015). Granger Causality Analysis in Neuroscience and Neuroimaging. *The Journal of Neuroscience : The Official Journal of the Society for Neuroscience*, *35*(8), 3293–3297. https://doi.org/10.1523/jneurosci.4399-14.2015

Shannon Aaron; Edrington Westin; Zhao Yunhua; Jayasinghe Aroshan; Page-McCaw Andrea; Hutson M. Shane, E. K. ; S. (2017). Multiple Mechanisms Drive Calcium Signal Dynamics around Laser-Induced Epithelial Wounds. *Biophysical Journal*, *113*(7), 1623–1635. https://doi.org/10.1016/j.bpj.2017.07.022

Shen, P., & Fillatreau, S. (2015). Antibody-independent functions of B cells: a focus on cytokines. *Nature Reviews. Immunology*, *15*(7), 441–451. https://doi.org/10.1038/NRI3857

Smoly, I. Y., Lerman, E., Ziv-Ukelson, M., & Yeger-Lotem, E. (2017). MotifNet: a web-server for network motif analysis. *Bioinformatics (Oxford, England)*, *33*(12), 1907–1909. https://doi.org/10.1093/BIOINFORMATICS/BTX056

Spéder Andrea H., P. B. (2014). Gap Junction Proteins in the Blood-Brain Barrier Control Nutrient-Dependent Reactivation of Drosophila Neural Stem Cells. *Developmental Cell*, *30*(3), 309–321. https://doi.org/10.1016/j.devcel.2014.05.021

Spinosa Brock; Mejia Daniela Lewin; Buschhaus Johanna M.; Linderman Jennifer J.; Luker Gary D.; Luker Kathryn E., P. C. ; H. (2019). Short-term cellular memory tunes the signaling responses of the chemokine receptor CXCR4. *Science Signaling*, *12*(589), NA-NA. https://doi.org/10.1126/scisignal.aaw4204

Sun Guillaume; Stone Howard A., B. D. (2013). Network Characteristics of Collective Chemosensing. *Physical Review Letters*, *110*(15), 158103-NA. https://doi.org/10.1103/physrevlett.110.158103

Sun Josephine; Normand Valery; Rogers Matthew B.; Stone Howard A., B. L. (2012). Spatial-temporal dynamics of collective chemosensing. *Proceedings of the National Academy of Sciences of the United States of America*, *109*(20), 7753–7758. https://doi.org/10.1073/pnas.1121338109

Swain Michael B.; Siggia Eric D., P. S. ; E. (2002). Intrinsic and extrinsic contributions to stochasticity in gene expression. *Proceedings of the National Academy of Sciences of the United States of America*, *99*(20), 12795–12800. https://doi.org/10.1073/pnas.162041399

Tamir, Y., Bussi, Y., Owczarek, C., Luque, L., Torrisi, G., Rose, L. A., Kliper-Gross, O., Sander, C., Schumacher, L., Parsons, M., Keren, L., & Zaritsky, A. (2024). Data-modeling the interplay between single cell shape, single cell protein expression, and tissue state. *BioRxiv*, 2024.05.29.595857. https://doi.org/10.1101/2024.05.29.595857

Tay Jacob J.; Lee Timothy K.; Lipniacki Tomasz; Quake Stephen R.; Covert Markus W., S. H. (2010). Single-cell NF-κB dynamics reveal digital activation and analogue information processing. *Nature*, *466*(7303), 267–271. https://doi.org/10.1038/nature09145

Tenggara, J. B., Rachman, A., Prihartono, J., Rachmadi, L., Panigoro, S. S., Heriyanto, D. S., Sutandyo, N., Nasution, I. R., Rahadiati, F. B., Steven, R., Betsy, R., Juanputra, S., & Sudoyo, A. W. (2024). The relationship between high ratios of CD4/FOXP3 and CD8/CD163 and the improved survivability of metastatic triple-negative breast cancer patients: a multicenter cohort study. *BMC Research Notes*, *17*(1). https://doi.org/10.1186/S13104-024-06704-Z

Vaseršteĭn, L. N. (1969). ON THE STABILIZATION OF THE GENERAL LINEAR GROUP OVER A RING. *Mathematics of the USSR-Sbornik*, *8*(3), 383. https://doi.org/10.1070/SM1969V008N03ABEH001279

Wernicke, S., & Rasche, F. (2006). FANMOD: a tool for fast network motif detection. *Bioinformatics (Oxford, England)*, *22*(9), 1152–1153. https://doi.org/10.1093/BIOINFORMATICS/BTL038

Wolinsky, H. (1980). A proposal linking clearance of circulating lipoproteins to tissue metabolic activity as a basis for understanding atherogenesis. *Circulation Research*, *47*(3), 301–311. https://doi.org/10.1161/01.res.47.3.301

Wooldridge, J. (2016). Introductory Econometrics: A Modern Approach (Nelson Education, Toronto). *INTERNETES FORRÁSOK*.

Wu, Z., Trevino, A. E., Wu, E., Swanson, K., Kim, H. J., D'Angio, H. B., Preska, R., Charville, G. W., Dalerba, P. D., Egloff, A. M., Uppaluri, R., Duvvuri, U., Mayer, A. T., & Zou, J. (2022). Graph deep learning for the characterization of tumour microenvironments from spatial protein profiles in tissue specimens. *Nature Biomedical Engineering*, *6*(12), 1435–1448. https://doi.org/10.1038/S41551-022-00951-W

Wu, Z., & Zou, J. (2022). Learning spatial cellular motifs predictive of the responses of patients to cancer treatments. In *NATURE BIOMEDICAL ENGINEERING* (Vol. 6, Issue 12, pp. 1328–1329). NATURE PORTFOLIO HEIDELBERGER PLATZ 3, BERLIN, 14197, GERMANY.

Yamamoto Kishio; Nakamura Makiko; Kobatake Eiry; Sokabe Masahiro; Ando Joji, K. F. (2011). Visualization of flow-induced ATP release and triggering of Ca2+ waves at caveolae in vascular endothelial cells. *Journal of Cell Science*, *124*(20), 3477–3483. https://doi.org/10.1242/jcs.087221

Yang Mark W.; Basta Lena P.; Anseth Kristi S., C. T. (2014). Mechanical memory and dosing influence stem cell fate. *Nature Materials*, *13*(6), 645–652. https://doi.org/10.1038/nmat3889

Yin Ke-Ping; Zhang Jing; Kumar Ashok; Yu Fushin X, J. X. (2007). Wound-induced ATP release and EGF receptor activation in epithelial cells. *Journal of Cell Science*, *120*(5), 815–825. https://doi.org/10.1242/jcs.03389

Young Rae Lynn M.; Parghi Sean S; Walker Megan; Kidd Jeffrey M.; Trask Barbara J., J. M. ; E. (2008). Extensive Copy-Number Variation of the Human Olfactory Receptor Gene Family. *American Journal of Human Genetics*, *83*(2), 228–242. https://doi.org/10.1016/j.ajhg.2008.07.005

Zinner Ilya; Liberali Prisca, M. L. (2020). Design principles of tissue organisation: How single cells coordinate across scales. *Current Opinion in Cell Biology*, *67*(NA), 37–45. https://doi.org/10.1016/j.ceb.2020.07.004

תקציר

התארגנות עצמית היא תהליך שבו תאים בודדים מסדרים את עצמם במבנה וסדר ברמה גבוהה יותר. עבודת הגמר הזאת מגשרת בין קני מידה מרחביים בדינמיקות אותות רב-תאיים והתארגנות רב-תאית. הפרק הראשון חוקר את הסנכרון של יוני סידן בשכבות חד-שכבתיות של תאי אנדותל בתגובה לגירויים מכניים. השתמשנו בתורת האינפורמציה כדי לכמת את העברת המידע האסימטרית בין זוגות תאים והגדרנו מדדים כמותיים כיצד תאים בודדים מקבלים או מעבירים מידע ברשת רב-תאית. חשפנו כי הסנכרון הקולקטיבי התהווה באמצעות התפשטות הדרגתית של מידע, המונעת על ידי תכונות תקשורת הטרוגניות בין התאים. הפרק השני מציג את שיטת הזיהוי תלוי-הקשר של מוטיבים מרחביים (CISM) , שיטה לזיהוי אינטראקציות תאיות מודולריות בקנה מידה מרחבי עדין של מספר תאים. יישום של שיטת CISM על נתוני פרוטאומיקה של תא בודד במרחב במלנומה ובסרטן שד שלילי לשלושת הסמנים (TNBC), היא חזתה מצבי מחלה בצורה אפקטיבית וחשפה הרכבי תאים וארגון תאי מרחבי שמאפיינים מצבי מחלה שונים. מחקרים אלה חושפים את הרכיבים המודולריים ואת הדינמיקות המתפתחות שמובילים להתנהגות תאית קולקטיבית לצורך הבנה של התארגנות עצמית רב-תאית וקישור בין רכיבים מודולריים למצב מחלה**.**

גישור קני מידה מרחבי-זמניים בהעברת מידע והתארגנות במערכת רב-תאית

מחקר לשם מילוי חלקי של הדרישות לקבלת תואר ״דוקטור לפילוסופיה״

מאת

עמוס זמיר

הוגש לסינאט אוניברסיטת בן גוריון בנגב

אישור המנחה ______ ______________

אישור דיקן בית הספר ללימודי מחקר מתקדמים ע״ש קרייטמן ________________________

כ׳ תשרי תשפ״ד

22st Oct, 2024

באר שבע

גישור קני מידה מרחבי-זמניים בהעברת מידע והתארגנות במערכת רב-תאית

מחקר לשם מילוי חלקי של הדרישות לקבלת תואר ״דוקטור לפילוסופיה״

מאת

עמוס זמיר

הוגש לסינאט אוניברסיטת בן גוריון בנגב

כ׳ תשרי תשפ״ד **22st Oct, 2024**

באר שבע